On the study of atomic and molecular processes affecting Astrophysical Plasma using high-resolution optical and UV spectroscopy

by

Ahmad Nemer

A dissertation submitted to the Graduate Faculty of
Auburn University
in partial fulfillment of the
requirements for the Degree of
Doctor of Philosophy

Auburn, Alabama
August 3, 2019

Keywords: Recombination, evidence, dissociation

Approved by

Stuart Loch, Chair, Associate Professor of Physics
Allen Landers, Professor of Physics
Mike Fogle, Associate Professor of Physics
Mitch Pindzola, Professor of Physics
Laurent Guillaume, Associate Professor of Physics
Evangelos Miliordos, Assistant Professor of Chemistry

Abstract

Rydberg Enhanced Recombination (RER), a recombination process related to dielectronic recombination in which electrons are captured into energy states below the ionization threshold, has been theoretically predicted to occur in low temperature plasmas. First evidence of RER is shown to occur in astrophysical environments, using high resolution optical spectra of planetary nebulae and a UV spectrum of symbiotic stars. RER can significantly impact diagnosed ionic and elemental abundances of important astrophysical species, with implications for cosmological models. The project underlines the importance of including this process in models of photoionized plasmas.

Acknowledgments

This work was funded by a NASA grant to Auburn University (). We thank Dr. Francis Robicheaux for his original work on this subject. We also thank Dr. Daniel Savin and Dr. Randall Smith for the very useful feedback they gave on this work. The work of students Pierce Jackson, Sammy Rizzutto, and Matt Gill are also gratefully acknowledged.

Table of Contents

List of Figures

List of Tables

Chapter 1

Introduction

Recently a new atomic process was proposed [2] that can potentially explain the low temperatures of the purported H-poor component of gas in Planetary Nebulae (PNe) and may have broader ranging implications for the ionization structure and power loss mechanisms of photoionized plasmas. In this Rydberg Enhanced Recombination (RER) process, energy states just below the ionization threshold can contribute to recombination, thus enhancing the total recombination rate at low temperatures particularly those found in photoionized plasmas. We extend the analysis of Robicheaux et al. [2] To show that emission lines from doubly-excited below-threshold states can affect plasma conditions via charge balance, thus affecting synthetic spectral models used to simulate emission spectra and determine abundances. Thus, the primary aim of this dissertation is to search for spectroscopic evidence of this new mechanism and to determine its significance for plasma conditions. Searching for evidence of this mechanism in atomic physics experiments, or regular laboratory plasmas, is very challenging, with no direct observations of the mechanism previously found.

The physical conditions of low temperature planetary nebulae make them ideal astrophysical laboratories in which to investigate whether the RER mechanism is real and significant. Because the dominant ionization mechanism is photoionization, moderately charged states of elements can exist at electron temperatures much lower than one would expect in a collisionally ionized plasma. RER increases dramatically at low electron temperatures, particularly below 10,000K. In this project, we first identify elements and charge states that could be affected by RER, then we look for spectroscopic evidence of it in PNe. We chose to search very deep, high-resolution spectra of PNe and Symbiotic stars. Specifically, we find C II

emission lines that arise from doubly-excited states lying just below the ionization threshold that are mainly populated by RER. While many additional states in other ionic species are likely to be populated by RER (e.g., we predicted RER populated lines for OII, OIII, CII, CIII), most of the other states emit at ultraviolet wavelengths. We find a trace of the C III line in the UV spectrum of Symbiotic star systems.

In the remainder of this chapter we describe the astrophysical plasma environments that will be studied (section 1.1), give some background theory on modelling ions and spectra (section 1.2), describe some useful plasma diagnostics (section 1.3), and then describe the computational methods used in this work (section 1.4). Chapter 2 will describe the theory of the new atomic process and how to calculate the new rates. Chapter 3 will describe the search for evidence and the first observational evidence found in PNe and Symbiotic binaries. Chapter 4 will go in depth about the implications of including RER in current plasma models. Chapter 5 will describe in detail specific simulations using the Cloudy radiative transfer code [3], Chapter 6 will focus on the work done to obtain data from the Hubble Space Telescope (HST). Chapter 7 will discuss conclusions and future work.

1.1 Plasma environments

Low temperature photoionized astrophysical plasmas are some of the most prominent objects in our universe, and they exist in various shapes and forms depending on the circumstances responsible for their formation. These gases can be ionized directly from a source of radiation, such as low-mass dying stars in the case of PNe, a hot compact object in symbiotic binaries, or super-massive black holes like the ones surrounding Active Galactic Nuclei (AGN). Other types of photoionized gases could form due to propagating radiation from young, massive stars as can be found in H II regions, which in turn disperses into what is called the Intergalactic and the Interstellar Media (IGM and ISM). PNe and HII regions

mark the endpoints (beginning and end) of stellar evolution, and one can determine their elemental abundances through precise spectroscopic studies.The investigation of these nebulae will serve to unfold many mysteries in the related fields of stellar evolution, nucleosynthesis, galactic composition and kinematics, and cosmology [4]. The research of these nebulae has suffered from a 75-year-old [5] predicament dealing with elemental abundance determination and temperature diagnostics.

1.1.1 Planetary Nebuale

PNe are produced by intermediate mass stars Fig. 1.1, those in the 0.8 M$\odot$ to 8 M$\odot$ range (M$\odot$ = mass of the sun), while they transit from the red giant stage to the white dwarf stage; those are stars that are not massive enough to undergo and core-collapse supernova, but are heavy enough to fuse helium and pass the red giant phase [6]. They are probes of stellar evolution, populations, gas dynamics, dust and molecules. They are also extragalactic probes of metallicity and dynamics in spiral and elliptical galaxies and in the intracluster medium [4]. Spectra of PNe are characteristic and easy to identify: they have strong emission (as opposed to absorption) spectra due to the photoionized gas. These systems are suspected to evolve in binary configuration (which means it includes two central stars orbiting each other) which is reflected in their chemical history. They can survive in the intracluster medium, and are rare probes of this interesting environment. Extragalactic PNe have been studied to disclose a characteristic luminosity function whose high-luminosity cutoff appears invariant (or almost invariant) across PNe populations, providing a good standard candle. [7]

The study of these nebulae show that intermediate mass stars are responsible for most of the nitrogen, about half the carbon, and a non negligible fraction of oxygen and helium present in the universe [6]. These stars also produce an important fraction of the slow neutron process elements, like rubidium, strontium, zirconium, cesium, barium, lanthanum, and praseodymium. Big-Bang nucleosynthesis [8] created all the hydrogen and deuterium, most

of the helium and a fraction of the lithium. Massive stars, those with more than 8 $M_{\odot}$, produce most of the remaining elements including the fast neutron process elements as well as a fraction of the helium, carbon, nitrogen, and oxygen abundances [9].

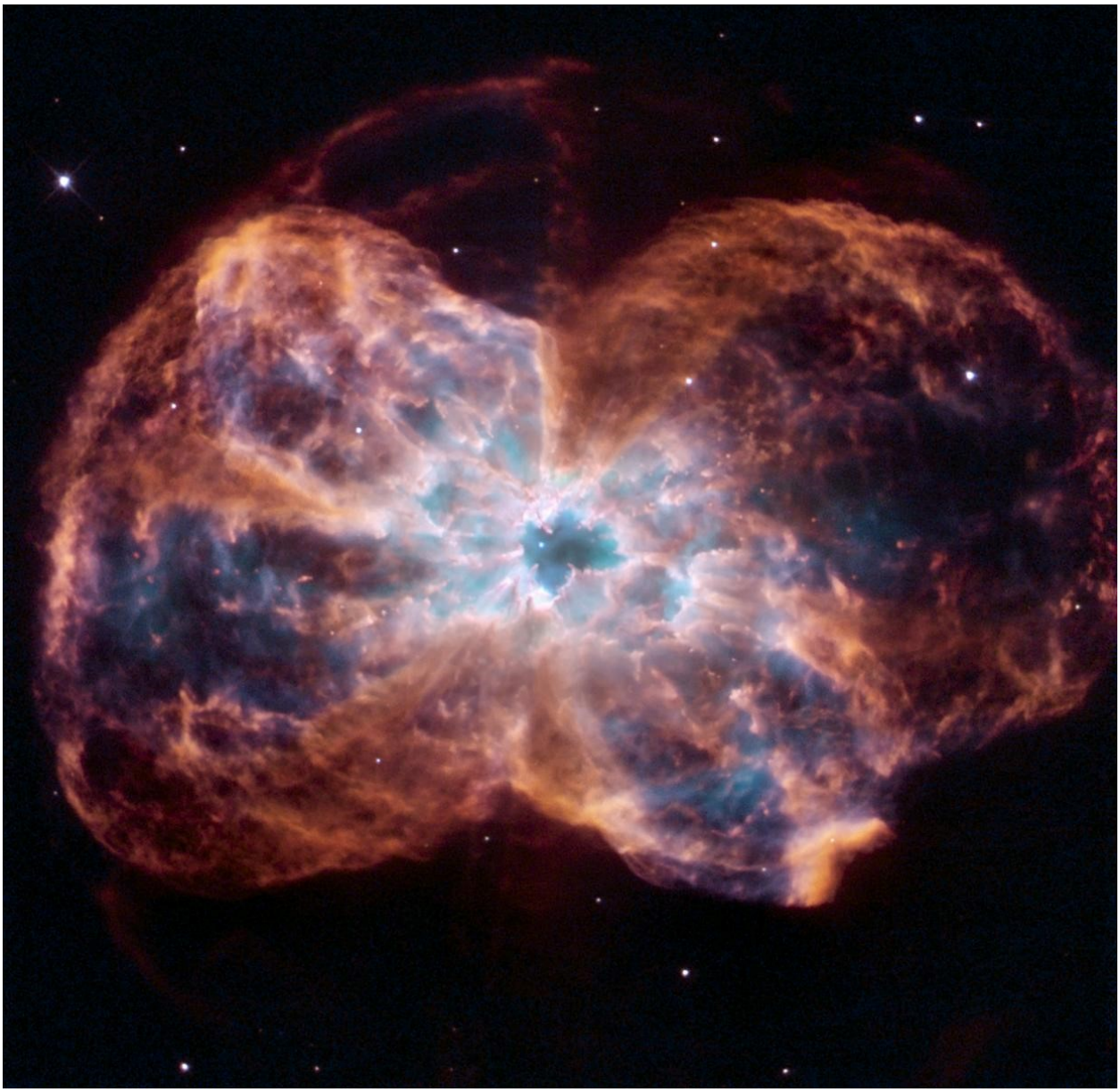

Figure 1.1: Image of the planetary nebula NGC 2440 from the WFC2 camera on the Hubble Space Telescope (courtesy STScI)

1.1.2 Symbiotic stars

Symbiotic stars are interacting binaries in which an evolved red giant accretes material into a hot and compact companion, usually a white dwarf (Fig. 1.2). It is typical for such a system to occupy a large spatial region because the presence of an evolved red giant (big) star is a requirement for Symbiotic systems. Symbiotic stars are thus interacting binaries with the longest orbital periods and the largest component separations. Mass accretion into the companion star play an important role in driving the basic symbiotic characteristics, and involves energetic phenomena relevant to many other astrophysical objects, including evolved single and binary stars or active regions in galaxies and quasars[10]. Symbiotic binaries are also among the most variable stars: their observed spectra experience changes due to the binary motion, but both components also show intrinsic variability with different timescales ranging from minutes (flickering and quasi-periodic oscillations of the hot component) to months and years (pulsations of the cool component), and even decades (nova-like eruptions of the hot component or solar-type cycles of the cool giant). Thus, these stars are a very attractive laboratory for studying various aspects of stellar evolution in binary systems [11]

Symbiotic stars are categorized in terms of stellar (S) and dusty (D) types based on their appearance at IR wavelengths [12]. The S-types have typical orbital periods of a few years and the cooler while the D-types have longer orbital periods. The hot components are dominantly white dwarfs in both the S and D type systems. However, a few exceptions have the hot component as an accretion disk around a main sequence star (Kenyon and Garcia 1986). In some cases the white dwarf is replaced by a neutron star. Such a binary is embedded is a circumstellar nebula formed by the material lost from both components [13].

Figure 1.2: An illustration of a Symbiotic binary with a white dwarf accreting material from a red giant

1.2 Plasma modelling

1.2.1 Atomic processes

A review is presented here of the main atomic processes relevant for the work.

Radiative transitions

The process of spontaneous emission would be

$$X^{+z}(i) \longrightarrow X^{+z}(j) + h\tilde{\nu} \tag{1.1}$$

where i is the initial level of the bound electron and j is the final level of the electron.

The **rate** of spontaneous emission is given by the Einetein A-coefficient. For electric dipole radiation this is given by:

$$A_{i\to j} = \frac{w_{ij}^3}{3\pi c^3 \hbar \varepsilon_o} | < \psi_j | D | \psi_i > |^2. \tag{1.2}$$

The photon that is given off has an angular frequency of ω_{ij}. The stimulated emission coefficient can be related to the photoabsorption and simulated emission via the detailed balance relationships. This produces the following expressions for the stimulated emission

$$B_{i\to j} = \frac{c^3}{8\pi h \nu^3} A_{i\to j} \tag{1.3}$$

and the photoabsorption coefficient is given by

$$B_{i\to j} = \frac{w_j}{w_i} B_{j\to i} \tag{1.4}$$

where w_i and w_j are statistical weights. In a plasma environments, electrons make transitions between bound states within an ion via radiative or collisional processes. They

also make transitions between charge states via ionization or recombination processes. Approximate A-values can be obtained using a classical expression, modified by a bound-bound Gaunt factor $\left(g_{ij}^I\right)$. ν_i effective quantum number = n - γ_i, where γ_i is the quantum defect representing the deviation from hydrogenic principle quantum number. If ν_i and ν_j are effective principle quantum numbers

$$A_{i\to j} = \underbrace{\frac{16\alpha^4 c}{3\sqrt{3}\pi a_o}}_{1.57456e10s^{-1}} \left(\frac{1}{w_i}\right) z_1^4 \left(\frac{1}{\nu_i^3 \nu_j^3}\right) \left(\frac{1}{|\frac{1}{\nu_i^2} - \frac{1}{\nu_j^2}|}\right) g_{ij}^I. \tag{1.5}$$

g_{ij}^I is usually close to one. Of course, electrons can also transition from bound to free states. Consider first **Photoionization**

$$X^{+Z}(i) + h\tilde{\nu} \longrightarrow X^{+z+1}(k) + e \tag{1.6}$$

The number of photoionizations/cm^3/s is

$$N_i a(\tilde{\nu}) \frac{c}{h\tilde{\nu}} u(\tilde{\nu}) d\tilde{\nu} \tag{1.7}$$

where $a(\tilde{\nu})$ is the photoionization cross section and $u(\tilde{\nu})$ is the radiation field density. The inverse process is **radiative recombination** with an associated capture cross section $Q_c(\tilde{\nu})$

$$X^{+z+1} + e \longrightarrow X^{+z}(i) + h\tilde{\nu} \tag{1.8}$$

There is also **stimulated recombination** with an induced radiation parameter $\sigma(\tilde{\nu})$.

$$X^{+z+1} + e + h\tilde{\nu} \longrightarrow X^{+z}(i) + h\tilde{\nu} + h\tilde{\nu} \tag{1.9}$$

Detailed balance relates these cross sections

$$\sigma(\tilde{\nu}) = \frac{c^3}{8\pi h\tilde{\nu}^3} Q_c(\tilde{\nu}) \tag{1.10}$$

$$Q_c(\tilde{\nu}) = \left(\frac{h\tilde{\nu}}{m_e v c}\right)^2 \frac{w_i}{w_+} a(\tilde{\nu}) \tag{1.11}$$

The expression for $Q_c(\tilde{\nu})$ is called the **Milne Relation**. In a real plasma it is the rates of the processes that are most important, rather that the cross sections. To describe this, we need to know the energy distribution of the free electrons.

It is common in many plasma environments for the free electrons to have a thermal distribution, described by a Maxwellian velocity distribution. Note that continuum states are considered to be the system of the ion plus the free electron.

$$f(v, T_e) = 4\pi \left(\frac{m}{2\pi k T_e}\right)^{3/2} e^{\frac{-\frac{1}{2}mv^2}{kT_e}} v^2 \tag{1.12}$$

In this case, the radiative recombination **rate coefficient** is given by

$$\alpha_i(T_e) = \sqrt{\frac{2}{\pi}} \frac{1}{c^2} \left(m_e k T_e\right)^{-\frac{3}{2}} \frac{w_i}{w_+} e^{\frac{I_i}{kT_e}} \int_{I_i}^{\infty} a\left(\tilde{\nu}\right) \left(h\tilde{\nu}\right)^2 e^{\frac{-h\tilde{\nu}}{kT_e}} d\left(h\tilde{\nu}\right) \tag{1.13}$$

At lower temperatures, $\alpha_i(T_e)$ falls off as $\frac{1}{T_e^{\frac{1}{2}}}$. At higher temperatures, $\alpha_i(T_e)$ falls off as $\frac{1}{T_e^{\frac{3}{2}}}$. Due to this rapid decrease with temperature, radiative recombination is not usually important in collisionally ionized plasmas, but maybe important in low temperature photoionized plamas.

Dielectronic recombination

This process was thought to be unimportant, but in the 1960s it was found to be the dominant recombination mechanism for many plasmas and was essential in describing the spectral emission from the solar corona [14]. This is a two-step process:

i. **Resonance Capture**:

$$A^{+Z+1}(i) + e \longleftrightarrow A^{+Z}(j, nl)$$

The free electron 'collides' with the bound electron. The bound electron gains some energy and the free electron loses energy and is captured into nl. **This happens at a precise energy for each nl.** The reverse process is called Auger breakup and is very fast.

ii. **Radiative Stabilization**:

$$\begin{aligned} A^{+Z}(j, nl) &\longrightarrow A^{+Z}(i, nl) + h\tilde{\nu}(TypeI) \\ &\longrightarrow A^{+Z}(j, n'l') + h\tilde{\nu}(TypeII) \end{aligned}$$

The recombination process is only complete if the ion ends up in a bound state. The type I radiative transition produces a photon called a 'satellite line.' This photon is very slightly shifted from the emission of

$$A^{+Z+1}(j) \longrightarrow A^{+Z+1}(i) + h\tilde{\nu}$$

Note that there is more than one possible core-excitation. For example, for a Be-like system them $1s^2 2s^2$ initial state could be excited to 2s2p (^1P) nl (called Δn=0 transitions). It could also excite out of the valence n-shell (e.g. to 2s3lnl for Δn=1 transitions).

The dielectronic recombination cross section is measured as a function of incident **electron energy**. Note that in typical experiments that measure DR it is a beam of electrons that is recombining with the ions, and the beam has a very narrow energy distribution. Thus, the experiment is able to resolve the resonances. Note that the resonance positions are approximately given by

$$E^{res}(n) \approx E_s - \underbrace{\frac{RZ_1^2}{n^2}}_{Hydrogenic} \tag{1.14}$$

Where E_s is the energy of the ionization threshold, R is the Rydnerg constant, and Z_1 is the effective charge seen by the Rydberg electron. The total dielectronic recombination Maxwellian rate coefficient is given by

$$\alpha^{DR}(T_e) = 2\frac{v_a}{\sqrt{\pi}}\sqrt{\frac{I_H}{kT_e}}\int_0^\infty \frac{\epsilon}{kT_e} \overbrace{\sigma^{DR}(\epsilon)}^{DR\ cross\ section} e^{\frac{-\epsilon}{kT_e}} d\left(\frac{\epsilon}{kT_e}\right) \tag{1.15}$$

v_a is $2.188 \times 10^8 cm/s$, σ^{DR} is dielectronic recombination cross section [cm^2], and ϵ is the electron density [eV]. $\sigma^{DR}(\epsilon)$ represents the DR cross section summed over all the resonances (doubly excited states), and if it was replaced by an individual resonance's cross section, then the above expression would be the dielectronic capture rate coefficient to that state.

Note that although the selection rules for radiation do not hold for dielectronic capture, they still give a reasonable indication of which core excitation will have the largest rate coefficient (i.e. $\Delta n = 0$, dipole allowed excitations). The strength of the resonances are given by $\frac{A_i^a A_i^r}{A^a + A^r}$. A_i^a is the dielectronic capture into i and A_i^r is the radiative stabilization of i.

Electron impact ionization

This process is

$$A^{+Z}(i) + e(\epsilon_i) \longleftrightarrow A^{+Z+1}(j) + e + e$$

The inverse process is the three-body recombination. The process is described by an ionization cross section that is zero below the ionization potential for the ion. There are two main processes that can lead to an ionization

i. **Direct Ionization**

$$\begin{aligned} Xe^{43+}(1s^2 2s^2 2p^6 3s) + e &\longrightarrow Xe^{42+}(1s^2 2s^2 2p^6) + e + e \\ &\longrightarrow Xe^{42+}(1s^2 2s^2 2p^5 3s) + e + e \end{aligned}$$

ii. **Excitation-Autoionization**

$$Xe^{43+}(1s^2 2s^2 2p^6 3s) + e \longrightarrow Xe^{43+}\underbrace{(1s^2 2s^2 2p^5 3snl)}_{Auger} + e \tag{1.16}$$

which can then undergo Auger decay to the next ion stage via

$$Xe^{43+}(1s^2 2s^2 2p^5 3snl) \longrightarrow Xe^{43+}(1s^2 2s^2 2p^6) + e$$

In this case, a core-excitation results in an autoionizing configuration that can Auger. For low charge states, these Auger rates are very large. However, for more highly charged ions, the radiative rates of the autoionizing configuration can compete with the Auger rates,

reducing the excitation-autoionization cross section. This is shown in the next set of figures.

If one compares the ionization and total ($DR + RR$) recombination rate coefficient for a typical ion, it is clear that ionization rates become bigger than recombination rates at temperatures significantly below the ionization potential for that ion for collisionally ionized plasmas. For photoionized plasmas, the dominant processes are the ones that prevail at low temperatures. In this case DR+RR are balanced by photoinization which will allow for higher charge states to exist at low temperatures

Electron impact excitation

In most plasmas, the excited state populations depend strongly on the electron impact excitation rate coefficients.

$$X^{+Z}(i) + e(\epsilon_i) \longrightarrow X^{+Z}(j) + e(\epsilon_j)$$

Energy is conserved, thus $\Delta E_{ij} = \epsilon_i - \epsilon_j$. The excitation cross section $\sigma_{i\rightarrow j}(\epsilon_i)$ (in cm^2) describes the process.

We define a dimensionless threshold-scaled energy, $X = \frac{\epsilon_i}{\delta E_{ij}}$ for $X \in [1, \infty]$ and a dimensionless quantity called the **collision strength** that is related to the cross section.

$$\begin{aligned} \Omega_{ij} &= w_i \left(\frac{\epsilon_i}{I_H}\right) \frac{\sigma_{i\rightarrow j}\left(\epsilon_i\right)}{\pi a_o^2} \\ &= w_j \left(\frac{\epsilon_j}{I_H}\right) \frac{\sigma_{j\rightarrow i}\left(\epsilon_j\right)}{\pi a_o^2} \end{aligned} \tag{1.17}$$

Ω_{ij} is symmetric between initial and final states. $\pi a_o^2 = 8.7972 \times 10^{-17}\ cm^2$

The Maxwellian excitation rate coefficient is:

$$\begin{aligned} q_{i\to j} &= 4\pi\left(\frac{m_e}{2\pi kT_e}\right)^{3/2}\int_0^\infty v_i e^{-\frac{\epsilon_i}{kT_e}}\sigma_{i\to j}\left(\epsilon_i\right)v_i^2 dv_i \\ &= 2\sqrt{\pi}\alpha c a_o^2\left(\frac{I_H}{kT_e}\right)^{1/2}\frac{1}{w_i}e^{-\frac{\Delta E_{ij}}{kT_e}}\int_0^\infty \Omega_{ij}(\epsilon_j)e^{-\frac{\epsilon_j}{kT_e}}d\left(\frac{\epsilon_j}{kT_e}\right) \end{aligned} \tag{1.18}$$

$2\sqrt{\pi}\alpha c a_o^2 = 2.1716\times 10^{-8}\ cm^2\ s^{-1}$

We also define an **effective collision strength**, Υ_{ij} (Upsilon)

$$\Upsilon_{ij}(T_e) = \int_0^\infty \Omega_{ij}(\epsilon_i)e^{-\frac{\epsilon_j}{kT_e}}d\left(\frac{\epsilon_j}{kT_e}\right) \tag{1.19}$$

$$\begin{aligned} q_{j\to i}(T_e) &= \frac{w_i}{w_j}e^{\frac{\Delta E_{ij}}{kT_e}}q_{i\to j}(T_e) \\ &= 2\sqrt{\pi}\alpha c a_o^2\frac{1}{w_j}\left(\frac{I_H}{kT_e}\right)^{1/2}\Upsilon_{ij} \end{aligned} \tag{1.20}$$

Let us consider the case of Li^+, and the means of exciting from the ground term to the 1s2p ^1P term. Note that one can have **direct excitation**,

$$Li^+(1s^2) + e \longrightarrow Li^+(1s2p\ ^1P) + e$$

and **resonant excitation**.

$$Li^+(1s^2) + e \longleftrightarrow Li\underbrace{(1s3p\ nl)}_{Auger}$$

which can then Auger decay into an excited term:

$$Li(1s3p\ nl) \longleftrightarrow Li^{+}(1s2p\ ^{1}P) + e$$

Note that because of the large number of possible nl states, there will be a whole series of resonance attached to each possible core excitation, we have just considered the 1s-3p core excitation here. This means that the excitation cross section has a smooth background that corresponds to the direct ionization process, on top of this is the indirect excitation (resonant excitation), which consists of a large number of usually very thin resonances. Resonance contributions have the largest effect on transitions with weak backgrounds, such as the non-dipole excitations. Also, not that while the dipole selection rules that we showed earlier are just for photon transitions, they also give a good indication of which electron-impact processes will be strong.

1.2.2 Equilibrium ionization balance and photoionized plasmas

Given ionization and recombination rate coefficients, one can determine the temperature at which each ion stage of an element will form. Most of the population in an ion stage is in the ground state. Thus, for the moment, we will only consider rates that connect ground states.

Consider an element with three ion stages, including the bare nucleus. Let α , β , γ be the ground states of the four ion stages. We will consider only connections between adjacent ion stages

$$\begin{aligned}
\frac{dN_\alpha}{dt} &= -S_{\alpha\to\beta}N_\alpha N_e + R_{\beta\to\alpha}N_\beta N_e + 0\ N_\gamma N_e \\
\frac{dN_\beta}{dt} &= S_{\alpha\to\beta}N_\alpha N_e - \left(R_{\beta\to\alpha} + S_{\beta\to\alpha}\right) N_\beta N_e + R_{\gamma\to\beta}N_\gamma N_e \\
\frac{dN_\gamma}{dt} &= 0\ N_\alpha N_e + S_{\beta\to\gamma}N_\beta N_e - R_{\gamma\to\beta}N_\gamma N_e
\end{aligned} \tag{1.21}$$

Where $S_{\alpha\to\beta}$ represent all ionization (collisional and photoionization), and $R_{\beta\to\alpha}$ represents all recombination processes which can be written as:

$$\begin{bmatrix} dN_\alpha/dt \\ dN_\beta/dt \\ dN_\gamma/dt \end{bmatrix} = \begin{bmatrix} C_{\alpha\alpha} & C_{\alpha\beta} & C_{\alpha\gamma} \\ C_{\beta\alpha} & C_{\beta\beta} & C_{\beta\gamma} \\ C_{\gamma\alpha} & C_{\gamma\beta} & C_{\gamma\gamma} \end{bmatrix} \begin{bmatrix} N_\alpha \\ N_\beta \\ N_\gamma \end{bmatrix} \tag{1.22}$$

Note that this is not really three equations with three unknowns. Due to the fact that each gain rate goes in elsewhere as a loss rate, this is really an underdetermined equation. Thus, we require one other equation to use in the solution. We use particle conservation

$$N^{TOT} = N_\alpha + N_\beta + N_\gamma \tag{1.23}$$

We can then solve for the equilibrium populations by setting dN/dt=0. We replace the first equation with the one for N^{TOT}.

$$\begin{bmatrix} N^{TOT} \\ 0 \\ 0 \end{bmatrix} = \begin{bmatrix} 1 & 1 & 1 \\ C_{\beta\alpha} & C_{\beta\beta} & C_{\beta\gamma} \\ C_{\gamma\alpha} & C_{\gamma\beta} & C_{\gamma\gamma} \end{bmatrix} \begin{bmatrix} N_\alpha \\ N_\beta \\ N_\gamma \end{bmatrix} \tag{1.24}$$

Which we can then solve for the fractional abundances.

$$\begin{bmatrix} N_\alpha/N^{TOT} \\ N_\beta/N^{TOT} \\ N_\gamma/N^{TOT} \end{bmatrix} = \begin{bmatrix} 1 & 1 & 1 \\ C_{\beta\alpha} & C_{\beta\beta} & C_{\beta\gamma} \\ C_{\gamma\alpha} & C_{\gamma\beta} & C_{\gamma\gamma} \end{bmatrix}^{-1} \begin{bmatrix} 1 \\ 0 \\ 0 \end{bmatrix} \tag{1.25}$$

This can, of course, be generalized for a system of N ion stages and solved numerically. Note that the matrix coefficients and, hence, the fractional abundances are only a function of electron temperature. If the excited states are included in the modeling, then the results become both temperature and density dependent. Thus, seeing emission from a given ion stage immediately gives us a range of temperatures that the plasma can have.

1.2.3 Population modeling and spectroscopy

In the following sections we will look at different approximations that are used to model the excited populations (and hence the spectra) of atoms. We will use the atomic data described earlier in this chapter in these models. In the first approximation we will evaluate the populations in Local Thermodynamic Equilibrium (LTE), valid for black body plasmas or plasmas at high densities. In the second approximation, valid at low densities, we use the Coronal approximation. In the last method, we use collisional-radiative theory, which is valid at all densities.

Local Thermodynamic Equilibrium

If a plasma is in thermodynamic equilibrium, then all of its physical characteristics are determined by the temperature. The radiation field is given by a Plank distribution

$$u(\nu) = \frac{8\pi h\nu^3}{c^3}\frac{1}{e^{h\nu}kT - 1} \tag{1.26}$$

The free electrons have a Maxwellian distribution

$$f(v) = 4\pi\left(\frac{m}{2\pi kT_e}\right)^{3/2} e^{-\frac{mv^2}{2kT_e}}v^2 \tag{1.27}$$

The bound states have a Boltmann distribution

$$\frac{N_i}{N_j} = \frac{\omega_i}{\omega_j}e^{-\frac{E_i - E_j}{kT_e}} \tag{1.28}$$

and alternatively they can be modelled with a Saha-Boltzmann distribution if one knows information about the ion, N_+.

$$N_i = N_e N_+ \left(\frac{h^2}{2\pi mkT_e}\right)^{3/2} \frac{\omega_i}{2\omega_+}e^{\frac{I_i}{kT_e}} \tag{1.29}$$

Where I_i is the ionization potential for level i. A plasma can be in **local** thermodynamic equilibrium (LTE) if collision timescales are sufficiently faster than radiative timescales, i.e. collisional-redistribution happens before radiative losses drive the system out of thermodynamic equilibrium. If a system is in LTE, the above equations hold.

To check if the collisional rates for a given excited state (N_i) will dominate over the radiative rates, one can evaluate the following ratio

$$\frac{\sum_{j<i} A_{i\to j}}{N_e \sum_{i\neq j} q_{i\to j}} \tag{1.30}$$

whenever this is less than one, the collisional rates will be greater than the radiative rates. The collisional-rates would have to dominate by a larger factor to drive the populations

to LTE. Note that one can either evaluate a critical N_e at which the populations are driven to LTE, or a critical n-shell at which they become LTE.

It is useful to consider typical timescales in a plasma, the following expressions give rough timescales for particles to reach equilibrium with other particles.

Electron-electron equipartition:

$$\tau_{ee} \sim 1.96 \times 10^7 \left(\frac{kT_e}{I_H}\right)^{3/2} \frac{1}{N_e \Lambda} \tag{1.31}$$

Electron-proton equipartition:

$$\tau_{ep} \sim 8.64 \times 10^6 \frac{m_p}{m_e} \left(\frac{kT_e}{I_H} + 5.4 \times 10^{-4} \frac{kT_p}{I_H}\right) \frac{1}{n_p ln\Lambda} \sim 1849 \tau_{ee} \tag{1.32}$$

The timescale for the excited states to reach equilibrium with the ground and metastable populations:

$$\tau_o \sim \frac{1}{N_e \sum q_{i \to j} + \sum A_{i \to j}} \sim 1 \times 10^{-8} s \tag{1.33}$$

The timescales for the ground and metastable states to reach equilibrium is much slower than the excited states, as they have no-where to radiate to.

$$\tau_g, \tau_m \sim \frac{(1 \times 10^8) z_1}{N_e} \tag{1.34}$$

and the timescale for the autoionizing levels to reach equilibrium is

$$\tau_a \sim \frac{1}{\sum A^r + \sum A^a} \sim 1 \times 10^{-14} s \tag{1.35}$$

The table 1.1 shows some typical equilibrium timescales for laboratory plasmas and the solar corona.

	N_e (cm^{-3})	T_e (K)	τ_{ee}(s)	τ_g (s)	τ_o (s)
PNe	$\sim 5 \times 10^4$	$\sim 1 \times 10^4$	~ 11.15	$\sim 4 \times 10^4$	$\sim 5 \times 10^{-4}$
Laboratory plasma	$\sim 1 \times 10^{13}$	$\sim 1 \times 10^7$	$\sim 3 \times 10^{-4}$	$\sim 1 \times 10^{-5}$	$\sim 1 \times 10^{-8}$

Table 1.1: A table showing typical timescales for the plasma environments studied in this work

The Coronal Approximation

Thus, in practice, the free electrons usually have a Maxwellian distribution. The ground and metastable states vary on a timescale similar to the plasma dynamics and must be modelled as part of the plasma evolution. The autoionizing and excited states very quickly come into equilibrium with the ground and metastable states. This is called the **quasi-static equilibrium** approximation. Before considering this we will consider the low density limit, the **Coronal Approximation**. This assumes that

- The only mechanism to populate the excited states is collisional excitation from the ground.
- The only depopulating mechanism for excited states is radiative decay.

Collisional-Radiative Theory

All excited populations should become Coronal at low electron densities and LTE at high electron densities. The regime in between these two limits is called the **Collisional-Radiative regime**. We consider the set of linear differential equations describing the rate of change of the populations of the ground and excited states. Note that here we are simply balancing the rates involving all of the atomic processes that we considered earlier in this chapter. While we could consider rate equations for all of the ion stages at one, in practice it is sufficient just to consider one ion stage and the ground of the next ion stage up. This is the same as saying that an excited state is overwhelmingly populated via excitation within the current ion stage, or recombination from the next ion stage. So we are omitting

ionization from the previous ion stage as an imporant mechanism (though it can be included in principle).

$$
\begin{aligned}
\frac{dN_1}{dt} &= -N_e(\sum_{j\neq 1} q^e_{1\to j} + S_1)N_1 + (A_{2\to 1} + N_e q_{2\to 1})N_2 + ...(A_{n\to 1} + N_e q_{n\to 1})N_n + \\
&\quad N_e R_{+\to 1} N_+ \\
\frac{dN_2}{dt} &= N_e q_{1\to 2} N_1 - (A_{2\to 1} + N_e(\sum_{j\neq 2} q^e_{2\to j} + S_2))N_2 + ...(A_{n\to 2} + N_e q_{n\to 2})N_n + \\
&\quad N_e R_{+\to 2} N_+ \\
\frac{dN_3}{dt} &= N_e q_{1\to 3} N_1 + N_e q_{2\to 3} N_2 - (\sum_{j<3} A_{3\to j} + N_e(\sum_{j\neq 3} q^e_{3\to j} + S_3))N_3 + ... \\
&\quad +(A_{n\to 3} + N_e q_{n\to 3})N_n + N_e R_{+\to 3} N_+ \\
.... &\quad ..... \\
.... &\quad ..... \\
\frac{dN_n}{dt} &= N_e q_{1\to n} N_1 + N_e q_{2\to n} N_2 + N_e q_{3\to n} N_3 + ... - (\sum_{j<n} A_{n\to j} + N_e(\sum_{j<n} q^e_{n\to j} + S_n))N_n \\
&\quad +N_e R_{+\to n} N_+ \\
\frac{dN_+}{dt} &= N_e S_1 N_1 + N_e S_2 N_2 + N_e S_3 N_3 ..... + N_e S_n N_n - NeN_+ \sum_j R_{+\to j}
\end{aligned}
\tag{1.36}
\tag{1.37}
$$

This can be written in matrix form, using C to represent the total atomic rates in each matrix element.

$$\begin{bmatrix} dN_1/dt \\ dN_2/dt \\ dN_3/dt \\ .... \\ .... \\ dN_n/dt \\ dN_+/dt \end{bmatrix} = \begin{bmatrix} C_{11} & C_{12} & C_{13} & .. & .. & C_{1n} & R_1 \\ C_{21} & C_{22} & C_{23} & .. & .. & C_{2n} & R_2 \\ C_{31} & C_{32} & C_{33} & .. & .. & C_{3n} & R_3 \\ ... & ... & ... & .. & .. & ... & .. \\ ... & ... & ... & .. & .. & ... & .. \\ C_{n1} & C_{n2} & C_{n3} & .. & .. & C_{nn} & R_n \\ N_eS_{1+} & N_eS_1 & N_eS_2 & .. & .. & N_eS_n & -\sum_n R_n \end{bmatrix} \begin{bmatrix} N_1 \\ N_2 \\ N_3 \\ .. \\ .. \\ N_n \\ N_+ \end{bmatrix} \tag{1.38}$$

The excited states are in equilibrium with the ground, so we can set the $dN/dt = 0$ for the excited states.

$$\begin{bmatrix} dN_1/dt \\ 0 \\ 0 \\ 0 \\ 0 \\ 0 \\ dN_+/dt \end{bmatrix} = \begin{bmatrix} C_{11} & C_{12} & C_{13} & .. & .. & C_{1n} & R_1 \\ C_{21} & C_{22} & C_{23} & .. & .. & C_{2n} & R_2 \\ C_{31} & C_{32} & C_{33} & .. & .. & C_{3n} & R_3 \\ ... & ... & ... & .. & .. & ... & .. \\ ... & ... & ... & .. & .. & ... & .. \\ C_{n1} & C_{n2} & C_{n3} & .. & .. & C_{nn} & R_n \\ N_eS_{1+} & N_eS_1 & N_eS_2 & .. & .. & N_eS_n & -\sum_n R_n \end{bmatrix} \begin{bmatrix} N_1 \\ N_2 \\ N_3 \\ .. \\ .. \\ N_n \\ N_+ \end{bmatrix} \tag{1.39}$$

Note that we cannot in general set the dN/dt for the ground (and metastable) states, because the plasma conditions can change on a timescale quicker than the equilibrium timescale for those levels. So normally we solve the time-dependence of the ground and metastable levels as part of a plasma code. However, it is still possible to isolate the atomic physics from the plasma physics and evaluate the excited populations as a function of the ground and metastable populations. These are sometimes called their 'driving populations'.

First, we eliminate the first and last rows. Consider the matrix on the right hand side, we can move the first and last contribution to the left hand side of the equation.

$$\begin{bmatrix} -C_{21}N_1 - R_2N_+ \\ -C_{31}N_1 - R_3N_+ \\ ... - ... \\ ... - ... \\ -C_{n1}N_1 - R_nN_+ \end{bmatrix} = \begin{bmatrix} C_{22} & C_{23} & .. & .. & C_{2n} & \\ C_{32} & C_{33} & .. & .. & C_{3n} & \\ ... & ... & .. & .. & ... & \\ & ... & ... & .. & .. & ... \\ C_{n2} & C_{n3} & .. & .. & C_{nn} & \end{bmatrix} \begin{bmatrix} N_2 \\ N_3 \\ .. \\ .. \\ N_n \end{bmatrix} \tag{1.40}$$

We can then solve for the excited populations with a matrix inversion

$$\begin{bmatrix} N_2 \\ N_3 \\ .. \\ .. \\ N_n \end{bmatrix} = \begin{bmatrix} C_{22} & C_{23} & .. & .. & C_{2n} \\ C_{32} & C_{33} & .. & .. & C_{3n} \\ ... & ... & .. & .. & ... \\ ... & ... & .. & .. & ... \\ C_{n2} & C_{n3} & .. & .. & C_{nn} \end{bmatrix}^{-1} \begin{bmatrix} -C_{21}N_1 - R_2N_+ \\ -C_{31}N_1 - R_3N_+ \\ ... - ... \\ ... - ... \\ -C_{n1}N_1 - R_nN_+ \end{bmatrix} = \tag{1.41}$$

If we call the matrix that we are to invert on the RHS, the *reduced collisional-radiative matrix C'*, then we have

$$\begin{bmatrix} N_2 \\ N_3 \\ .. \\ .. \\ N_n \end{bmatrix} = \left[C'\right]^{-1} \begin{bmatrix} -C_{21}N_1 - R_2N_+ \\ -C_{31}N_1 - R_3N_+ \\ ... - ... \\ ... - ... \\ -C_{n1}N_1 - R_nN_+ \end{bmatrix} \tag{1.42}$$

Or, written in terms of the individual matrix elements we have

$$N_2 = -\sum_j {C'_{2j}}^{-1} C_{j1}N_1 - N_e \sum_j {C'_{2j}}^{-1} R_jN_+ \tag{1.43}$$

with the general level being given by

$$N_i = -N_1(\underbrace{\sum_j {C'_{ij}}^{-1} C_{j1}}_{Excitation\ contribution}) - N_e N_+(\underbrace{\sum_j {C'_{ij}}^{-1} R_j N_+}_{Recombination\ contribution}) \tag{1.44}$$

This can be further generalized for σ metastable states in the ion and ρ metastables in the plus ion stage.

$$N_i = -\sum_\sigma N_\sigma \sum_j {C'_{ij}}^{-1} C_{j\sigma} - N_e \sum_\rho N_\rho^+ \sum_j {C'_{ij}}^{-1} R_{j\rho} \tag{1.45}$$

This system of equations is easily solved numerically on a computer. Note that one can archive the contributions from N_σ and N_ρ^+ on a T_e, N_e grid for later use once we know the fractional abundances of these ground and metastable states.

The ADAS code ADAS208 solves the above equations, and the ADAS code ADAS405 gives the equilibrium fractional abundances (N_σ and N_ρ). Note that in the coronal density regime, collisions between the excited states are negligible. At higher densities, populations and spectral line ratios will be density dependent as well as temperature dependent. At higher densities, the line ratio will be density dependent as well as temperature dependent. In this case, we would have to solve the collisional-radiative equations to determine the temperature.

Since collisional redistribution increases with density, solving the equilibrium population equations serves to calculate the excited level populations for higher density regime. But it can also be used to calculate the populations of high Rydberg states in the low density environments. I utilized ADAS 204 to calculate Rydberg states' populations as they are needed later on to calculate transition rates between these Rydberg states and resonant doubly excited states for the low density conditions we have in PNe and Symbiotic.

1.2.4 Radiative Transfer

Emission lines from the most abundant elements in the universe such as Carbon, Oxygen, and Nitrogen have been extensively used as diagnostic tools for plasma conditions. Carbon abundances are of a specific interest because it is the second most abundant heavy element in the Universe, an important source of opacity and energy production in stars [15], and a major constituent of interstellar dust and organic molecules [16]. Moreover, it plays an important role to constrain chemical evolution models of galaxies [17]. In addition, elements from the second row of the periodic table provide the main cooling channels in the nebulae because they have low-lying excited states with energies accessible by the free electrons thermal energy [18], hence they absorb and re-radiate energy efficiently.

The observed spectrum is a result of the interaction of radiation with the plasma as it travels through a cloud with depth-dependent physical conditions [19]. Cloudy [3] is a good example of a radiative transfer code that would synthesize a spectrum while taking into account the interaction between the gas and the ionizing radiation. Basically, Cloudy breaks the nebula into equidistant zones, and uses the output of the leading zones as an input for the following one. And for each zone the stat-population and ionization-balance equilibria are solved according to the equations described in the previous sections. **Note that the equations above apply for collisional plasma, and are missing the photo-ionization and photo-excitation terms to apply for photoionized plasmas**. The solutions to equilibria equations are used to compute optical depths τ_ν which a parameter determining how much of the radiation will escape before it is re-absorbed by another ion as a function of frequency; of course it will depend on the likelihood of the absorbing transition, but also is proportional to the optical path length so that at zero path length all the radiation would escape and $\tau_\nu = 0$. Thus, the specific intensity of radiation I_ν escaping one zone to the next is:

$$I_\nu(\tau_\nu) = I_\nu(0)e^{-\tau_\nu} + \int_0^{\tau_\nu} S_\nu e^{-(\tau_\nu - \tau'_\nu)} \mathrm{d}\tau'_\nu \tag{1.46}$$

where S_ν is the source function which is a measure of how photons in a light beam are removed and replaced by new photons by the material it passes through.

The basis of radiative transfer theory for photoionized regions is to assume an equilibrium between ionization and recombination. Since approximately 90% of the atoms of the ISM are hydrogen, to a first approximation the equilibrium is studied for a gas made up entirely of hydrogen atoms. Locally one must study the equilibrium between recombination and ionization:

$$n_e n_p \alpha_a(H^0, T_e) = n(H^0) \int_{\nu_o}^{\infty} \frac{4\pi J_\nu}{\hbar\nu} a_\nu \mathrm{d}\nu \tag{1.47}$$

where n_e, n_p, $\mathrm{n(H^0)}$, represent the electron, proton, and neutral hydrogen density, $\alpha_a(H^0; T_e)$ represents the recombination coefficient for hydrogen at a given temperature, $\hbar\nu_o$ the energy required to ionize hydrogen (13.6 eV), J_ν represents the local radiation, and a_ν the ionization cross section of a given photon. In photoionized regions, $\int_{\nu_o}^{\infty} \frac{4\pi J_\nu}{\hbar\nu} a_\nu \mathrm{d}\nu$ dominates over $n_e \alpha_a(H^0, T_e)$ and the ionization fraction is nearly one for most of the volume.

All the above quantities are generally dependant on the physical conditions of the gas: namely electron temperature and density. Nonetheless, the energitics of the photoionized regions is dominated by photoionization and the temperature strongly depends on the physics of photoionization. Hence, the temperature of the gas comes from balance of local cooling and heating processes when in equilibrium. The heating would come mainly from photoionization which will be due to the excess energy of photo ionizing photons beyond the ionizing threshold of the different atoms (13.6 eV for Hydrogen). Consequently, it will be proportional to the number of photoionizing photons and to the temperature of the photoionizing star (energy of the photon). Since Hydrogen comprises the majority of the chemical composition (and Helium is second to it), we expect more than 90 % of the heating to come from Hydrogen and Helium.

On the other hand, the number of photoionizations is equal, when in equilibrium, to the number of recombinations, which in turn is correlated with the density squared for most objects. To balance the heating we need to consider the major sources of cooling. The obvious source would be recombination where the kinetic energy of the captured photon is removed from the gas. However, if one were to simulate a gas made up entirely of Hydrogen and Helium alone, recombination would be the main source of cooling. Since heating is proportional to the temperature of the star, and the cooling is proportional to the temperature of the gas, so equilibrium will be satisfied when these two temperatures are similar. The reality is different than this approximation; ionizing stars of H II regions have temperatures of $T_{star} \sim 30000 - 45000K$, while H II regions often have temperatures of $T_e \sim$ 7000 - 15000 K; central stars of PNe have temperatures of $T_{star} \sim$ 30000 - 200000 K, while PNe often have temperatures of $T_e \sim$ 7000 - 20000 K. The difference is due to the additional cooling produced by forbidden lines excited by collisions.

In general, the intensity of an emission line, I(λ), can be written as:

$$I(\lambda) = \int j_\lambda \mathrm{d}s = \int n(X^+i) n_e \epsilon_\lambda(T_e) \mathrm{d}s \tag{1.48}$$

where j_λ is the emission coefficient, $n(X^+i)$ is the density of the ion that emits the line, n_e is the electron density, and $\epsilon_\lambda(T_e)$ is the emissivity as a function of electron temperature. For recombination, the emissivity is given by:

$$\epsilon_{nn} = \frac{\hbar\nu_{nn}}{4\pi} \alpha_{nn}^{eff} \tag{1.49}$$

where $\hbar\nu_{nn}$ is the energy difference between the two levels and α_λ^{eff} represents the effective recombination coefficient. Whereas, the emissivity of a collisionally excited line is:

$$\epsilon_{kl} = \frac{\hbar\nu_{kl}}{4\pi} f_k A_{kl} \tag{1.50}$$

where f_k is the fraction of ions X^+i in the upper level, k, and A_{kl} is the spontaneous transition probability from level k to l. To compute the emissivity of a collisional lines, one needs to know the population of the upper level. It is necessary to solve the statistical equilibrium equations: the rate of population of a level by radiative and collisional processes is balanced with the rate of de-population by these processes. Optical Recombination Lines (ORLs) are produced when free electrons are captured by ions and descend from excited to lower levels emitting photons in the process. These lines are also known as permitted lines since they typically satisfy all the selection rules for an electric dipole transition. Most of the bright recombination lines in emission spectra are from hydrogen and helium. Metals, such as carbon, nitrogen, and oxygen, also produce recombination lines but are much weaker due to their lower abundances with respect to hydrogen and helium. In contrast with hydrogen and helium, the energies of the first excited levels of some ions of heavy elements are within a few eV of the ground level, which makes it relatively easy to reach them through collisions with electrons. Collisionally Excited Lines (CELs) are produced when the atoms, excited through collisions, decay via radiative transitions. Although the transition probability of these lines is low, the relatively low density of ionized nebulae, allows these transitions to occur. Some of these transitions, the ones produced in the optical range, are forbidden by the parity selection rule ($\Delta l = \pm 1$) and thus, the emitted lines are often called forbidden lines.

Until recently, most of the plasma analysis have been carried out using the intense CELs which govern nebular spectra and typically covers the UV regime; those lines are sensitive to temperature variations and hence can cause large uncertainties in the analysis. On the other hand, ORLs from those elements are less prone to plasma conditions making them more reliable analytic tools [20]. However, the emission in the optical suffers from high opacities

leading to poor signal to noise ratios which poses limits on their measurement. Abundance determinations in photoionized nebulae have long been plagued by an unresolved dichotomy between the abundances derived from forbidden CELs and those from permitted transitions whose upper levels are populated by electron-ion recombination, ORLs. For a given ion, the ORL abundance is significantly larger than the CEL abundance. This so-called abundance discrepancy (AD) problem is quantified by the abundance discrepancy factor (ADF), which is the ratio of the ORL abundance to the CEL abundance for a given ion [21]. The physical conditions of these plasmas are governed by a host of atomic processes (mainly photo-ionization, excitation and recombination). Together, the atomic processes will set the ionization balance and level populations of excited states of ions, and as a result will affect plasma conditions such as electron temperatures and densities. The ADF is quantified as:

$$ADF(X^{+i}) = \frac{X^{+i}_{RLs}}{X^{+i}_{CELs}} \tag{1.51}$$

Where X^{+i} is the fractional abundance of the i^{th} charge state of element X.

1.3 Plasma Diagnostics

This section describes the basic ideas behind some common plasma spectral diagnostics. The idea is that we can take these principles and apply them to other ions/spectra. We will consider diagnostics that use line ratios, however it should be noted that these techniques return line-of-sight averages quantities. For more detailed plasma diagnostics, one often looks at absolute line intensities (not ratios) and couples the analysis with a 3-D model of the plasma.

1.3.1 Electron Temperature Diagnostics

The basic idea is to find a ratio of two spectral lines that is dependent upon electron temperature, but not upon electron density. Specifically under coronal conditions, the ratio of the excited population to the ground population is independent of electron density. Furthermore, one would like the ratio to vary quite strongly with electron temperature. Usually to achieve that, we choose lines that have significantly different dependence on temperature. For example, the excitation energy of level $^1S_0$, from which the [O III] λ4363 line originates, is 5.35 eV. Whereas the excitation energy of level ^1D, from which the [O III] λ5007 line originates, is 2.51 eV. Therefore, the ratio between these two lines tells us about the temperature of the plasma. We expect the intensity ratio of [O III] $\lambda4363/\lambda5007$ to be higher in hotter nebulae.

In coronal conditions, the excited levels are populated by electron collisions directly from the ground (which give rise to CELs), or recombination from the next charge state's ground (which give rise to ORLs). We expect these lines to have a different dependence on temperature since they originate through a completely different mechanism. This is understood because the low energy electrons are more likely to be captured by the ion's potential well as opposed to the fast energetic ones. One the other hand the emissivities of CELs are lowest at low temperatures and increase with temperature. Since the increase in temperature

results in higher collisional rates between ions and electrons, the excited levels will be more abundantly populated.

Thus, a common electron temperature diagnostic is to take the ratio of an excited level that is populated via a forbidden transition to one populated via an allowed transition. This will clearly work particularly well when the populations are close to **coronal** conditions.

Consider the line ratio:

$$\frac{I_{i\to j}}{I_{k\to l}} = \frac{N_i A_{i\to j}}{N_k A_{k\to l}} \tag{1.52}$$

Excited state population of a collisionally excited transition is given by

$$\frac{dN_i}{dt} = N_1 N_e q_{1\to i} - N_i \sum_{j<i} A_{i\to j} \tag{1.53}$$

while the excited state population of a DR or RER transition to a doubly excited state is given by

$$\frac{dN_i}{dt} = N^+ N_e \alpha_i - N_i(\sum_{j<i} A^r_{i\to j} + \sum_{j,i} A^a) \tag{1.54}$$

We set the $dN/dt = 0$ as the excited populations are likely to be in equilibrium with the ground for collisionally activated states and recombination populated states, respectively

$$N_i = \frac{N_1 N_e q_{1\to i}}{\sum_{j<i} A_{i\to j}} \tag{1.55}$$

$$N_i = \frac{N^+ N_e \alpha_i}{(\sum_{j<i} A^r_{i\to j} + \sum_{j,i} A^a)} \tag{1.56}$$

Thus, a line intensity ratio in the coronal approximation is given by

$$\frac{I_{i\to j}}{I_{k\to l}} = \left(\frac{q_{1\to i}(T_e)}{\sum_{j'<i} A_{i\to j'}}\right)\left(\frac{(\sum_{j<i} A^r_{i\to j} + \sum_{j,i} A^a)}{N_e \alpha_i(T_e)}\right)\left(\frac{A_{i\to j}}{A_{k\to l}}\right) \tag{1.57}$$

The only term on the top that varies with electron temperature is the excitation rate coefficients, and in the bottom it is the electron capture rate coefficient. Thus, if one considers an upper level i that is forbidden for excitation from the ground, and an upper level j that is dipole allowed for excitation from the ground, the above ratio will be very temperature sensitive.

1.3.2 Electron Density Diagnostics

By definition, one cannot have a line ratio that is density sensitive in the coronal or LTE regimes. Thus, one looks for lines that are sensitive to collisional redistribution amongst the excited states. For a useful N_e line **ratio** diagnostic, one seeks a line that is insensitive to collisional redistribution (i.e. decays mostly to the ground) and a second line that is sensitive to collisional redistribution. One can often identify potential lines by looking at the excited populations as a function of electron density. All that is required is that the two excited levels behave **differently**.

Ion	Lines		Ion	Lines	
Reddening:		Ratio	T, δT, κ:		T_C
H I	6563/4851	3.0	N II	3063/6584	25,000
He II	1640/4686	6.6	O II	7319/3727	19,600
N II	3063/5755	0.06	O III	4363/5007	32,900
O II	2470/7319	0.30	O III	1664/5007	57,600
O III	2321/4363	0.27	Ne III	3343/3869	43,000
Ne III	1815/3343	1.8	Ne IV	4716/2439	30,500
Ne V	1575/3325	3.0	Ne V	2972/3425	48,400
Ne IV	1609/4724	8.9	S II	4068/6717	13,900
S III	3722/6312	0.57	S III	6312/9532	22,800
Density:		n_{cr}	REL/CEL :		Type
O II	3726/3729	700	C II/C III	7115/1909	RER
C III	1907/1909	40,000	C II/C III	4267/1909	RR
N III	1750/1752	400	C II/C III	4961/1909	DR
N IV	1483/1486	100,000	C III/C IV	1563/1551	RER
O IV	1401/1405	8000	C III/C IV	2297/1551	DR
Ne IV	2422/2425	20,000	O II/O III	4649/5007	DR
S II	6717/6732	500	O III/O IV	2430/1401	RER

Table 1.2: Sample Diagnostic Line Ratios

Table 1.2 gives examples on the common line ratios and their characteristic behaviour. Density-sensitive ratios behave as $n_c r/(n_e + n_c r)$ or as and temperature-sensitive ratios go as $exp(-T_c/T)$. The recombination to CEL ratios should include an RER line, an RR line and a DR line. H alpha/H beta or 1640/4686 can be used for reddening, since they depend weakly on temperature, density and optical depth, but we know those things well enough from other diagnostics. Similarly some of the ratios depend both on density and temperature, but one or the other dominates in the parameter ranges of interest.

1.4 Computational Methods

The theoretical methods required for this paper center upon two aspects of RER: Predicting spectral lines that result from RER and evaluating enhancements to the total recombination rate coefficient caused by RER. As shown by Robicheaux et al. [2], and later used by Pindzola et al. [22], the method of calculating RER rates is analogous to the regular dielectronic capture methodology. For this project two atomic structure codes were modified, the multi-configuration Breit-Pauli atomic structure code AUTOSTRUCTURE [1] and the multi-configuration Dirac-Fock code GRASP [23]

1.4.1 Atomic Data and Analysis Structure (ADAS)

The Atomic Data and Analysis Structure (ADAS) is an interconnected set of computer codes and data collections for modelling the radiating properties of ions and atoms in plasma [24]. It can address plasmas ranging from the interstellar medium through the solar atmosphere and laboratory thermonuclear fusion devices to technological plasmas. ADAS assists in the analysis and interpretation of spectral emission and supports detailed plasma models.

ADAS has a wide range of functionalities, and mainly utilizes collisional radiative theory to generate all the atomic data. I used ADAS for four purposes:

- level population and fundamental atomic data
- Dielectronic rate coefficients
- Ionization equilibrium and power calculations
- Emission lines emissivities and diagnostic line ratios

The code in the ADAS family used for fundamental atomic data calculation is AUTOSTRUCTURE. AUTOSTRUCTURE [24] is a general program for the calculation of

atomic and ionic energy levels, radiative and autoionization rates, and photoionization cross sections in LS or intermediate coupling using non-relativistic (IC) or semi-relativistic (ICR) wavefunctions. It is, in effect, a superset of SUPERSTRUCTURE on which it was initially based. The nuclear charge and the level of accuracy desired determines whether LS, IC or ICR coupling should be chosen. The configurations to be chosen include those for which data is required plus, optionally, additional configurations to improve accuracy - a configuration interaction (CI) expansion. This defines a unique angular algebra problem. The CI expansion is related closely to the choice of radial functions. The better the choice of radial functions, the smaller the CI expansion required to obtain a given level of accuracy which in turn leads to a smaller computational problem. Each (nl) radial function is calculated in a model potential - Thomas-Fermi (TF) or Slater-Type-Orbital (STO). Both contain scaling parameters. These scaling parameters can be optimized automatically by minimizing a weighted sum of term energies chosen by the user. The LS, IC or ICR Hamiltonian is diagonalized to obtain e-energies and e-vectors with which to construct the rates. In the case of autoionization, the target N-electron and (N+1)-electron Hamiltonians are automatically diagonalized separately. The continuum orbitals are (TF or STO) distorted waves, their energy being uniquely determined by energy conservation for a given autoionizing state and continuum.

AUTOSTRUCTURE has numerous control features, one of which is to control the ionization threshold energy relative the ground state. This helps in improving on the accuracy of the atomic structure by matching the models with experimental energies. This will help improve the excited stats' energies and hence their relative transition rates. In the work to be presented later, I used that feature to modify the structure to include below threshold states in the process of DR as part of a RER process; in the next chapter there is a description of the RER process.

ADAS also has post-processors to take the fundamental atomic data generated by AUTOSTRUCTURE to calculate rate coefficient. The total DR rates generated as part of the DR project [1] is one of the most commonly used DR data sets and is considered to be one of the highest quality available. All the radiative and Auger rates are passed in a file to a sub-code for processing to make a total DR rate as a function of temperature. Those files are widely used in the community and in photo-ionization codes like cloudy for plasma modelling. Similarly Maximilian averaged rate coefficient can be calculated for ionization and other recombination processes. All these total rates can be used to calculated the power radiated from these processes and establish the ionization balance between the different charge stages of an element.

The emissivities of each emission lines is archived in the ADAS database as a functions of temperature and density. The actual line intensity would the line emissivites integrated over line of sight. But if we take the ratios of these emissivities, it would represent the actual observed line ratios for a homogeneous plasma. And those can be used for diagnostic as described above.

1.4.2 General-purpose Relativistic Atomic Structure Package (GRASP)

Relativistic atomic theory is known to provide an economically and reliable approach to the estimation of the static and dynamic properties of highly-charged ions. There are, however, numerous other niches in atomic theory where the relativistic formalism is a felicitous choice: for instance, inner-shell processes in heavy atoms, the calculation of term energies to spectroscopic accuracy, and, quite generally, any situation in which strong configuration mixing is evident.

Relativistic atomic orbitals are one-electron spinor eigenfunctions of parity, $\hat{p}$, and angular momentum $\hat{j^2}, \hat{j_z}$. Configuration state functions (CSFs) are built from antisymmetrized

products of such orbitals, and have prescribed coupling scheme, parity, P, and angular momentum J, M quantum numbers. Multiconfiguration atomic state functions (ASFs) are linear combinations of CSFs having common values of P ,J and M. Matrix elements between CSFs are calculated using Racah algebra. Finite-difference methods are used in all operations on radial functions. When the orbital radial functions are specified, the program operates in a configuration-interaction (CI) mode to determine the ASFs and the corresponding energy levels by diagonalizing the Hamiltonian matrix. Radial wavefunctions of a great variety can be generated by the program itself. Most important among these are the extended-average-level (EAL) and the extended-optimal-level (EOL) self-consistent-field (SCF) functions. In the EAL procedure an average-of-configurations approximation is used to define the radial equations, whereas variational optimization on the average energy of a selected subset of ASFs yields the equations in the EOL mode. Only the Coulomb repulsion of the electrons is included in the SCF process. Corrections to the energy levels due to the retarded Coulomb interaction and the polarization of the vacuum by the nuclear charge distribution are included in a perturbation approximation. A rough estimate of the electron self-energy is also made. A modified version of the code was used in this work to calculate high quality Auger rates for below threshold states.

1.4.3 Spectrum modelling and rate code (IDL)

After generating all the data required to make spectral predictions, we need to consolidate all the atomic data and post-process them to generate a spectrum. For that purpose I used Interactive Data Language (IDL) code that I developed for this work. IDL is ideal for these calculations because it is very well integrated with ADAS, and can be used to run some sub-routines of ADAS readily. After considering all the states involved in our intended atomic structure and evaluating their populations and radiative rates we want to calculate their emissivities; and more importantly their relative emissivities because they represent

line ratios. We rely on statistical arguments to determine the likelihood of a certain transition, and conduct branching ratio studies to calculate probabilities of emission for spectral lines. I will describe in detail those calculations and the results of the model in the next chapter.

Chapter 2

Rydberg Enhanced Recombination RER and its rate in plasmas

In photoionized gases, the charge states of each element present are primarily controlled by the balance of photo-ionization which increases the charge state, and electron-recombination which decreases the charge state. The recombination in these photoionized environments can be either radiative recombination or dielectronic recombination. While radiative recombination is well understood, there have historically been large uncertainties in low temperature dielectronic recombination rate coefficients. We explain both recombination processes below, in order to compare them with the newly proposed recombination mechanism. We then outline the theoretical methods used to investigate the implications of RER for photoionized plasma properties.

2.1 Recombination Processes

There are two main recombination processes in plasmas, DR and RR as described previously. Figure 2.1 shows a schematic of the dielectronic recombination mechanism. The classical picture of dielectronic recombination is that a free electron interacts with an atomic ion to form a doubly excited state, which can then decay to a lower level via spontaneous emission, completing the recombination process. The photons emitted in this last stage serve both as evidence that recombination has occurred and as plasma diagnostics [25]. The recombined ion cascades to the ground through a series of radiative decays, accompanied by emission of photons typically in the optical or UV region that give rise to ORLs. Quantum mechanically, the ion is both in the doubly excited state and the continuum state at the same time (i.e in a superposition of the two states), and the radiated photon is what distinguishes these states. The key point is that the regular process of DR has to start from a free electron

(continuum state) which is resonant in energy with a doubly excited state that is above the ionization potential. In Figure 1 this is shown by the blue arrows.

To elaborate on the existing uncertainties in DR rates we give a brief review on the work in the literature. The theoretical calculations often show differences of up to a factor of two between each other, and there are similar differences between measured DR rate coefficients and the theoretical ones currently being used [26]. Theoretical studies of DR for astrophysical applications include the rate coefficient sequence of papers from the DR project [**?**], the sequence work of Gu et al [25], and work focused on both rate coefficients and detailed spectral line emission [27] [28]. It has been found that the theoretical and experimental recombination rates agree closely at high temperatures, but theory generally fails to predict the observed cross sections at the low temperatures that prevail in photoionized plasmas. This is due to that fact that the low-temperature DR rates are dominated by a few low-energy resonances, unlike DR rates in hot collisionally ionized plasma where the large number of resonances at higher energies is what determines the rate. Thus, the large uncertainties at low temperature are largely due to the difficulty in calculating accurate energies for low-lying doubly excited states. It should be pointed out that the measured rate coefficients should be considered the most accurate for the recombination contribution from the positive energy double excited states. Note that this tends to mean calculating doubly or triply excited states involving low n-shells, where there is a lot of Coulomb interaction between the electrons. The resonance positions in the experimental measurements have quite small uncertainties ($\sim 5\%$) which is primarily due to the energy resolution of their electron-beam and lack of plasma effects that are described below, while the uncertainties in the theoretical resonance positions are in general more prevalent. For the theoretical calculations, a small change in the atomic structure can have a large effect, causing a significant change in each resonance recombination rate coefficient leading to a larger aggregate uncertainty.

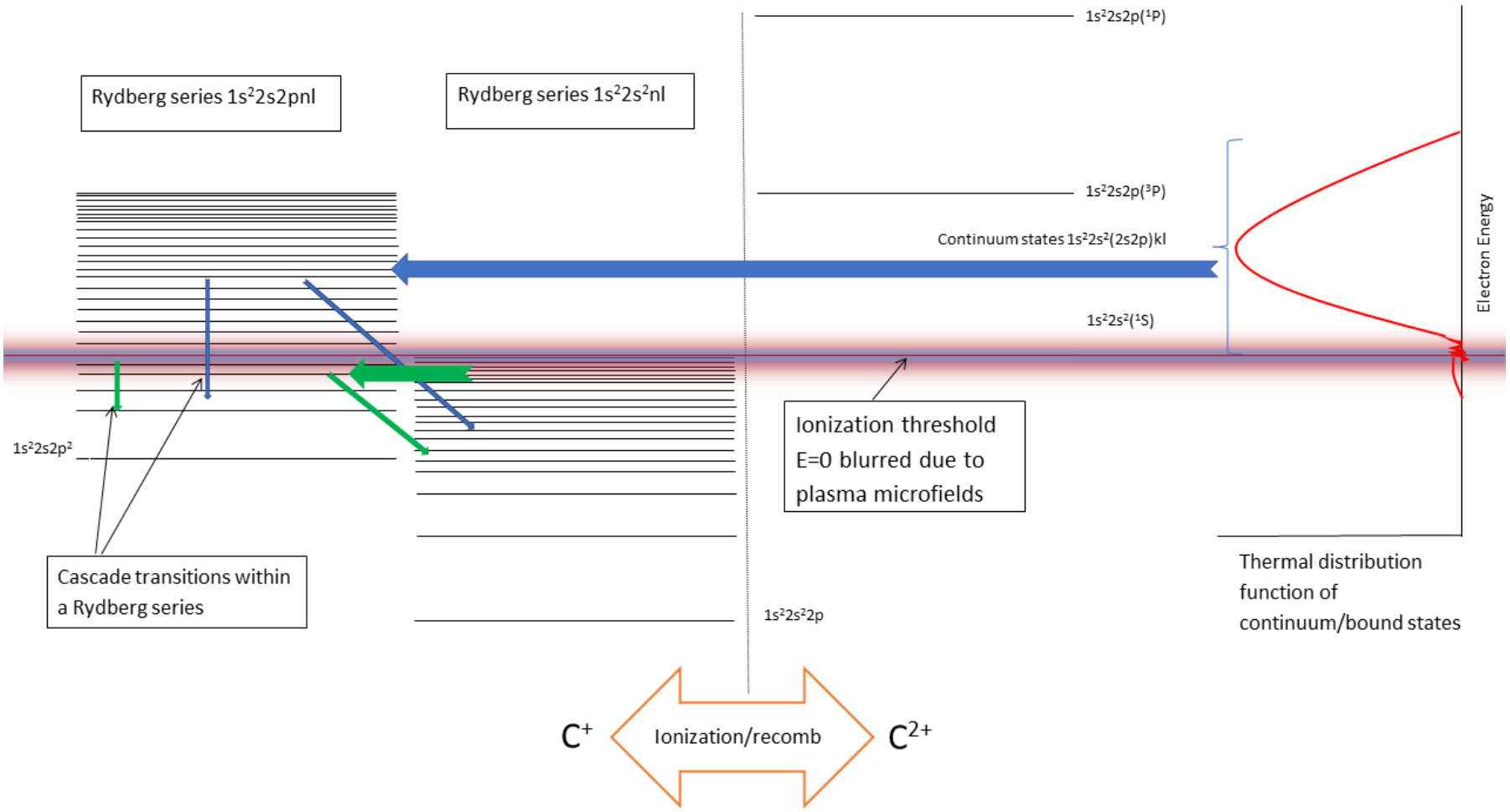

Figure 2.1: Energy level diagram, showing the DR process. The right hand-side shows C^{2+} in the process of recombining into C^{+}. The blurred line representing the ionization threshold (and the ground state of C^{2+}). Two series of energy levels are shown, the singly excited $1s^2 2s^2 nl$ series, and the doubly excited $1s^2 2s 2pnl$ series. On the right-hand side the electron distribution function is shown, extending to energies above and below the ionization potential

Until recently, it was assumed that for dielectronic recombination, that only free electrons can initiate the DR process. The emphasis was on calculating accurate resonance positions to resolve the standing discrepancies in low temperature DR rates; the resolution was not found in that approach, but rather was in an unexpected place. A novel recombination mechanism was proposed by Robicheaux et al [2] that brings a very different perspective to the picture, where the explanation lies in considering plasma effects. The newly proposed process extends the picture of regular DR (which starts from continuum states just above the ionization potential) to include high n-shell bound states that lie just below the ionization potential.

The energy distribution function of free electrons through collisions will smoothly extend to include high-n bound states, see Fig 2.1. This finding is well known in the field of radio astronomy, where emission from very high$-n$ states is observed and used to diagnose plasma parameters such as velocity shifts and temperature maps [29]. The category of states that differ by only the valence electron (nl), with no change in core electron configuration, is called a Rydberg series. The high-Rydberg states can have very large statistical weights, resulting in a large capacity to hold electrons that can contribute to RER transitions. These Rydberg states are also quantum mechanically intertwined with the doubly excited states that are coincident in energy, so they can make a transition to these states, see the green lines in Fig. 1. The inclusion of the few doubly excited states that lie below the ionization threshold can increase DR rates at low temperatures and reduce the sensitivity with respect resonance positions; given that they obtain significant populations and mix well (i.e. large Auger rates) with the neighboring Rydberg states. Robicheax et al [2]found a 1.6 to 2.5-fold increase in the DR rate coefficient of Mg^{8+} at photoionized temperatures.

RER is an outcome of mixing between states, but also a result of the finite density effects of the plasmas. Because the ions in the plasma are in the proximity of other ions

and free electrons, we expect them to interact electrically. This effect can only be experienced locally within the ions, but the overall effect of these fields will cancel and cannot be observed globally, hence they are called plasma microfields [30]. The interaction between the valence electron and the adjacent charges might provide the excess energy needed to free the bound electron or absorb energy enough to entrap free electrons. So, bound states might be considered free momentarily (or vice versa) due to plasma micro-fields, so they will interact with continuum states. Hence, accounting for plasma effects is different from the stand-alone atomic model in that the positions (in energy) of excited states are always fluctuating due to the dynamic environment. That will disturb resonance positions that lie above the threshold, but it will also allow states just below to partake in recombination. Specifically, bound states that are thought to be the final step of recombination are now initiating it. This subtle finding runs against the historical convention that only free states are populated and thus can initiate DR.

2.2 Rydberg Populations and Stimulated Emission

While DR cross sections are converted to plasma rate coefficients via integration over a Maxwellian energy distribution of free electrons, the equivalent for RER is an integral over the populations of the Rydberg states. The rate of collisional events among the ions and electrons increases with the density, but more importantly increases with n-shell. So, the high n-shell states are expected to be mainly populated by collisions and depopulated by mainly by radiative processes and ionization. They will approach the Saha-Boltzmann thermal distribution function value; at which state the high-n populations would be described to be in Local Thermal Equilibrium (LTE). In principle, in LTE the level populations are in equilibrium with the dominant process that populates them, so could be in LTE with the radiation field temperature, with the gas temperature, or with the electron temperature; of course, that assumes that the radiation field is a blackbody described by one temperature. It should

also be noted that the Rydberg populations, as well as providing a source of electrons for RER, will also have their own populations affected by this process. Collisional-radiative theory, along with a modified ADAS code (13), was used to determine the Rydberg populations.

The black line in Fig. 2.2 shows the C^+ Rydberg populations for different densities in terms of b_n (the departure coefficient defined as the ratio between the level populations and their local thermal equilibrium (LTE) value). The highest n-shells are close to LTE, as one would expect, and below about n=200 the populations fall below the LTE value due to less frequent collisions and increased radiative decay. One would expect high-n Rydberg states to tend to their LTE value with increasing n-shell, coming into equilibrium with the Maxwellian free electrons. As an illustration of the effect of doubly excited states on Rydberg populations, the red curve in Fig. 2.2 shows what happens when 5 doubly excited states are allowed to mix with co-energetic Rydberg states, with the mixing being modeled as an enhanced Rydberg radiative rate. This depopulating mechanism leads to a dip in the Rydberg populations for n-shells with the same energy as the doubly excited states. The resulting dip in populations is smoothed out from neighboring Rydberg states through collisions, causing the dips to become both broader and shallower, see Fig 2.2. This effect of collisional distribution is more pronounced for higher densities as expected. DR and RR rates usually have linear dependence on density. It should be noted that the departure factor depends on density. Since the departure factor is included in calculating RER but not DR and RR, we expect RER to have a different dependence on density. This unique feature makes the RER lines an efficient probe of plasma density.

2.3 Transition rates

The method of calculating below threshold transition rates (between Rydberg states and neighboring doubly excited states) has been outlined in [2], and was used to calculate

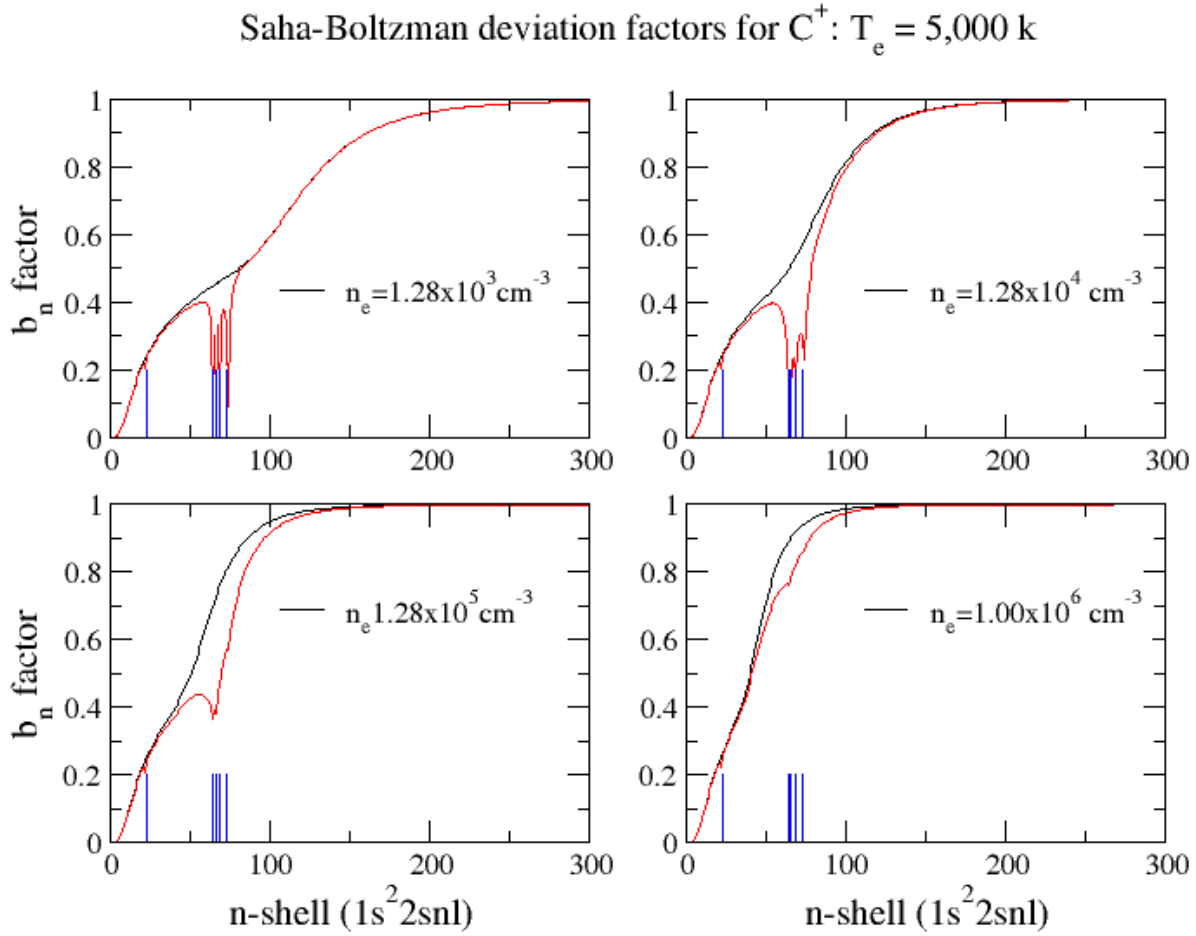

Figure 2.2: Population distribution for C II for Te=10,000 K and a range of electron densities, showing the departure of the n-shell populations from their LTE value. The black dashed line shows the model without the presence of doubly excited states, the red solid line shows the populations when the excited states (blue sticks) are present

rate coefficients for C III in [31]. The method is analogous to the calculation of regular above threshold dielectronic capture rate coefficients, which is due to mixing between a continuum state and a doubly excited state. The transition from a doubly excited state to a Rydberg state would be the analog of Auger breakup for a doubly excited state which makes a transition to a continuum state.

The regular above threshold Auger rate is determined from the configuration interaction between a continuum state and a doubly excited state, due to the electron-electron interaction term in the Hamiltonian operator. This would, for example, give an autoionization rate for a transition from a $1s^2$2s2pnl doubly state to a $1s^2 2s^2$kl continuum state that is at the same energy, provided that the doubly excited state is above the ionization threshold (i.e., it is autoionizing). This process can be extended to the below threshold equivalent by considering the transition from the doubly excited state to a Rydberg state that is coincident in energy, in this case $1s^2$2s2pnl $\rightarrow$1s$^2 2s^2$n'l'. The modification to codes that calculate above threshold Auger rates so that they can calculate the below threshold equivalent is thus to extend the Auger rate calculations to slightly negative energies. Once this has been done, then the inverse process can be calculated via detailed balance. For the cases modelled here, we used a high-n collisional-radiative code (ADAS204, see (14)) to calculate the Rydberg populations for use in the rate coefficient. This gives the population of the Rydberg states relative to their LTE value, and an example of the population results can be seen in Fig. 2.2.

It is very crucial to the quality of the calculation to get the most accurate possible atomic structure and energies; it was shown [32] that the DR rates are very sensitive to resonance positions. The calculation of the Auger and radiative rates for C^+ and the radiative rates for

Element and ion stage	Term (multiplet)	Energy below ionization potential (eV)	Auger rate (s^{-1})	Total radiative rate (s^{-1})
C II	$2s2p(^3P)3d\ (^4D_{1/2})$	-0.01443	2.00×10^8	2.90×10^8
C II	$2s2p(^3P)3d\ (^4D_{3/2})$	-0.013743	1.06×10^8	1.48×10^8
C II	$2s2p(^3P)3d\ (^4D_{5/2})$	-0.012701	1.04×10^8	2.46×10^8
C II	$2s2p(^3P)3d\ (^4D_{7/2})$	-0.011443	5.08×10^8	3.44×10^8
C II	$2s2p(^3P)3d\ (^4F_{3/2})$	-0.114273	1.20×10^5	8.62×10^7
C II	$2s2p(^3P)3d\ (^4F_{5/2})$	-0.11268	5.25×10^8	1.58×10^6
C II	$2s2p(^3P)3d\ (^4F_{7/2})$	-0.110162	7.40×10^8	2.53×10^6
C II	$2s2p(^3P)3d\ (^4F_{9/2})$	-0.112927	0.00	0.00
C III	$1s^22p4d\ (^1D_2)$	-0.05254	1.41×10^{13}	2.41×10^9
C III	$1s^22p4d\ (^3F_2)$	-0.05148	1.90×10^{14}	1.27×10^9
C III	$1s^22p4d\ (^3F_3)$	-0.05148	1.90×10^{14}	1.18×10^9
C III	$1s^22p4d\ (^3F_4)$	-0.05148	1.90×10^{14}	1.50×10^9
C III	$1s^22p4d\ (^1D_2)$	-0.07475	2.87×10^{13}	1.55×10^9

Table 2.1: Calculated transition rates

C^{2+} were computed using AUTOSTRUCTURE and the Auger rates for C^{2+} were calculated using GRASP taken from [31]. These rates are listed in table 2.1 below.

2.4 DR Rate coefficients

The total DR rate coefficient between two ion stages is defined as:

$$\alpha_{DR} = \frac{4\pi a_o^2 I_H}{k_B T_e}^{3/2} \sum_j \frac{w_j}{2w_i} e^{-E_r/k_b T_e} \sum_l A^a_{j,Er} \frac{A^r_{j\to l}}{\sum_h A^r_{j\to h} + \sum_m A^a_{j\to m}} \tag{2.1}$$

where a_0 is the Bohr radius, I_H is Rydberg constant, k_B is Boltzmann constant, T_e is the electron temperature, w_i and w_j are the statistical weights of the capturing resonance state (j) and the initial state (i) of the recombining ion, E_r is the the energy of the resonance state j,A^r and A^a are radiative and Auger rates. The first summation is over the possible resonance states (j) (doubly-excited states), the second one is over all possible bound states that the captured electron can stabilize to. The summations over h and m are other Auger and radiative channels. Equation 2.1 is the traditional definition for DR rate coefficient.

The theoretical modeling required for this work was the calculation of total recombination rate coefficients which include the effects of RER. This is then simply a sum over all of the capture into the doubly excited states that lie just below the ionization potential. The inclusion of the few doubly excited states that lie below the ionization threshold can increase DR rates at low temperatures and reduce the sensitivity of DR rates with respect to resonance positions; given that they obtain significant populations and mix well (i.e. have high Auger rates) with the neighboring Rydberg states; the difference is in the population distribution. Instead of using Maxwell distribution, the distribution for below-threshold resonance is $e^{-E_r/k_bT_e} \times f_{T_e,D}(E_r)$; where $f_{T_e,D}(E_r)$ is called the deviation of the below threshold distribution from the Saha-Boltzman bound state distribution as described in the previous section.

Robicheax et al. [2] found a 1.6 to 2.5-fold increase in the DR rate coefficient of Mg^{8+} at photoionized temperatures. Fig. 2.4 shows an example of the enhancement in the recombination rate coefficient of C III, due to RER. We compare different calculations of total DR rates for these ions along with measured rates from experiment; it is worth mentioning that the recommended rate would be the experimental measurements supplemented by below threshold DR. It is evident that all techniques used to obtain the total DR rates agree at high temperatures (above 40,000K). For temperatures below 20,000K, we start to see considerable disagreement due to a combination of many factors (the capture rates and their constituent parts). Particularly, below temperatures around 2,000K the DR rate is dominated by below-threshold resonances, and RER produces rates that are orders of magnitude higher than conventional processes.

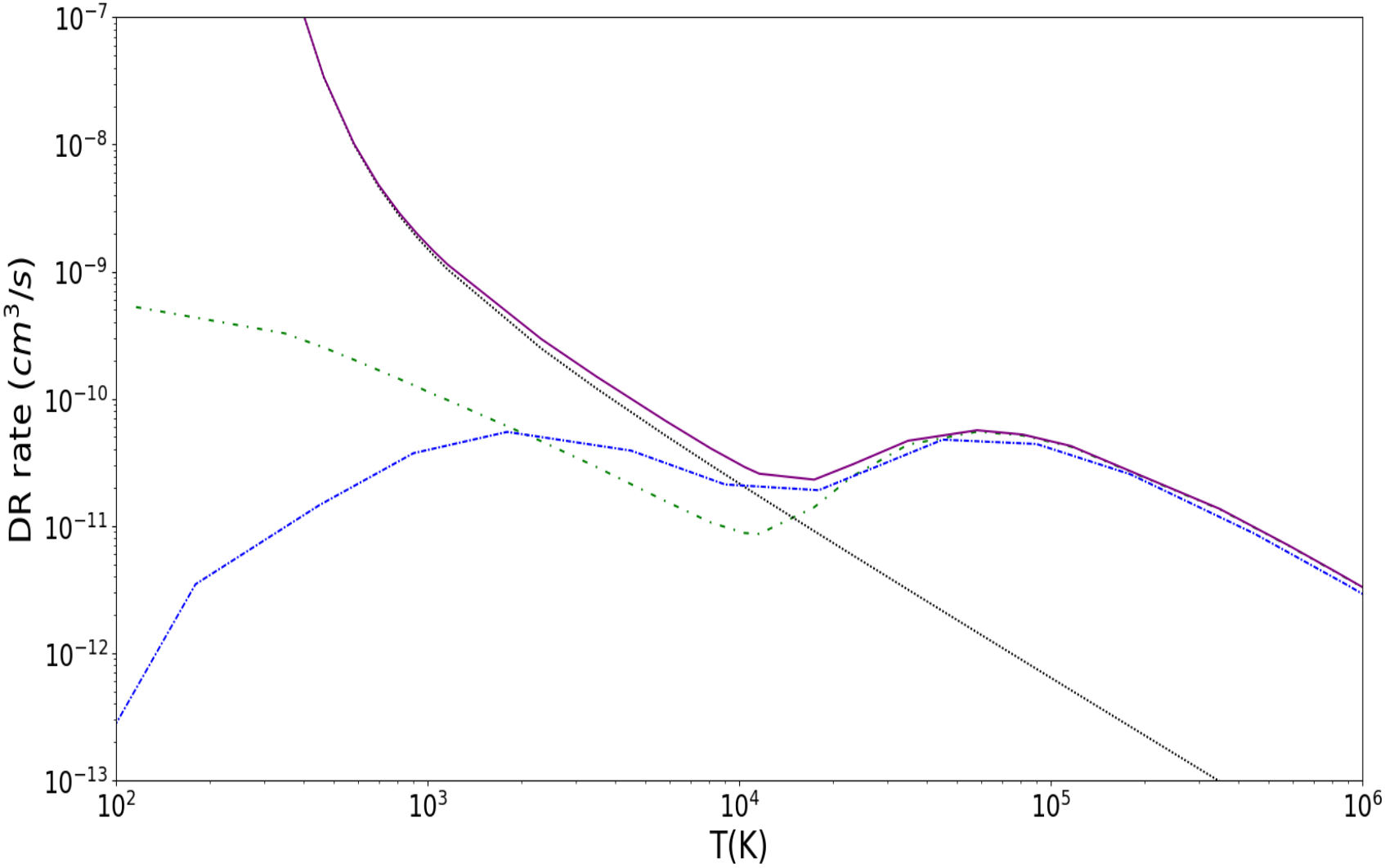

Figure 2.3: Comparison amongst C III DR rates from the literature. The green curve represents Badnell et al [1]. calculated rates, the blue curve is our calculated rates for above threshold DR only, and the black curve is our calculated DR rates due to RER only. The purple curve is the recommended total rates produced by combining the measured DR rates with the RER contribution.

2.5 Branching Ratios and generating a spectrum

The calculation of spectral lines associated with RER also requires the calculation of spontaneous emission rates. These are calculated from AUTOSTRUCTURE and GRASP. Thus, the intensity of a spectral line associated with RER is the transition rate coefficient between the Rydberg states and the doubly excited states, multiplied by a branching ratio for spontaneous emission. We developed a code that used the rates from the AUTOSTRUCTURE or GRASP calculations to make a synthetic spectrum for the ions of interest in this project. Note that more accurate wavelengths for the transitions that we are interested in can be obtained from the NIST database, thus the NIST energies were used in the calculation of the wavelengths of the lines, and the rates from AUTOSTRUCTURE or GRASP were used in the calculation of the strengths of the lines.

In the evaluation of the intensities of the spectral lines from the near threshold doubly excited states, the populations are evaluated assuming that the dominant populating mechanism is dielectronic capture (or the below threshold equivalent RER), and the de-populating mechanisms are all of the radiative decay channels and Auger breakup (or the below threshold equivalent). This is the approximation made for satellite line emission and is equivalent to the assumption that there is no collisional-redistribution of the populations in the doubly excited states. This is because the Auger rates are much faster that the collisional rates, so they dominate the populating mechanism. The steady state value for the doubly excited state population is thus determined via

$$N_i = \frac{N_{Ryd}\alpha_i}{\sum A^a + \sum A^r} \tag{2.2}$$

Where N_{Ryd} is the population of the Rydberg state that is coincident in energy with the doubly excited state N_i. The Auger rates were evaluated using a modified version of the GRASP relativistic atomic structure package (for CIII) and a modified version of the

AUTOSTRUCTURE for C II. The C III results using GRASP have been published previously [31] and the C II results were generated as part of this work. For the C II calculated Auger rates care was taken on the atomic structure calculation to get the energies of the near threshold doubly excited states as close as possible to the NIST energies. Differences were usually less than 5%, and we performed some studies looking at the sensitivity of the below threshold Auger rates to the uncertainties in the resonance positions, finding that the rates did not dramatically change, with the average change being about 15% and the largest one changing by a maximum of 45%.

In the evaluation of the collisionally excited line intensities (e.g., Fig 3.2) we used a full collisional-radiative model with excitation, ionization, recombination, and spontaneous emission processes included. One of the ADAS codes (ADAS208) was used to produce the photon emissivities that were used for our line intensities. This was based upon large-scale atomic calculations for the fundamental atomic data.

The line intensities follow from the calculation of the excited state populations, both for the CELs and for the RER lines. In this project we use photon emissivity coefficients (PECs) in the spectral analysis (Fig 2.4), with units of $photons cm^3\ s^{-1}$. The PEC is defined as:

$$PEC_{i\to j} = \frac{N_i^{exc}}{N_i} A_{i\to j} \tag{2.3}$$

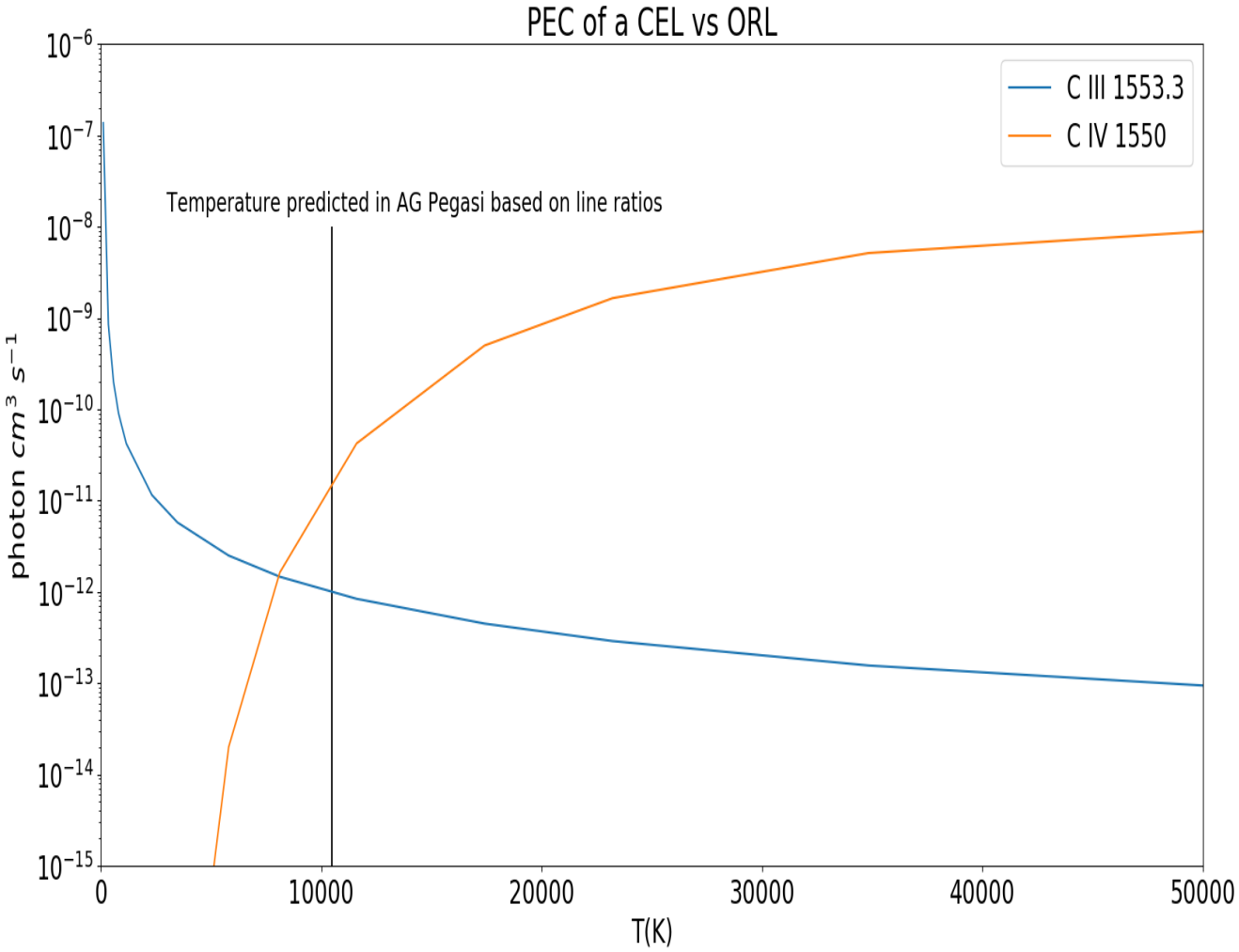

Figure 2.4: Plot showing the PECs of a CEL (C IV resonance line at 1550 Å) and an ORL (C III RER line at 1553 Å) as a function of temperature. Note that the vertical line represents the ratio observed in AG Pegasi as described in chapter 3

Chapter 3

The spectroscopic search for evidence of Rydberg Enhanced Recombination

3.1 Prediction of RER emission lines

Due to the potential importance of RER, it becomes critical to make some observational predictions of the mechanism, and to verify or refute it with experiment. In order to predict observable properties of RER, we established criteria to identify transitions whose upper levels are likely populated by RER. Specifically, the doubly excited states must i) be propinquitous to the ionization threshold to insure significant population; ii) adequately overlap with high Rydberg states, resulting in large mixing rates with the doubly excited states; iii) be from an ion widely observed in astrophysical nebulae; and iv) produce relatively strong emission in the available high-resolution spectra of suitable PNe. We searched the first two rows of the periodic table up to sulphur for candidates that fit these criteria, and found that C II, C III, O II, and O III are the most promising. Oxygen and carbon are the most abundant elements in the Universe other than Hydrogen and Helium and play a major role in the cooling of photoionized nebulae. While we focus on Carbon and Oxygen for this study, Nitrogen and Neon ions may also be affected by RER. In general, relatively simple ions of heavy elements (open sub-shell with one or two valence electrons) have a few resonances near the threshold, hence omitting some of them that lie below the threshold will significantly change DR rates. That is different from complex ions that include a forest of resonances around the threshold, and each individually will have negligible effect on DR rates if omitted. So, some of these lines are of measurable intensity with predicted emission in the optical. Table 3.1 shows the list of doubly excited states that were selected for the study.

Element and ion stage	Term (multiplet) Term (multiplet)	Energy below ionization potential (eV)	Wavelength of strongest transitions (Å)
C II	$1s^2 2s2p(^3P)3d\ (^4D)$	0.010097 -0.011355	651.21 -651.39
C II	$1s^2 2s2p(^3P)3d\ (^4F)$	0.105355-0.112927	**7115.53**,7134.03, **7112.94**,**7119.73**
C III	$1s^2 2p4p\ (^1D)$	0.07475-0.05254	1581.43,416.77, 1623.25,1512.93
C III	$1s^2 2p4p\ (^3F)$	0.05148	1593.65,1594.27, 2799.19,**1553.38**
O II	$1s^2 2s^2 2p^2(^1S)4s\ (^2S)$	0.130312	413.65
O II	$1s^2 2s^2 2p^2(^1D)5s\ (^2D)$	0.635618	397.9, 420.7
O III	$1s^2 2s^2 2p^2(^4P)4p\ (^3D)$	0.04554	225.9, 671.8
O III	$1s^2 2s^2 2p^2(^4P)4p\ (^5P)$	0.45183-0.59911	2430.3,2427.7,2287 2285.9,2286.4,2288.9

Table 3.1: C and O transitions and energies arising from RER. UV wavelengths are in vacuum, optical wavelengths in air. Observed lines are highlighted in bold

We modeled the spectrum of C II and C III with all of the RER transitions to guide our search. While the proposed lines in Table 3.1 (non-bold) are promising for future investigations, we faced some difficulties in detecting their spectral signatures related to their weak emission and/or blending with lines around them. Hence, we require high-resolution spectra to detect the desired lines accurately. There is a dearth of high-resolution UV spectra other than the UV spectrometers on Hubble Space Telescope (HST) which adds a constraint on our search. We restricted the predicted transitions to the ones that are most probable (i.e. corresponding to transitions with large branching ratio) and hence most intense in the spectrum. This in turn led to two lines of C II at 7112.94 Åand 7115.53 Åthat we searched for in high resolution optical spectra, and one C III line at 1553.8 Åthat we searched for in UV spectra.

3.2 Observational Evidence for RER

The optical C II RER lines are expected to be relatively weak, compared to the UV transitions (Table 3.1) due to their transition probabilities. High-resolution spectroscopy is critically important for identifying these lines, both to resolve these lines from features of other species and to provide greater line-to-continuum contrast. Because of their high surface brightness's compared to H II regions (making weak emission lines more easily detected), PNe are natural laboratories in which to search for evidence of RER.

Thus, we selected eight PNe with deep, high resolution spectra to look for optical C II lines produced by RER: IC 418; IC 2501, IC 4191, NGC 2440, NGC 7027 [33]; NGC 3918 [34]; NGC 6369 and an unpublished spectrum of Hb 12, taken with the 2D-coud echelle spectrograph on the 2.7-m Harlan J. Smith Telescope at McDonald Observatory [35]. The spectra of six of these objects, showing the C II RER lines, are shown in Fig. 3.1.

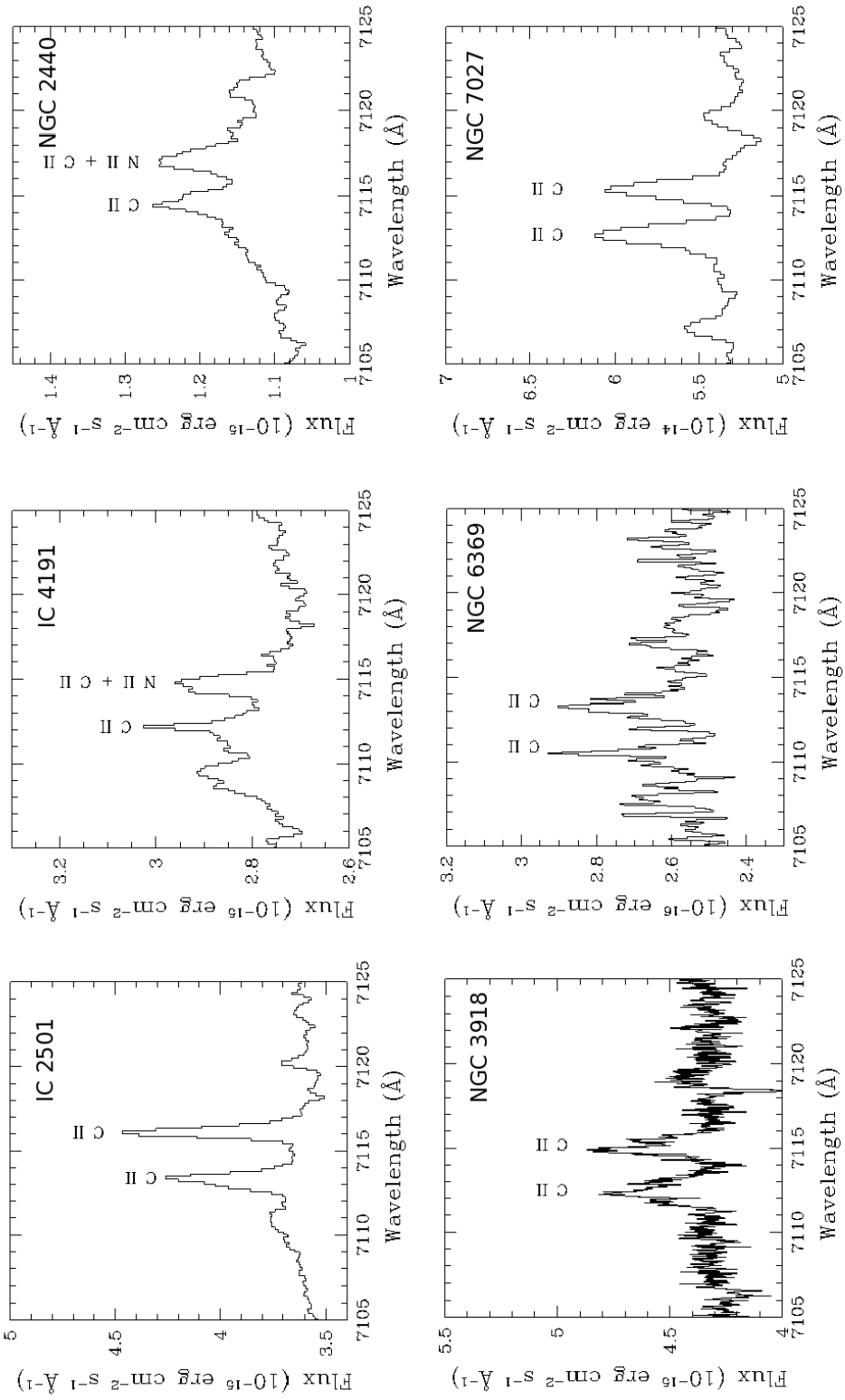

Figure 3.1: Portion of the high-resolution spectra showing the C II satellite lines at 7112 and 7115 Åfor 6 PNe and C III line at 1553 Å. From left to right and from top to bottom: IC 2501, IC 4191, NGC 2440, NGC 3918, NGC 6369 and NGC 7027

To verify the identity of the C II RER lines, we utilized the Atomic Line List (v2.05b21; http://www.pa.uky.edu/∼peter/newpage/) to search for other possible identifications with rest wavelengths within 1 Å of the RER lines. We considered forbidden transitions of atomic ions with excitation energies below 10 eV (collisional excitation to more energetic states is negligible at the electron temperatures, typically $\leq 1.3eV$, of PNe), as well as permitted transitions of elements in the first three rows of the periodic table. For possible alternative identifications, we searched for multiplet members, lines from the same upper level, and in the case of forbidden transitions of iron-peak elements, the strongest optical lines expected given the physical conditions of the nebulae.

As an example, possible alternative identifications for C II 7112.94 Å include Ne II 7112.70 Å, C IV 7112.40 Å, Si I 7112.80 Å, C I 7113.18 Å, N II 7113.50 Å, and Ne III 7113.50 Å. We dismissed the majority of these identifications given the lack of multiplet members or lines from the same upper level in the observed spectra. The most plausible alternative identification is C I 7113.18 Å, which has multiplet lines at 7111.47 , 7115.17, 7122.20, 7132.11, and 7139.18 Å. In Hb 12, a line at 7110.86 Åwas detected, but is likely [Cr IV] based on the presence of several other [Cr IV] lines in the spectrum. None of the other C I multiplet members were detected in any object in our sample with the exception of a feature near 7115.5 Å, which is likely C II 7115.53 Å (Table 3.1). If the identification was in fact C I, we would expect that the disagreement between the observed and modeled intensity ratio of 7112.94 and 7115.53 Åwould correlate with the ionization level of the PN. That is, low-ionization PNe such as Hb 12, IC 418, and IC 2501, with a larger reservoir of near-neutral ions, would show larger disagreement with model predictions than higher excitation PNe such as NGC 2440, NGC 3918, and NGC 7027. However, no such correlation was found.

Similarly, no viable alternative identifications were found for the 7115.53 Åline. These arguments, and the detection of multiple lines from this C II multiplet, support our identification

of the 7112.94 and 7115.53 Åfeatures as the C II RER transitions. We also examined candidate C II RER lines at other wavelengths, including 6724.54, 6742.43, and 6755.13 Å. These lines are expected to be much weaker than those listed in Table 3.1, due to their radiative rates and branching ratios, but features near these wavelengths were detected in the spectra of some of the PNe we examined. Our vetting process indicated that other identifications (e.g., [Cr II] 6724.85 and He I 6755.85 Å) are more likely, or an insufficient amount of evidence available for the C II identification (e.g., no multiplet members detected) precluded an unambiguous identification.

Using this method, we ruled out alternative identifications of the 7112.44 and 7115.53 Å features. Storey et al [36] also identified two lines at these wavelengths as being C II lines. Based on our line vetting criteria and the detection of multiple members of the multiplet, we are confident that C II 7112.94 and 7115.53 Å emission has been detected in each of the seven PNe that we studied. The populating mechanisms competing with RER for the observed lines are discussed in the next section.

3.3 Competing mechanisms for populating the C II lines

The next step in the processes of verifying the lines was to check that these C II lines are produced by RER and not another mechanism. Fluorescence is highly unlikely to populate these doubly excited states due to the lack of wavefunction overlap between the studied doubly excited states and ground (or metastable) states. In addition, selection rules eliminate the possibility of direct excitation and impose low photon absorption rates. Alternatively, cascade from higher (i.e., above threshold) doubly excited states in the same Rydberg series (e.g. $1s^2 2s2pnl$) can provide a populating mechanism. These above-threshold doubly excited states are populated by DR. To quantify the effect of populating the levels of interest ($1s^2 2s2pnl\,^4D$ and ^4F) due to above threshold cascades down (see Fig. 2.1), we looked for

the spectral lines that cascade to the upper levels of the two lines of interest.

The two C II lines shown in Fig. 3.1, have upper levels with two different J-values in the $1s^2 2s2p3d(^4F)$ term. These two upper levels are in turn populated via cascades from the $1s^2 2s2p4f(^4G)$ and $1s^2 2s2p4p(^4D)$ terms. There are two main cascade lines that can populate either the upper levels of the 7112.94 and 7115.53 Å lines; C II 3876 and C II 5259 Å which are both blends of three spectral lines. Using radiative branching ratios, we determined what fraction of each of these blended cascade lines will populate each of our two lines of interest. We want to determine if RER contribution is sufficiently large to populate the upper levels of 7112.94 and 7115.53 Å lines. We note that Sochi et al [27] have calculated effective DR rate coefficients into the upper level of the lines 7112.94 and 7115.53 Å, due solely to cascades from higher levels. Our rate coefficients due to cascades are very close to those calculated by Sochi et al. Let Path A be the population of the near-threshold state by cascade from a higher energy state in the same Rydberg series, and Path B be direct population via RER. We find that at temperatures below 1 eV, path B is the major channel to populate the near-threshold doubly-excited states (the ratio Path A / Path B = 0.01 - 0.25). The contribution from path A increases with temperature, and the ratio quickly becomes larger than one for temperatures above 1.5 eV. This is as one might expect, since the first step of path A requires DR to high energy states, and at low temperatures to these states capture into these states will be negligible. These results are for a simplistic model (homogeneous density and temperature plasma) and should be considered as a guide for the observations of the cascade contribution, and an indication that cascade contributions are possible.

Our determination of the cascade contribution to the observed lines was then based purely upon the observed fluxes of the cascade lines, as this is a model-independent method of checking the cascade contribution. Table 3.2 shows the observed intensities of the 7112.94

and 7115.53 Å lines in the eight PNe investigated, along with the observed intensities of the cascade lines. The table provides an estimate of the cascade contribution to the observed lines, based upon the observed cascade intensities and radiative branching ratios that connect these lines to the observed lines in question. In five of the cases (NGC 6369, NGC 7027, NGC 2440, NGC 3918 and Hb-12), the cascade contribution was either too small to detect, or too weak to explain the observed intensities shown in Fig. 3.1. ***Thus, we believe that these five detections are the first direct evidence of RER***. In two cases, the cascade contribution was close to the observed intensity in the two lines, indicating that RER is a lesser contribution to the line intensity. There is one particular case, IC 4191, that shows an extremely exaggerated intensity of the cascade lines as compared to the C II 7115 Å(15 times higher) which tells us that in this case the cascade lines are either blended with other lines or mis-identified. This is indicated as a negative percentage in the table.

PN	I(7115) / I(H) x 100	I(3876)/ I(H) x 100	I(5259)/ I(H) x 100	Contribution limit for RER to I(7115)
NGC6369	$1.1 \pm 0.44 \times 10^{-2}$	Not detected	Not detected	100%
HB-1	$4.48 \pm 0.9 \times 10^{-3}$	Not detected	Not detected	100%
IC418	$74.30 \pm 0.86 \times 10^{-3}$	$6.9 \pm 1.38 \times 10^{-3}$	$6.3 \pm 1.26 \times 10^{-3}$	-34%
IC2501	$79.80 \pm 1.96 \times 10^{-3}$	$1.4 \pm 0.15 \times 10^{-2}$	$5 \pm 1 \times 10^{-3}$	22%
IC4191	$3.1 \pm 0.62 \times 10^{-3}$	$9.60\pm 1.01 \times 10^{-2}$	Not detected	-1000%
NGC2440	$2.3 \pm 0.253 \times 10^{-2}$	Not detected	$3.6 \pm 0.72 \times 10^{-3}$	92%
NGC3918	$6.8 \pm 1.36 \times 10^{-3}$	Not detected	Not detected	100%
NGC7027	$1.47 \pm 0.16 \times 10^{-2}$	Not detected	$7.9 \pm 1.58 \times 10^{-3}$	72%

Table 3.2: A table showing the observed RER line (7115 Å) intensity along with the cascade lines (3876 Å and 5259 Å) that correspond the competing mechanism to produce the RER lines. The estimated contribution of RER on the line as a percentage is reported in the last column

The five PNe with no or little cascade contribution are consistent with the above theoretical conclusion about RER as the temperatures expected in them are $\sim 1eV$. Hence, the other three PNe have line intensities that cannot be reproduced adequately with our simple model (which assumes a spherically uniform gas) but need depth-dependent radiative

transfer modelling. A full model of RER lines in photoionized models (such as Cloudy) requires the addition of multiple RER-modified recombination rates for many ions and charge states, along with an accurate description of the boundary conditions and plasma parameters.

Uncertainties

There are inherent sources of error in this study that come from both theory and observation. The optical C II emission lines produced by RER tend to be weak, and the error bars on their observed intensities are 20-25% in the objects investigated. Moreover, flux calibrations for cross-dispersed echelle spectra are non-trivial and can lead to additional uncertainties in the line intensities. From the atomic physics point of view, the Auger rates have significant uncertainties depending on the coupling model and the accuracy of the atomic structure (Breit-Pauli Hamiltonian for the AUTOSTRUCTURE calculations or the Dirac Hamiltonian for the GRASP code) adopted to compute them (we estimate this to be 30%). There is also some uncertainty in the radiative branching ratios, which again come from uncertainties in the structure calculations. There are not any NIST A-values to compare with for these high-lying transitions, but we estimate the uncertainty on the A-values to be about 10-20% for these electric dipole transitions. The larger uncertainty in our simulated RER line intensities and the modified recombination rate coefficients is likely due to the uncertainty in the Rydberg populations. These were estimated from a collisional-radiative calculation and require accurate knowledge of the plasma conditions in the regions of emission. Thus, the expected uncertainty in the predicted emissivities for the RER lines is a maximum of 40%.

3.3.1 Evidence at Ultraviolet Wavelengths

Moreover, the effect of RER is expected to extend to many astrophysical objects that exhibit low-temperature plasma; one of which is Symbiotic star systems. They are binary

star systems with typically a white dwarf accreting a red-giant star from which we observe traces of C III 1553.38 Åin the spectra of multiple systems. The spectra that were recorded with the IUE spectrometer have low resolution which causes the interpretation of such a weak line to be rather inaccurate and incomplete; observations with HST are required to compare line intensities. The emission from these plasmas (other than that coming from the stars) is from the surrounding gas to the stars, and its either from the dense white dwarf wind, the red-giant upper atmosphere, or the nebula around the system. One of systems of strong relevance is the AG Pegasi Symbiotic system. This system has experienced a drastic change in the luminosity and as a result the spectral features underwent a transformation that can be traced to their originating mechanism. Between the years 1984-1994 the systems luminosity decreased by four magnitudes as a result of the expanding stellar atmosphere of the white dwarf [37]. Consequently, more UV radiation would reach the red-giant upper atmosphere, changing the emission features.

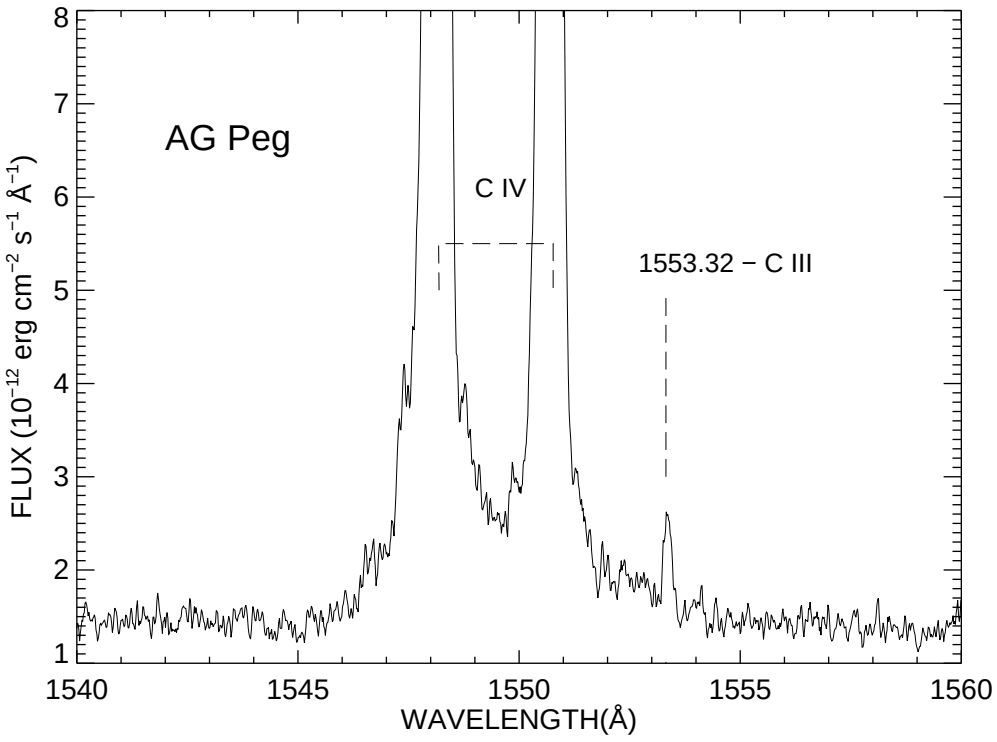

Figure 3.2: Sample UV spectrum for AG Pegasi showing the C III 1553 Å line taken from HST archive

The observed spectrum of AG Pegasi during the diminish in luminosity indicates that the broad line features, coming from the dense white dwarf winds, is gradually replaced by narrower emission that emits from a plasma with different temperature and density; namely the upper atmosphere of the red-giant. Accordingly, the C III 1553.8 ÅRER line was blended within the strong broad resonance emission from C VI 1550.4 Åprior to 1981, and progressively the width of the resonance line decreased to reveal the RER line as in Fig 3.2. The lower resolution of the IUE also makes it challenging to detect the other RER UV lines as they are blended with other strong features. There was one observation performed on the system using the HST high-resolution GHRS spectrometer that revealed the line very clearly [37]. Eriksson et al were not able to identify the line as coming from the score of the other ionic species of heavy elements and iron whose lines were observed. Using the reported relative heights of the C III lines observed by HST and the widths of these lines we were able to estimate that the observed line is the C III 1553.38 Åand that it comes from a $\sim 11,000K$ plasma which fits well with other assumptions about the origin of the C IV resonance lines.

In summary, we have confirmed the identity of C II lines that are populated by RER in all eight (5 of them with dominant contribution and 2 with partial contribution) of the PNe we investigated and ruled out other mechanisms for producing these features. We also observed the C III line in the spectrum of AG Pegasi. This is the first direct astronomical evidence of the RER mechanism, which has several implications for nebular astrophysics as discussed in the next section.

Chapter 4

The effects of RER for photo-ionized plasmas: discussion on potential impact on current discrepancies in planetary nebulae

Near threshold doubly-excited states and the RER mechanism have a large number of implications for astrophysical plasmas. We subdivide this section into two topics for consideration: The role of enhanced recombination for plasma modelling, and the implications of RER for spectroscopy.

4.1 Plasma modelling and Rydberg Enhanced Recombination

The collective effect of RER on plasmas is to increase the overall recombination of ions with electrons. That in turn lowers the ionization state of abundant elements with temperatures and charge states which sample the enhanced recombination rates. Moreover, elements from the second row of the periodic table provide the main cooling channels in the nebulae because they have low-lying excited states with energies accessible by the free electrons thermal energy [18], hence they absorb and re-radiate energy effectively. Consequently, RER is expected to change the cooling rate in the regions of the plasma where it prevails as a result of changing the abundances of main coolants.

Accordingly, if below-threshold transitions are not accounted for in models of photo-ionized plasma regions, the ionization equilibrium solutions will incorrectly predict higher ionization states in the plasma. Ferland et al. [19] argued that the lack of reliable DR rates is the dominant uncertainty in ionization balance calculations of photo-ionized plasmas. In addition, determination of fractional abundances of some ions will influence many abundance ratios (e.g Si/C ratio); these ratios are often used to constrain the Intergalactic medium

(IGM) models. Savin et al. [38] showed that uncertainties in existing DR rates, related to Si/C ratio, will limit our ability to constrain the chemical abundances and the shape of the metagalactic radiation field at high redshift.

To demonstrate the effect of RER to the ionization balance in the plasma, we conducted a simulation on Cloudy using the new DR rates for C II and C III in a test model of a PN from Cloudy. The boundary conditions are similar to those for the Paris meeting PN, a homogeneous grain-free PN. We introduced density fluctuations, creating two regions with mild contrast in density (10000 – 1000 cm^{-3}). For more information about the suite refer to this file in the Cloudy documentation: `<c17.01/tsuite/auto/doc_tsuite.htm>`. From Fig. 4.1 we can see the sizable shift in the fractional depth-dependent fractional abundance curves of C II and C III as a result of enhanced recombination. This change indicates the potential effect of RER on the Carbon ionization balance. Thus, to get an accurate estimate of the change in the overall conditions we need to include enhanced rates for all the ions of the most abundant elements.

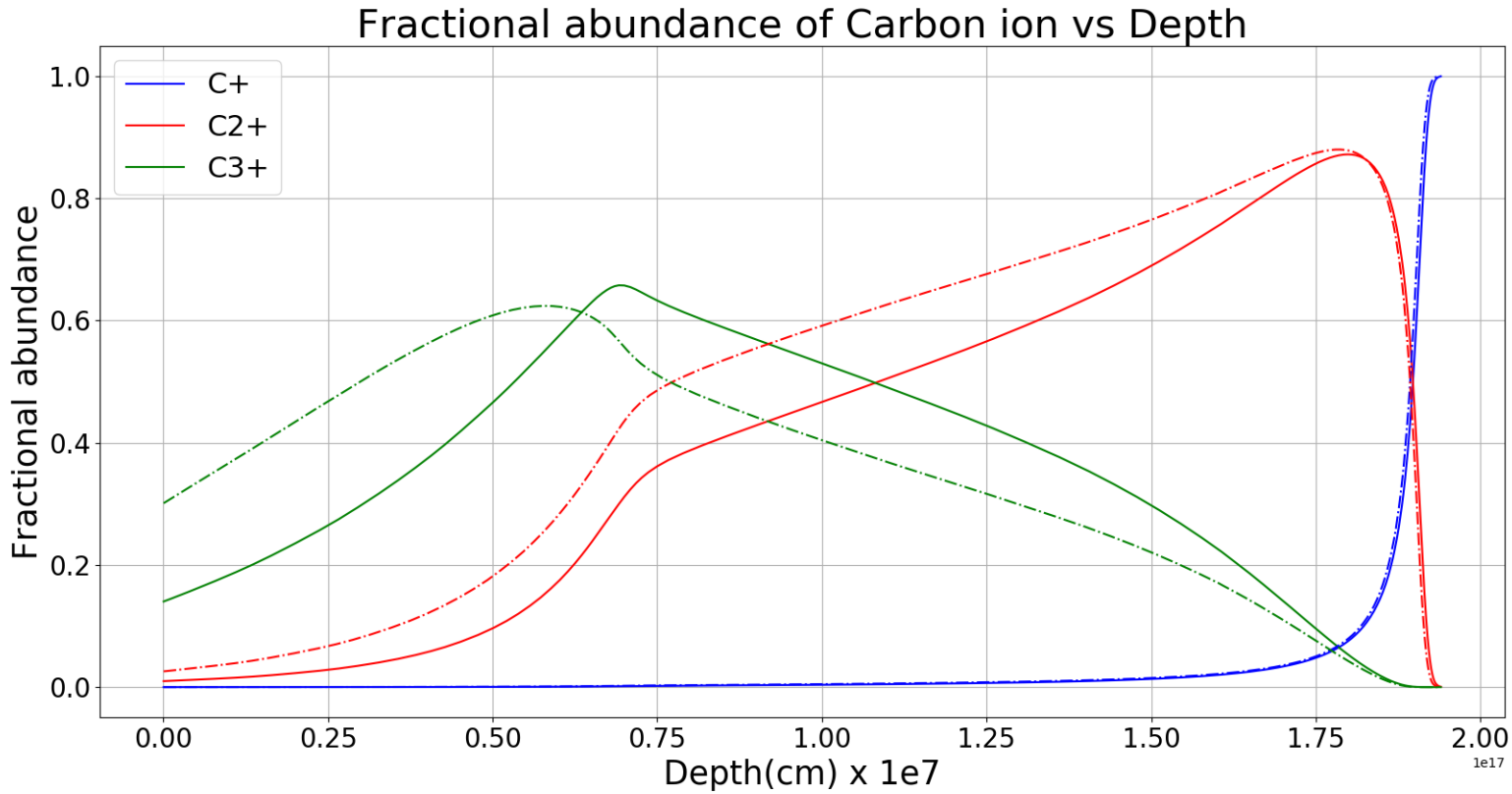

Figure 4.1: Fractional abundances of carbon ions as a function of depth in the PN test suite. The blue curve is C^{+}, red is C^{2+} and the green curve is C^{3+}. The solid curves represent the abundances with old rates (without RER) and the dashed curves are obtained using new rates (with RER)

4.2 Abundance Discrepancy problem

Abundance discrepancies have been studied in planetary nebulae (PNe), the ionized ejecta of dying low-mass stars (1 8 M_sun; [20], [39], and references therein) and in H II regions (photoionized gas surrounding newly formed massive stars; [40], and references therein). ADFs of 1.5-3 have been found in H II regions and most PNe, but about 10-15% of PNe exhibit substantially larger ADFs of 10-100 ([41], and references therein). The ADF for O^{2+} is the most well-studied since O II lines are the brightest ORLs and both O II and [O III] lines are present in optical spectra. But with the aid of UV spectroscopy and very deep optical spectra it has been found that C^{2+}, N^{2+}, O^{+}, and Ne^{2+} also exhibit discrepancies between abundances obtained from CELs and ORLs (e.g. [20], [21], [39]). Note that many of these ADF studies have involved observations at both UV and optical wavelengths, which complicates the analysis as one has to calibrate the relative intensities in two different spectrometers. It would be very useful to have an ORL and CEL in the same wavelength window.

A number of effects have been invoked to try and explain these discrepancies. The relevant effects can be split into three main areas of consideration: uncertainties in the observations, uncertainties in the atomic data, or hidden atomic and physical processes in the plasmas. Observational uncertainties were investigated but were only partially able to explain the ADFs [42]. Inaccuracies in the atomic data were explored, but similarly did not explain the ADFs. In recent years, the dielectronic recombination rate coefficients have been of a particular interest. For example, Fogle et al. found that a single near threshold resonance in O^{4+} increases the recombination rate coefficient at typical photoionized plasma temperatures [43]. Also, the work of Davey and Fang et al. [28] [44] showed that careful consideration and inclusion of low energy doubly excited states could significantly change the low temperature DR rate coefficients that populate the ORLs, but no work has been done to study their effect on plasma cooling. In general, studies on the atomic data have been unable to explain the discrepancies.

Physical processes that have been studied include temperature fluctuations ([45]); density fluctuations [46]; cold, metal-rich knots [47]; non-Maxwellian (κ) electron velocity distributions [48]; and X-ray irradiated clumps [49]. None of these solutions have been conclusively ruled out, although non-thermal electron distributions appear to be physically implausible [50]. Inhomogeneities in astrophysical plasmas is another possible solution to the observed discrepancies. As a result of inhomogeneity (of any sort), parts of the plasma with different conditions might experience different cooling patterns, which would lead to temperature fluctuations in the plasma. The idea of temperature fluctuations within the plasma was proposed by Peimbert et al [45]. The model proposed by Peimbert et al. posits that ORLs are preferentially emitted from a lower temperature zone than where CELs are emitted, and this explanation is supported by temperature estimates from permitted line diagnostics. Because of the temperature sensitivity of CELs, they are preferentially emitted in higher temperature regions of photoionized nebulae. In contrast, ORLs are strongest in cooler parts of the gas. The temperature fluctuations scenario would imply that the real abundances are the ones derived from ORLs because they are not affected by this temperature bias, while CELs are strongly affected. On the other hand, a different scenario was proposed by Liu et al. [47], where they argue that the presence of cold, dense, H-poor inclusions, representing a small percentage of the total mass of gas in the nebula, can explain the observed ADFs. The scenario proposed by Liu et al. posits that ORLs are preferentially emitted from a lower temperature zone than CELs, supported by temperature estimates from permitted line diagnostics. The observed spectrum is then a superposition of the emission from both hot and cold regions. In this case, the "real" abundances of the nebula would be closer to the ones derived from CELs.

4.3 RER and the AD problem

It has become clear to the community that the observed nebulae seldom have homogeneous physical conditions of density, temperature and abundances, and these non-homogeneities have direct effect on the observed discrepancies. Observations of NGC 6720 [51] showed that the Optical Recombination Lines O II and Collisionally Excited Line [O III] emissions are not co-spatial, and that the O II emission is generally more centrally peaked. Moreover, the Optical Recombination Lines vs Collisionally Excited Lines abundance discrepancy was observed throughout the nebula for both O and C but was larger towards the center. This implies that the gas is chemically inhomogeneous, and the two lines are emitted from a different spatial region. The RER emission lines are predicted to originate from only the lower temperature of those regions, hence will be able to uniquely trace them.

Recent studies ([52] and references therein) have shown that the Optical Recombination Lines emission maps different structures in the Planetary Nebulae than the Collisionally Excited Lines and show that the Abundance Discrepancy problem seems to persist in other photoionized plasmas. They also found that the Abundance Discrepancy problem persists in a range of low temperature photoionized plasmas with different physical conditions. Those are all indications of the validity of Liu et al. [47] model of small metal rich clumps that are embedded in the overall gas and are responsible for the Optical Recombination Lines emission. These clumps would have extreme temperature and abundance conditions (Te $\leq$ $1000K$, and an order magnitude higher column densities). Those conditions could facilitate for RER to dominate since it forms in similar conditions and dominates at low temperatures. The RER line can be used to probe the structure of the nebulae because of its unique behavior at low temperatures. Consequently, the RER lines are expected to be emitted from the same regions as the Optical Recombination Lines, in the Planetary Nebulae affected by the Abundance Discrepancy problem and can be used to trace cold structures within the gas. Moreover, the origin of these extreme conditions found in the metal rich clumps stays a

mystery, and the processes that maintain such low temperatures are unknown. The current recombination rates used in simulation models do not lead to sufficient cooling to explain the temperature variations observed from different diagnostics. RER predicts drastically enhanced recombination rates at low temperatures which is expected to create equally drastic changes in the ionization balance of photoionized plasmas in the current models and could explain how the metal-rich clumps could maintain such low temperatures.

Inhomogeneities were also reported for moderate PNe as illustrated through a paper by Piembert et al. [53]. They conducted a study on a sample of 20 PNe that suffer from moderate to high ADFs. They found that the high-density clumps scenario is unlikely to explain the observed spectra. Furthermore, they investigated the temperature fluctuation model in the studied PNe; which is characterized by the parameter t2 that describes the dispersity of temperature in the gas. They found that the observed t2 values in the range of 0.024-0128 are much higher than predicted by Cloudy (which typically has values less than 0.012). Usually the equilibrium temperature is simulated by solving the power balance equation as a function of radius, and as a result produce the respective equilibrium temperature for each region of the nebula. In this picture, the diagnostics obtained from the ORLs and CELs are correct and reflect genuinely different parts of the plasma at different equilibrium temperatures due to their respective physical conditions. This explanation has been hampered by the fact that modeling codes for photo-ionized plasmas do not predict the observed temperature variations without introducing additional heating or cooling mechanisms to get a good match. Ercolano et al. [49] had to introduce additional heating source in the power balance equation, to achieve the observed equilibrium conditions in the outer hot parts, in the form of dust grains. While Piembert et al. postulated that the observed values can be achieved in the existing models by the addition of missing energy sources, and they proposes shock waves as a heating source to some of the cases.

The above conclusions were deduced empirically from the observed spectra, but no fundamental description of the mechanism at which these conditions formed is explored. Many authors have argued historically about the existence of a hidden atomic process that could complete the description of line production mechanisms and fix the erroneous atomic data necessary to resolve the AD problem [42], [54], [55]. While it is not clear without including RER to all the ions if it would explain the observed ADFs, the description of low-temperature non-homogeneous plasmas is incomplete without and sensitive to the inclusion of RER. The test model we simulated in Cloudy do not show significant cooling when RER is included, but the cooling effect is enhanced when we introduce density fluctuations. The cooling is an indirect effect of changing the ionization balance of the plasma which causes different coolants (e.g. C^{3+}, C^{2+}) to spatially redistribute which will change the cooling pattern in the gas. Hence, plasma cooling, inhomogeneity and atomic processes (specifically RER) are codependent, and the nature of their relationship can be exposed with detailed modelling. The above demonstration of RERs effect on plasma modelling is merely qualitative and a more accurate description can be studied when including RER in all the ions.

In the future we plan to model these scenarios for specific PNe using Cloudy. To demonstrate the effect of adding the new rates of all the important ions in regard to the bi-abundance scenario described above, we simulated the test suite pn_fluc with the experimental rates of C and O charge states (until we make new rates including RER for all ions). The results can be seen in Figures 4.2, 4.3, and 4.4

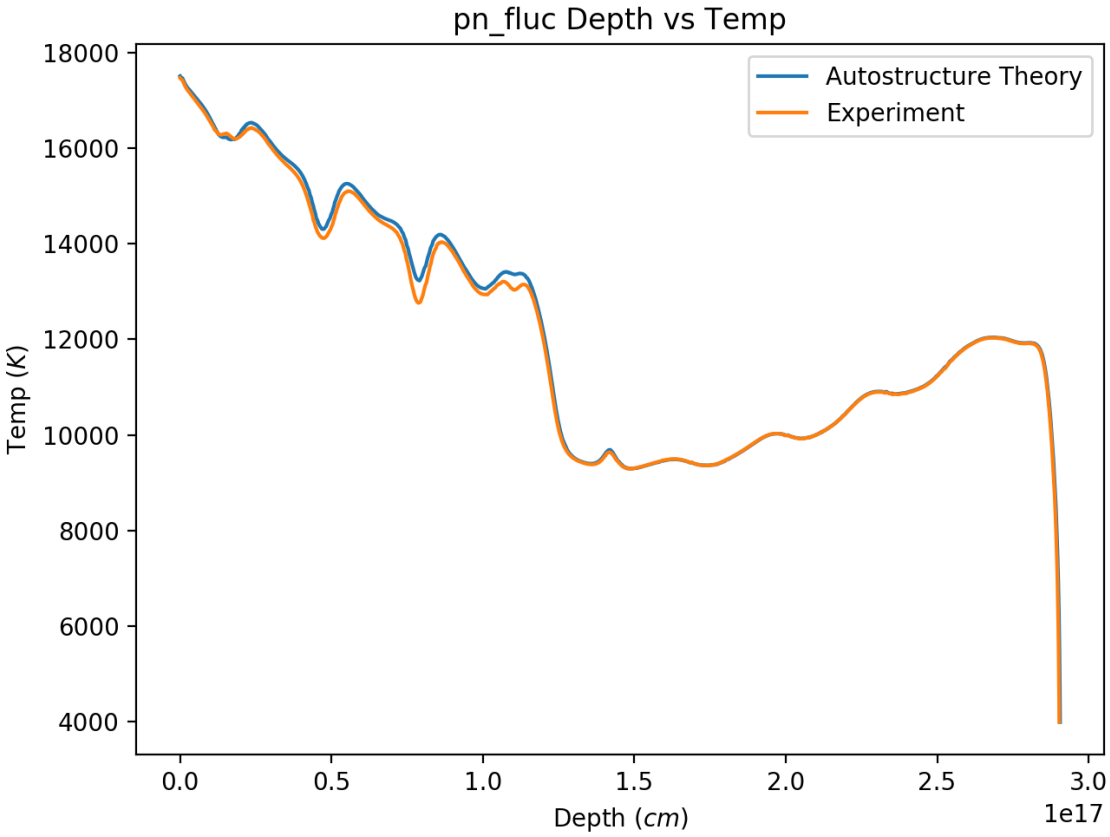

Figure 4.2: The radial temperature profile as a result of simulating a PN the has density fluctuations with the old and the new rates

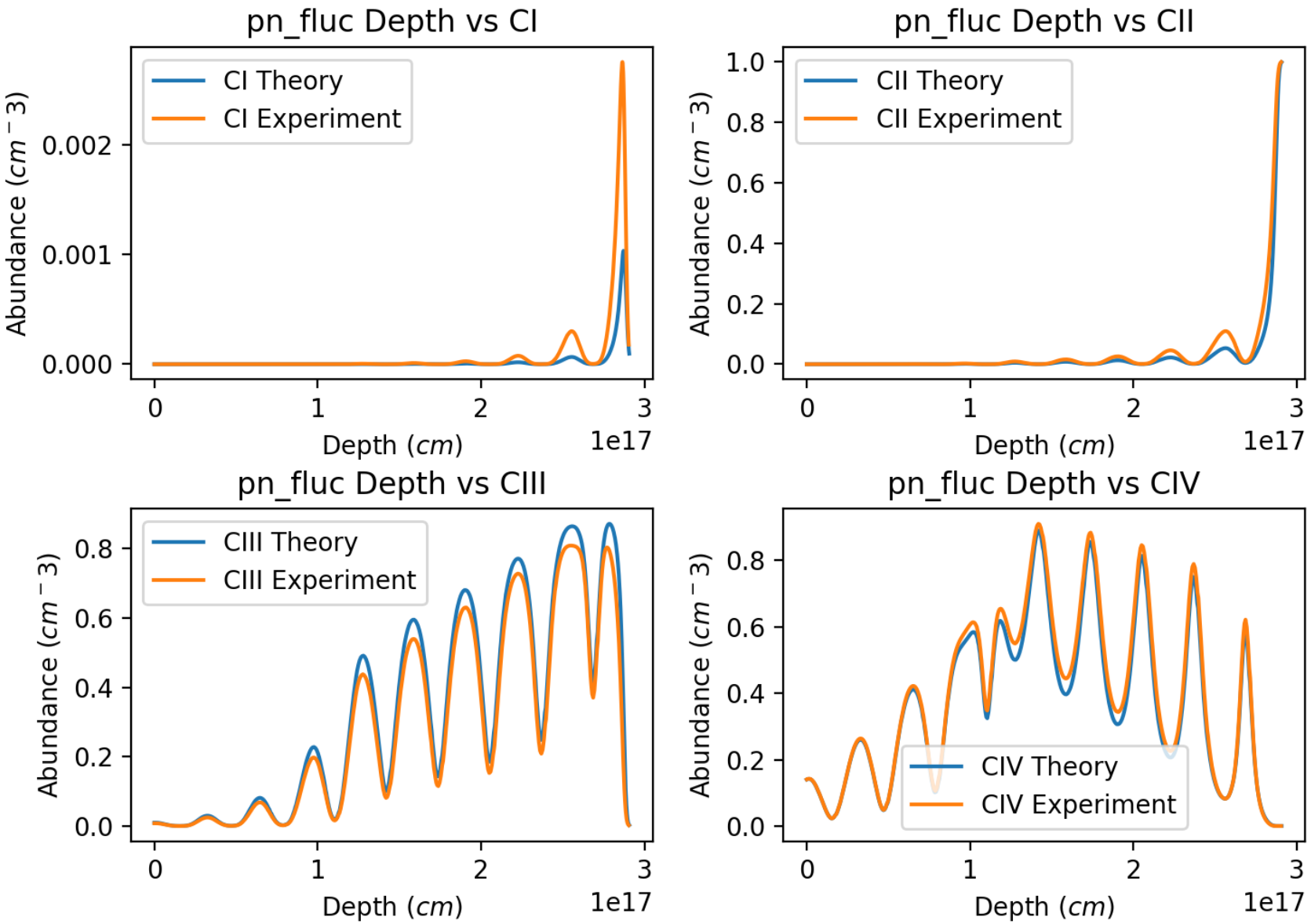

Figure 4.3: Fractional abundances of Carbon ions with the new and old rates

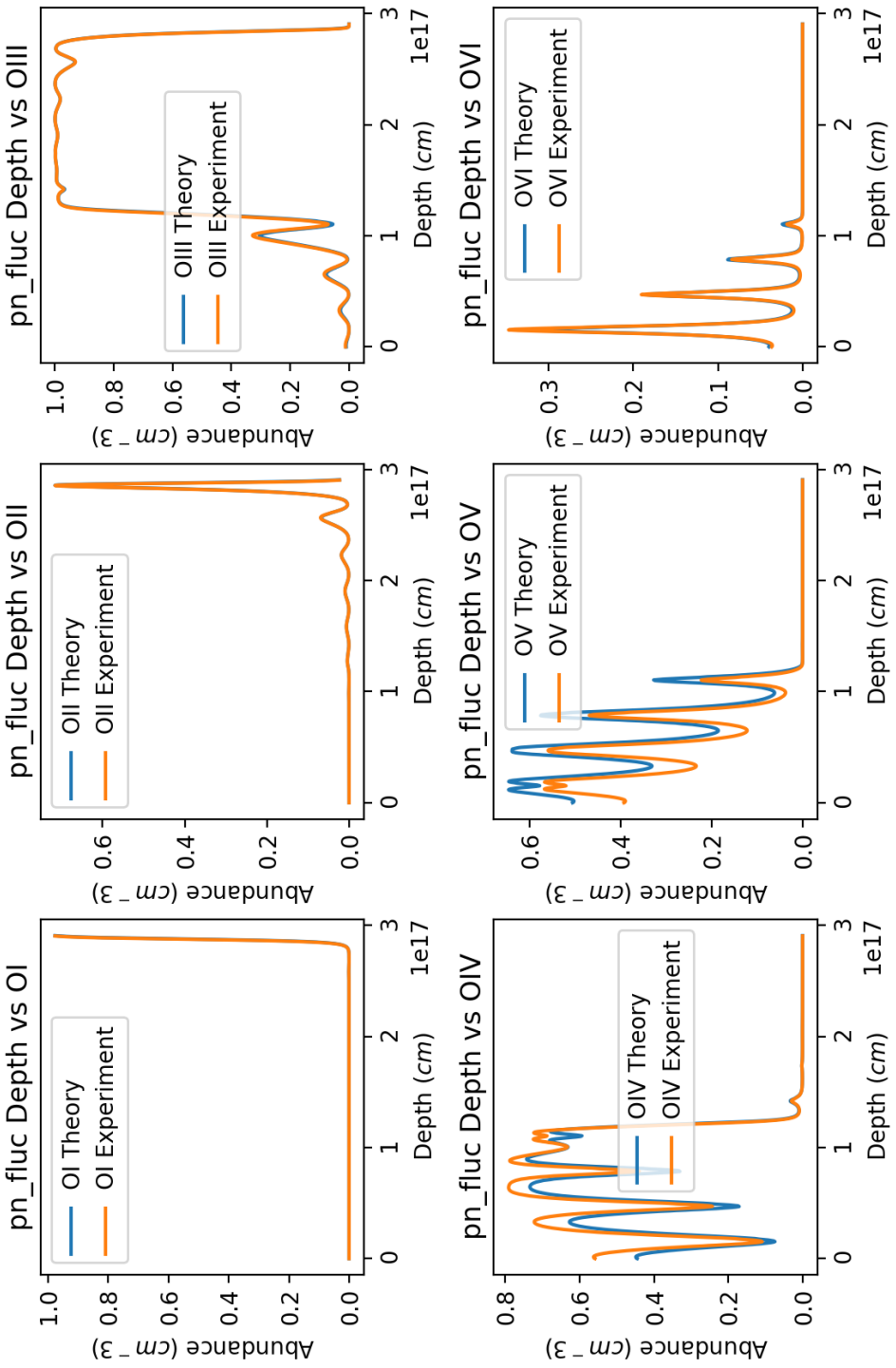

Figure 4.4: Fractional abundances of Oxygen ions with the new and old rates

The reason we used pn_fluc model as a proxy for the bi-abundance scenario is because the density changes periodically in the gas using the command fluctuations which would change the density of H (and other ions in effect) periodically between 2 values for a specified period. This picture should resemble the idea presented by Liu et al. [47] stating that the gas includes a number of metal-rich clumps in that the gas has multiple locations with different physical conditions. The clumps predicted by Liu et al., though, have higher abundances and extremely low temperatures (as opposed to pn_fluc). The interesting thing to observe from the results is that in the zone where the temperature dips (probably because of the dip in density) at around depth 0.7×10^{17} cm the new rates will cause this dip to be deeper. This is probably because the enhanced recombination increased a good coolant causing enhanced cooling. What is more interesting is that the increase in cooling is mainly due to one ion (O IV) increased fractional abundance in that region while the increase in recombination rate is about 20% at the simulated temperature. Moreover, for the zones further than 17×10^{17} cm the cooling mainly comes from O III, but there are no differences between experimental and theory for this ion. O III and O IV are some of the cases that we found measured below threshold resonances on NIST making them a strong candidate to be affected by RER. If we want to test the bi-abundance model thoroughly, we would create more extreme conditions in the gas where temperatures in would go down to $\sim 1000K$ and the abundances in the clumps would be enhanced rather than diminished. As can be seen from Fig 2.4, when we include RER in the rates, we saw an enhancement of orders of magnitude at temperatures below 10,000 K for C III.

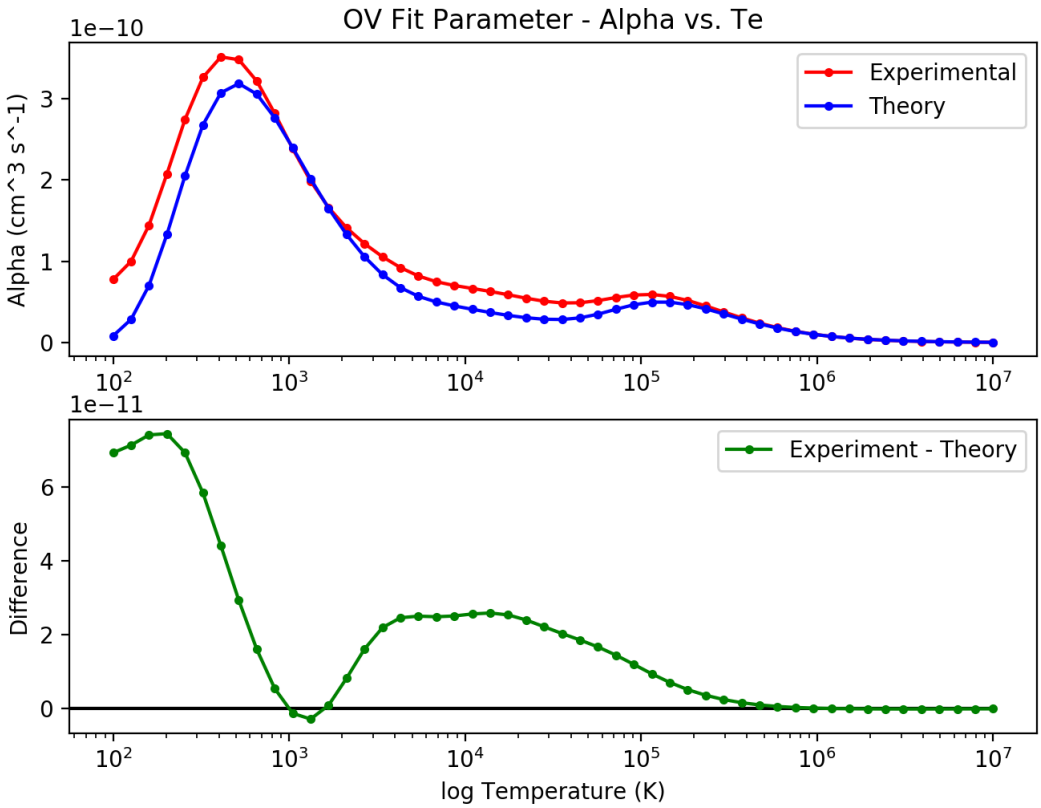

Figure 4.5: Comparison between experimental and theoretical rates of O V as a function of temperature

4.4 Implications of RER for spectroscopy

The near-threshold doubly-excited states populated by RER produce emission lines across the spectrum, with the strongest transitions typically in the UV. Table 3.1 shows a list of lines that are a direct indication of RER from different ion species (i.e. CII, CIII, OII, OIII). We could not search for the majority of these lines in our study due to the lack of high-resolution, high S/N UV spectra of PNe. The branching ratios for RER lines the in the optical tend to be small, except for CII 7119.73, 7112.94, and 7115.53

Furthermore, we propose a new temperature diagnostic based on the line ratios of the strongest CII ORLs; the well-known C II 4267 and the newly predicted C II 7115.6. This ratio can be valuable for determining electron temperatures for the part of the gas that has higher Carbon abundances, and we would be able to tell if that part is hot or cold compared to other temperature diagnostics (i.e. Hydrogen and Helium lines that describe global temperatures). In addition, the modeling of C II 7115.6 is relatively simple, requiring just energy positions, Auger rates, and radiative rates. By comparison, ORLs require a complex model which accounts for all contributions from excited states above it. There are some empirical difficulties in using such lines to measure the electron temperature. First, the variation in the line ratio with temperature is weak, typically a factor of 1.5 to 5.5 when the temperature changes from 3,500 to 20,000 K, which means that very accurate relative flux calibration over the wavelength range spanning the two C II lines is required. As described above, PNe are complicated objects that come in a wide range of physical conditions and might experience inhomogeneity in different part of the nebula. The combined spectrum from these different parts will reflect the conditions of both (or more). Fig. 4.6 show the expected line ratio of the CII 4267 and 7115.6A lines as a function of temperature. The obtained ratios were higher than 20 and up to ~ 220. A ratio of 1-5 would have reflected a pure line ratio from the same part of the gas, and we would be able to tell the temperature of that part. Nevertheless, the present predictions don't adequately account for the observed ratios, so

a more complex scenario may be at play. It is likely that detailed modeling (perhaps with Cloudy) will be needed to unravel the current situation for the seven PNe we investigated. Alternatively, observations from distinct zones that can separate the spectrum would serve to address this issue.

The change in the ionization state of the gas will change the column densities of related ions, and this outcome will extend to affect individual line emission. The intensities of carbon recombination lines that are used for diagnostics will diminish or increase depending on the change of the respective ions column density. In the test simulation we made through Cloudy of a PN, we noticed a change of 15% in recombination line intensities of CII, CIII, CIV. The CII 4267A line decreased by 15%, while there was an increase by a similar amount to CIII 4069A and CIII 4649A. There was also a decrease of 65% in CIV 1549A, and this line is of specific interest because it is very close to the CIV 1550A resonance line in energy and may be a source of blending. On the other hand, accurate account of RER when calculating individual line emissivities is necessary to match the observed line heights. We predict that including RER will change the effective recombination coefficients of some RLs as well as changing level populations of all excited levels in an ion when conducting a collisional-radiative model.

4.5 Implications of RER for radio astronomy

Moreover, DR is a major atomic process to populate/depopulate the high Rydberg states of the ion that lie just below the ionization threshold. Pedlar et al. [56] have inspected the 109α line of C I at 5011 MHz (109 indicates transitions to n=109 and α represents transitions with $\Delta n = 1$) in the radio frequency regime to explain its inconsistent observed intensity as compared to common models. The carbon line intensity was observed to be 3% that of the 109α H I recombination line at 5 GHz, while the expected carbon abundance is about 1×10^{-4} of the hydrogen abundance. The authors report that this irregular behavior can be accounted for if DR is correctly included in the model as it serves to overpopulate specific

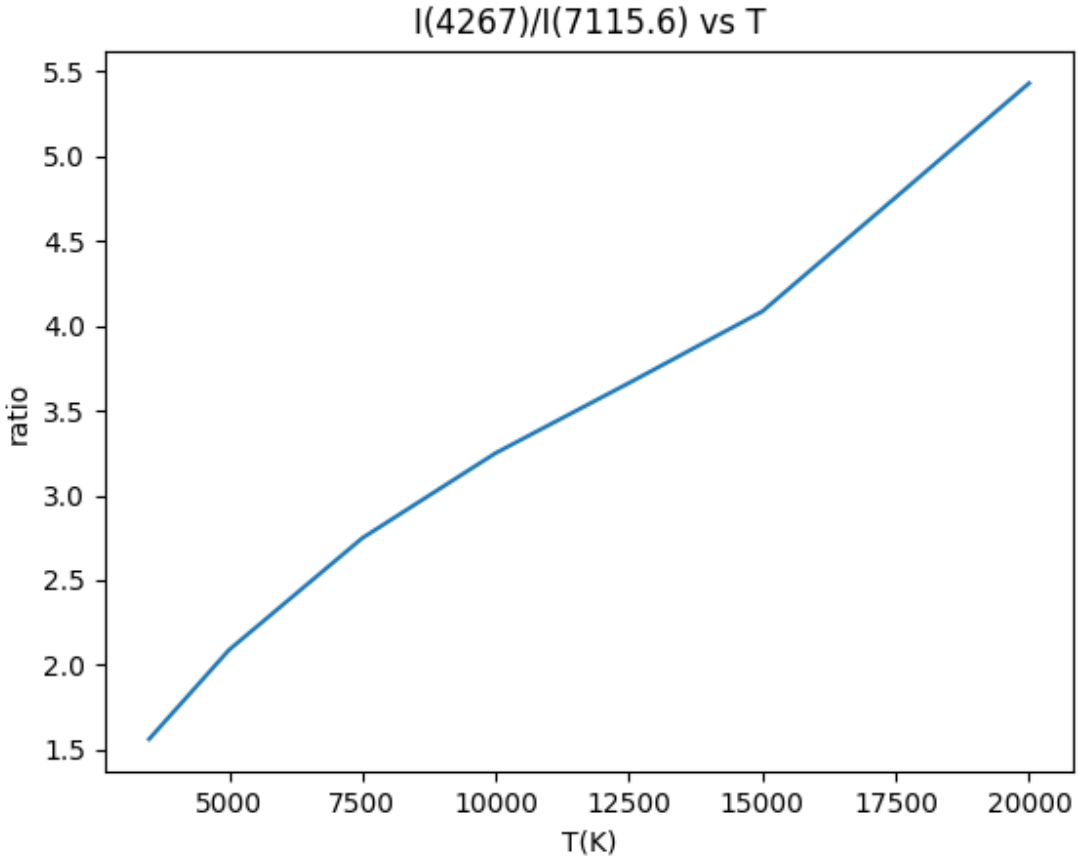

Figure 4.6: Figure 7: The ratio of predicted intensities of C II 4267 and C II 7115.6 as a function of temperature

high Rydberg states, and hence intensify lines coming from these states. This observation by Pedlar et al. along with the observed widths of Carbon Radio Recombination Lines (RRLs) as compared to neighboring HI and He II lines led to the conclusion that these lines are emitted from different part of the gas at much lower temperature.

We discussed in chapter 2 the effect of adding an enhanced rate for a few resonances affected by RER to Rydberg populations where is creates a dip in the departure factor for n-shells around those Rydberg states. We also saw that the dip is collisionally distributed to the neighboring Rydberg states. Fig 2.2 shows that the width and depth of this shape is density dependent. Moreover, the relationship between temperature and departure factors is more complicated. For low temperatures the high-n shells still tend to 1 as expected, and the lower n-shells become closer to unity as a result of increasing temperature (hence more collisions); but the populations are not very sensitive to temperature change at this regime. On the other hand, at temperatures above 12,000 K we see an unusual behaviour. For lower n-shells (below n=100) we start seeing an increasing overpopulation with a deviation factor above unity. The overpopulation behaviour peaks at about n=100 and then decays to unity as n goes to infinity (but saturates very slowly). It also seems that for higher temperatures, the overpopulation peaks at a higher n-shell. This effect was predicted and proved by Pedlar et al. as described earlier in the section. They refer this higher intensity to an overpopulation in a range of n-shells as a result of DR to high doubly excited states as in the transition for C^+:

$$1s^2 2s^2 + e^- \rightarrow 1s^2 2s 2pnl \rightarrow 1s^2 s^2 nl \tag{4.1}$$

And this DR transition will serve to overpopulate specific nl's. For low temperatures, DR will only be able to access low lying resonances above the threshold, which will correspond to low nl's that the overpopulation is dissipated due to radiatve transitions. As the temperature increases, DR will sample more resonances, and at higher nl's which will

distribute the overpopulation over all the Rydberg states. Moreover, with the increase in the temperature the DR will have higher rates where the Maxwellian distribution of electron peaks. And this peak moves with temperature. Both of these effects can be seen in figure 4.7. Also the dip in the populations due to adding RER is not sensitive to temperature change.

All the above calculations of the departure factor were calculated without a radiation field, similar to the equations described in the introduction. We made another calculation, this time turning on the radiation field to see the effect Fig. 4.8. We still observe overpopulation in the n-shells lower than n=100, but it is damped down drastically (from maximum of b_n = 20,000 without a field to maximum of b_n = 40 for the same physical conditions). In addition, the dip in the populations due to RER almost disappears with some effect at very high temperatures. Also, the peak of the overpopulation in this case is centered at the same n-shell for all temperatures. The curves in this case saturates to unity at lower n-shell than without the field. The radiation field increases the ionization rates by adding photo-ionization to electron impact ionization like in the case without the field. The radiation field serves to arrest the increase of b_n at some value of n, and that is fixed by electron density, and thereafter to cause it to decrease to unity at the limit when $n \to \infty$. Also the disappearance of the dip in the populations is an indication that the radiation field-induced processes can be more efficient in coupling Rydberg states than collisions for many of the conditions present in photoionized plasmas.

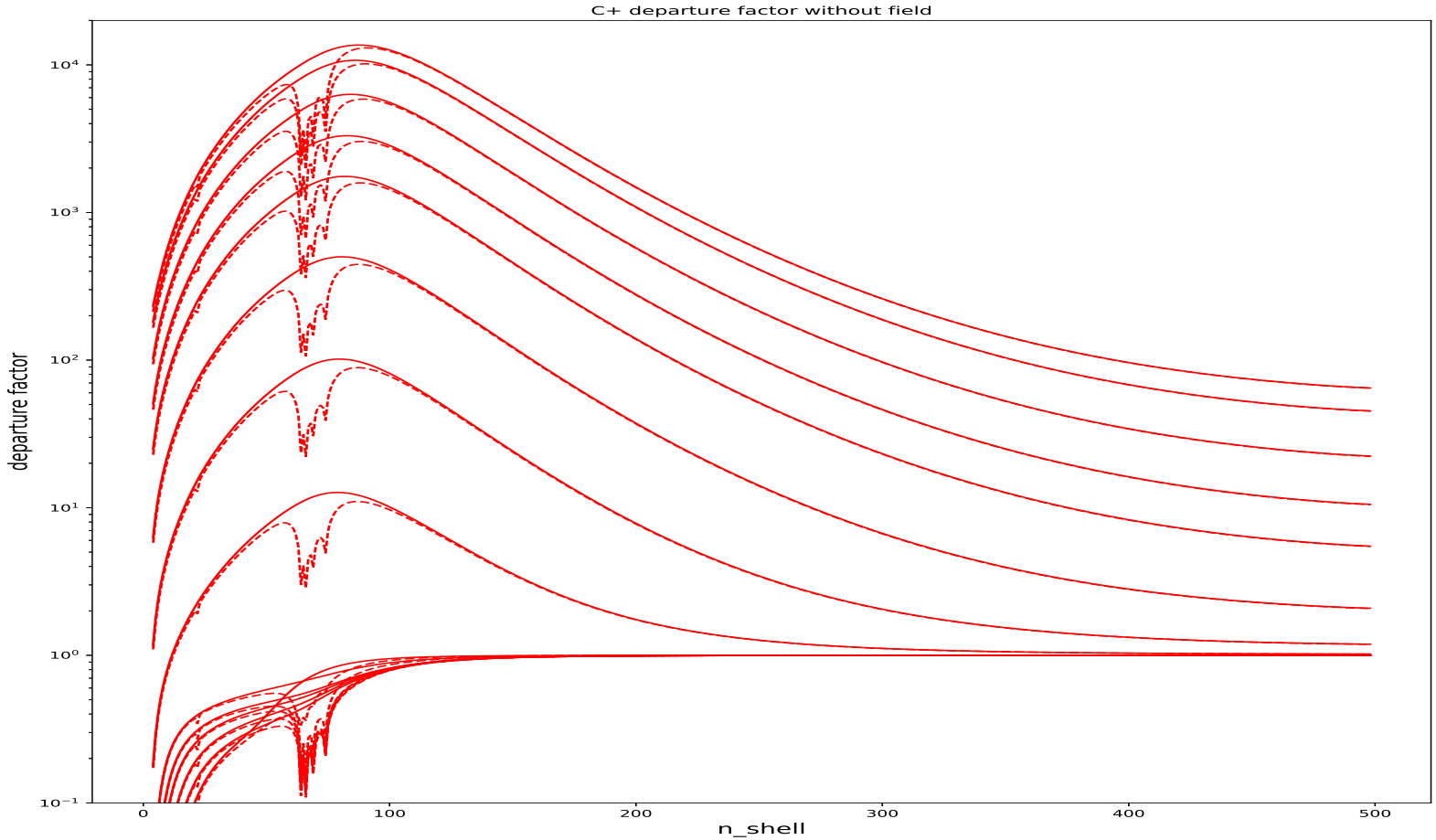

Figure 4.7: The departure factor of Rydberg state's population at different temperatures for the same density of $1 \times 10^4 cm^{-3}$. The dotted curves are with the inclusion of RER

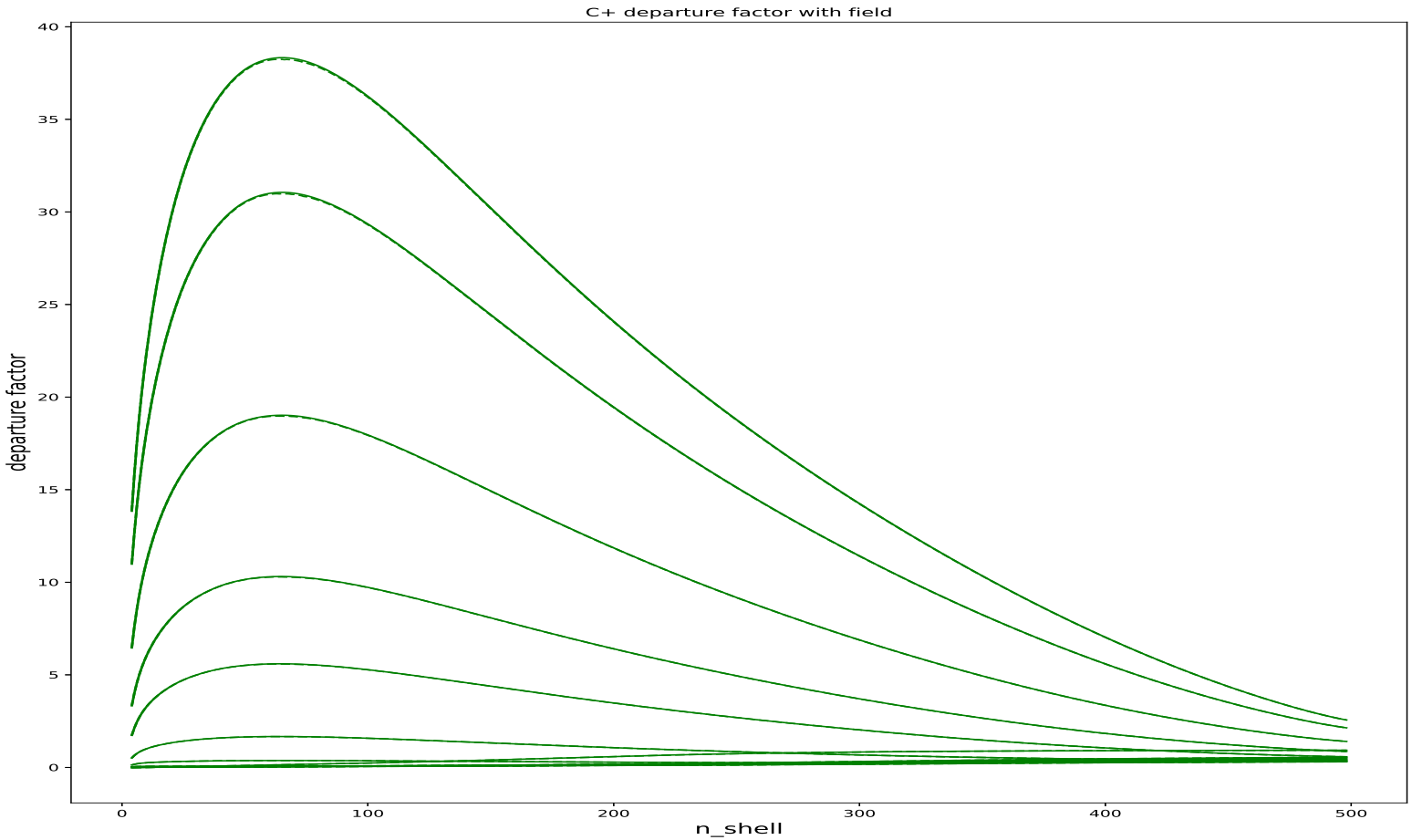

Figure 4.8: The departure factor of Rydberg state's population at different temperatures for the same density of $1 \times 10^4 cm^{-3}$ with turning on the radiation field. The dotted curves are with the inclusion of RER

The non-LTE depopulation effect due to RER in a few Rydberg states could cause a steep gradient in the Rydberg states' populations as seen in the dip in Fig 2.2. Goldberg et al. [57] pointed out that this gradient in the departure factor would play a key role at radio frequencies when the emission is corrected for stimulated emission. Specifically, the emission will depend on $\frac{\mathrm{d}\ln b_n}{\mathrm{d}n}$. The radio recombination Hydrogen and molecular lines have been shown to be affected non-LTE conditions (stimulated emission) in numerous studies [58]. As mentioned before, Hydrogen and Helium comprise $\sim 99\%$ of the volume of the gas. So the very low elemental abundances of the of elements makes them difficult to detect.

Furthermore, RRLs from Hydrogen, Helium and Carbon have been detected and used to obtain information about the properties of the emitting gas as a supplement to other techniques [59]. In cases of a strong source of radio continuum emission in the proximity of ionized gas, RRLs are expected to be a non-LTE process and affected by stimulated emission if the right conditions are achieved [60]. The optimal conditions for RRL production in ionized gasses are case-dependent with unsuccessful attempts to generalize them [61] [62]. The common general conditions to achieve RRLs were constrained to low density ($\leq \ 10^4 cm^{-3}$), low temperature ($\leq 10,000K$), and a mechanism to throw Rydberg states, that produce RRLs, out of their LTE conditions. Goldberg et al. [57] have made the remark that the slope of level populations (for example as in Fig. 2.2) should be indicative of the nature of emission originating from it. That is, if the slope (db_n/dn) is positive within a range of n-shells (hence range of frequencies), then the excitation temperature is negative in that frequency range of lines and it will be affected by maser amplification. Accordingly, RER is expected to alter the populations of Rydberg states, and the perturbation would re-distribute amongst neighboring states through collisions; we found that RER timescales ($\sim$ ns) are much faster than collisional timescales ($\sim$ 100s). In this case, $b_n - b_n - 1$ might subtend large values in which case the lines might appear with maser amplification. This

modelling work will be explored in subsequent papers. Figure 2.2 shows the steep gradient in populations which in turn will cause maser amplifications of some of Carbon RRLs.

Chapter 5

Cloudy Simulations

In this chapter we explore the effects that RER-modified recombination rate coefficients have on photoionized plasma environments. We have calculated the new rates by modifying two atomic structure codes (AUTOSTRUCTURE and GRASP) and generated fit coefficients for the new data in the form used by the Cloudy code, as described by Badnell et al. [**?**]. The new rates that were added were for C II and C III at the moment, but we are in the process of systematically making new rates for all relevant ions. The data file in Cloudy that contains DR information is called badnell_dr.dat and can be found in the data folder. Only the data for the two carbon ions was modified in this file. In order to study the effect of RER on plasma properties, we decided to explore the parameter space by changing important plasma conditions and looking at the effects of the modified recombination rate coefficients. In collaboration with Francisco Guzman, one of the Cloudy team, it was decided to start with the simplest type of model and build up to more complex scenarios. This was to allow the parameter space to be identified under which RER can have a affect on plasma conditions.

5.1 Exploring the parameter space

The first run is a simplified model and was made for a laser source that has enough energy to ionize C^{2+} (4 Ryd or 54.4 eV) see Figures 5.1 5.2 5.3 5.4; the gas consisted of Hydrogen and Carbon only for simplicity. We only changed the ionization parameter and Hydrogen density (hence Carbon abundance) over a grid of values. The input file is described below. Some representative plots are included for each of the runs to help us make some intuitive conclusions about the new rates. I included plots for depth vs fractional

abundance of Carbon, depth vs temperature and temp vs fractional abundance. The blue curves represent the calculation with the new rates, while the red one shows the results for the unmodified rates.

```
Laser source input file:
Laser source:
laser 4 Ryd
ionization parameter -2 vary
grid -3 3 0.25 ncpus 20
init file "honly.ini"
set save prefix "newdr"
element carbon on
element carbon abundance -5 log
hden 4 log vary
grid 2 5 0.2 log
iterate
stop thickness 24 log
```

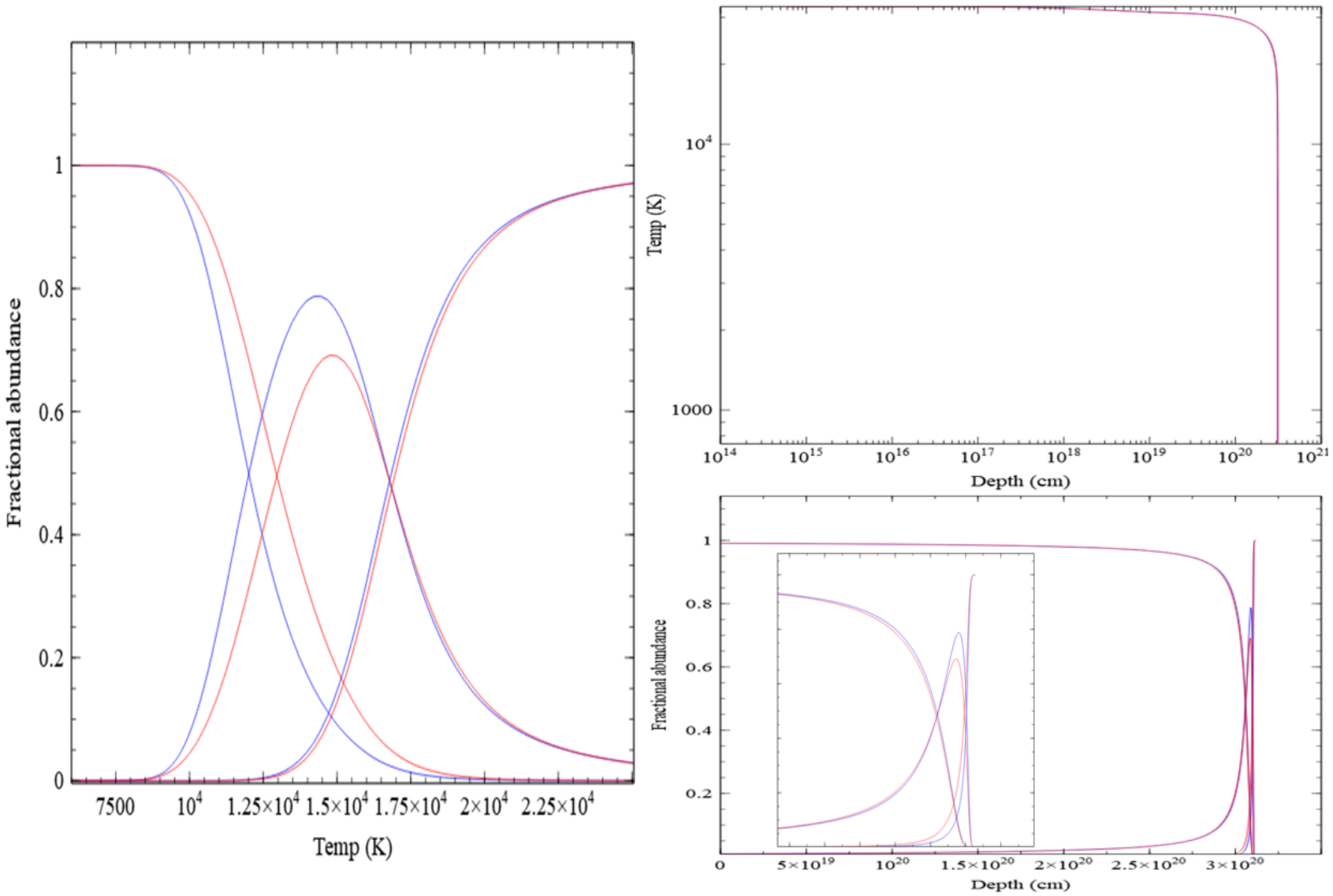

Figure 5.1: Density = 100 cm-3 , Ionization param = -1 log

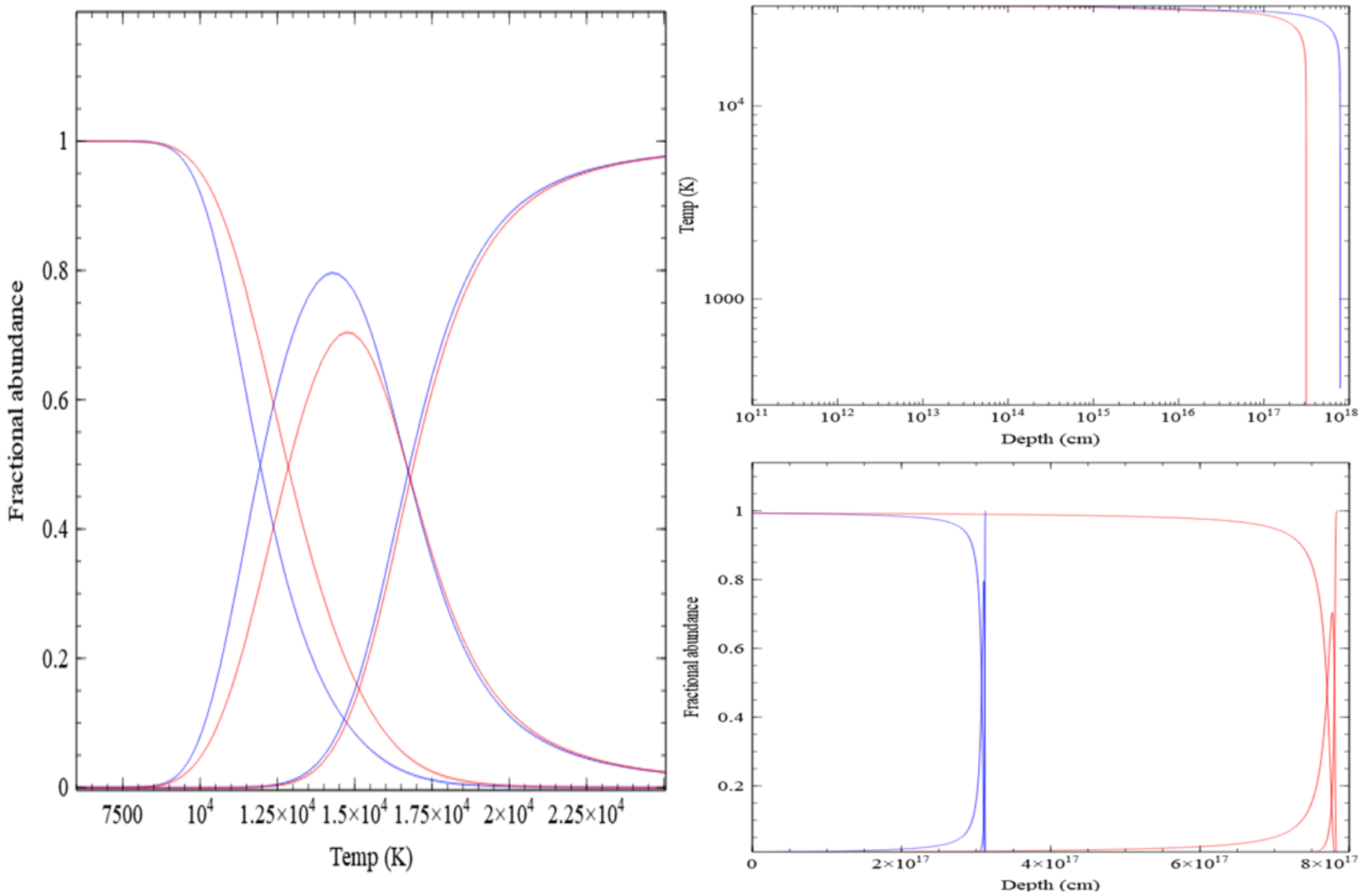

Figure 5.2: Density = 100,000 cm-3 , Ionization param = -1 log

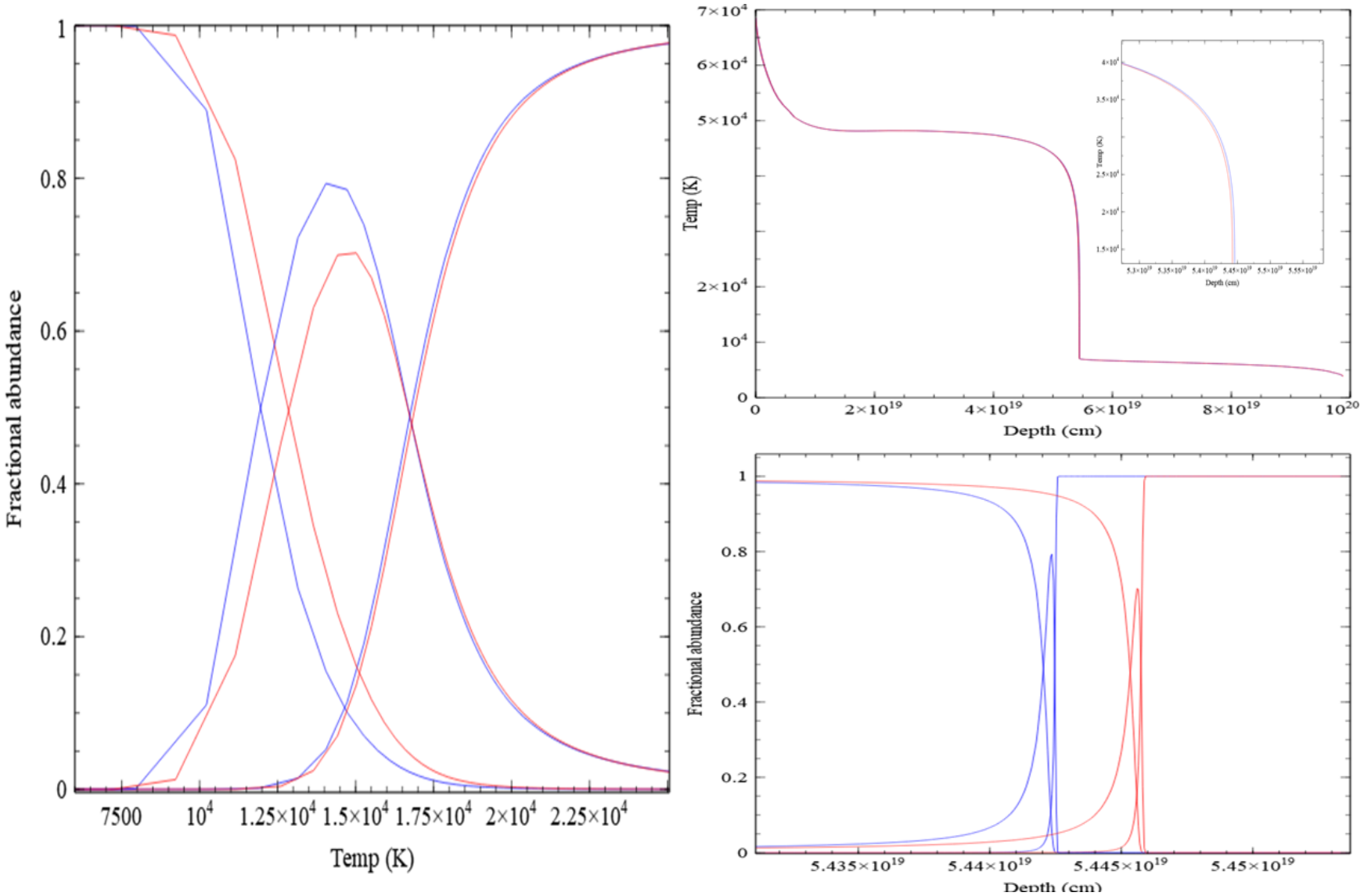

Figure 5.3: Density = 100,000 cm-3 , Ionization param = 2 log

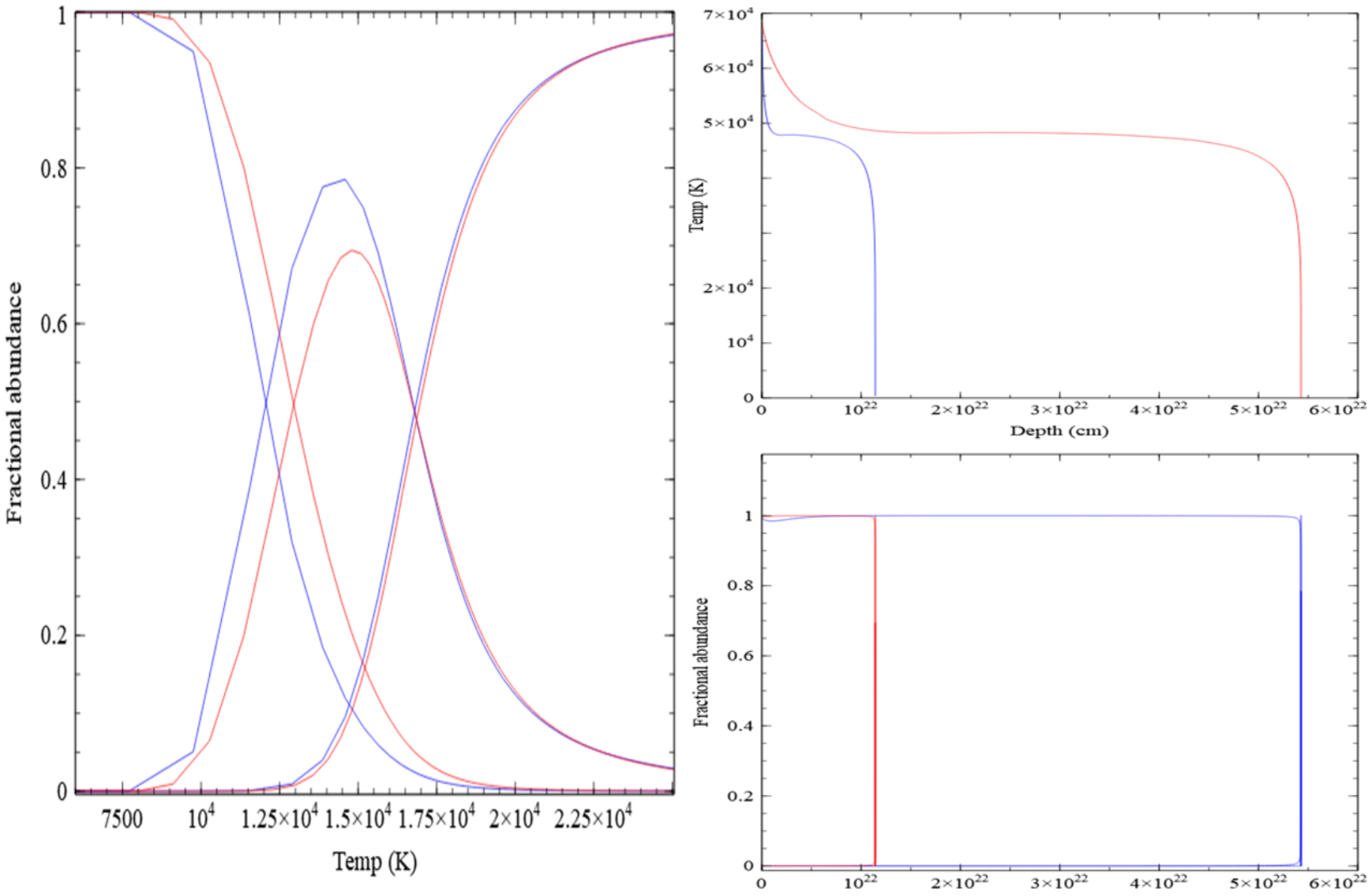

Figure 5.4: Density = 100 cm-3 , Ionization param = 2 log

Note that the recombination in the nebulae would not occur until the required temperature is reached. As a result for their not being many coolants, that temperature is reached quite slowly. Once C^{2+} is available, the temp goes down steeply. For this reason the ionization balance change occurs in a narrow spatial region. The rates clearly change the ionization balance and hence fractional abundances. The plot of temperature vs fractional abundances also changes with the rates, especially at lower temperatures. For example at lower temperatures there is an increase in recombination of C^{2+}, but that is overcome by the increased recombination of C^{+}.

There is a clear effect of changing the density and the ionization parameter on the plots. When the density is increased (i.e. increasing the amount of H and C), one observes cooling which will cause the temperature needed for recombination to be reached closer to the star. This is as expected because of the increase in amount of coolants available. The effect of the ionization parameter is observed at the front facing the star where it exhibits fast cooling due to the increase in the number of ionizing photons, and then goes back to a slow decrease further away from the star. Hence, the increase in density apparently causes the recombination to happen closer to the star, but the increase in the ionization parameter causes the recombination to happen deeper in the gas due to the increase in the heating flux.

Thus, it is apparent that the density and the ionization parameter only affect the equilibrium equations and their solution which would affect the temperature profile not the recombination process. The temperature profile is what directly controls the recombination, which will affect the cooling/heating in return. It would be optimum to have a gradually decreasing temperature in the gas; like in the case of a planetary nebula model where you have photons at different energies (which allow multiple atomic transitions and ion stages to to be accessed) and with a more complex chemical composition.

To test the effect of a more complex system we introduced a blackbody radiation source. We also introduced a more complex chemical composition by increasing Carbon abundance to match what is observed in PNe, and for a third run we introduced Oxygen since both Carbon and Oxygen are dominant coolants in low temperature plasmas [18].

Blackbody with no Oxygen:

blackbody T=5 log vary

grid 4.6 6 0.2 log ncpus 20

ionization parameter -2 vary

grid -1 2 0.5 ncpus 20

init file "honly.ini"

element carbon on

element carbon abundance -4 log

hden 4 log vary

grid 2 5 0.2 log ncpus 20

iterate

stop thickness 21 log

Blackbody with Oxygen:

blackbody T=5 log vary

grid 4.6 6 0.2 log ncpus 20

ionization parameter -2 vary

grid -1 2 0.5 ncpus 20

init file "honly.ini"

element carbon on// element oxygen on// element carbon abundance -4 log// element oxygen abundance -4 log// hden 4 log vary

grid 2 5 0.2 log ncpus 20

iterate

stop thickness 21 log

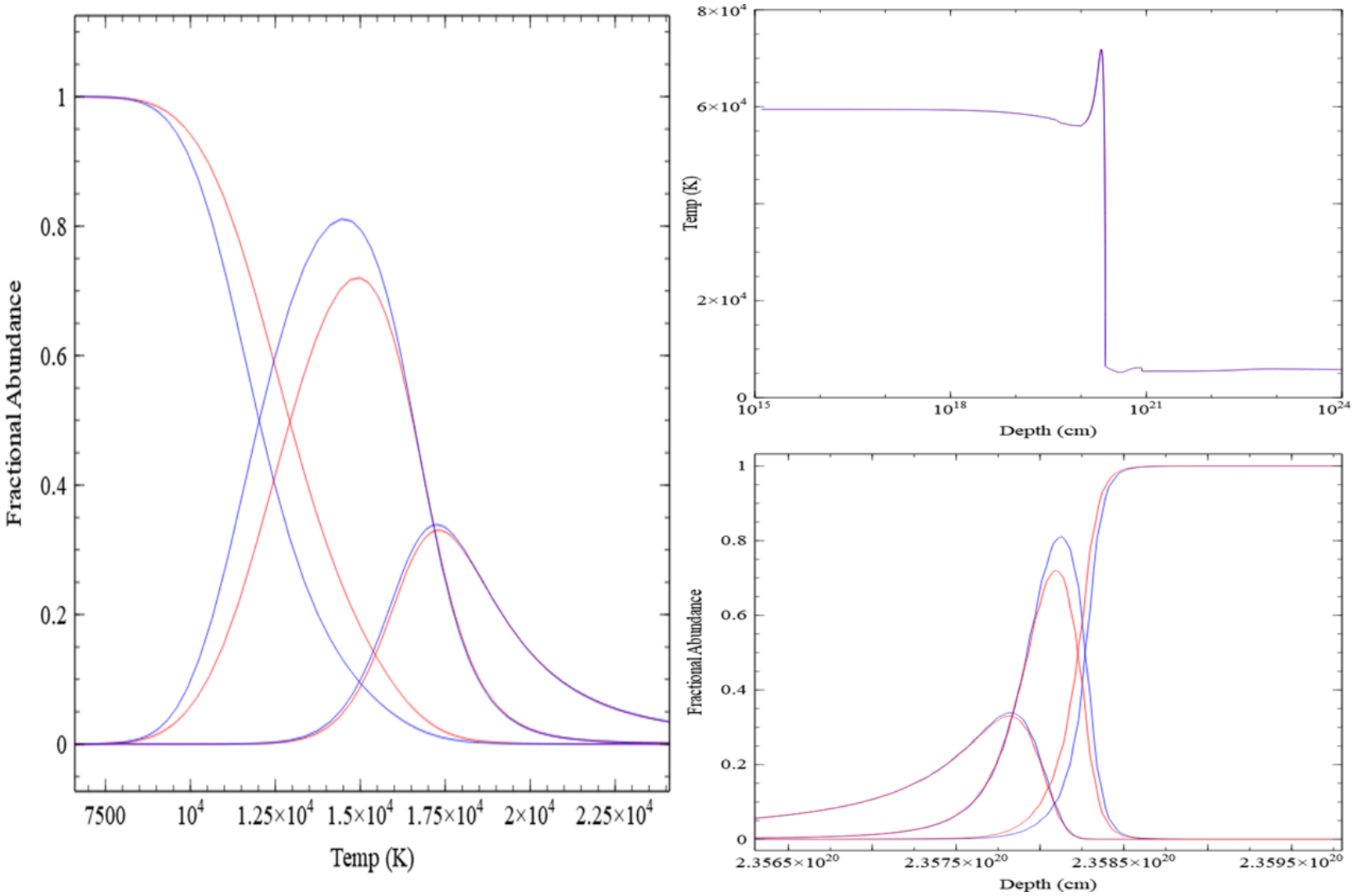

Figure 5.5: Density = 10,000 cm^{-3} , Ionization param = 2 log no O, BB_T = 100,000 K

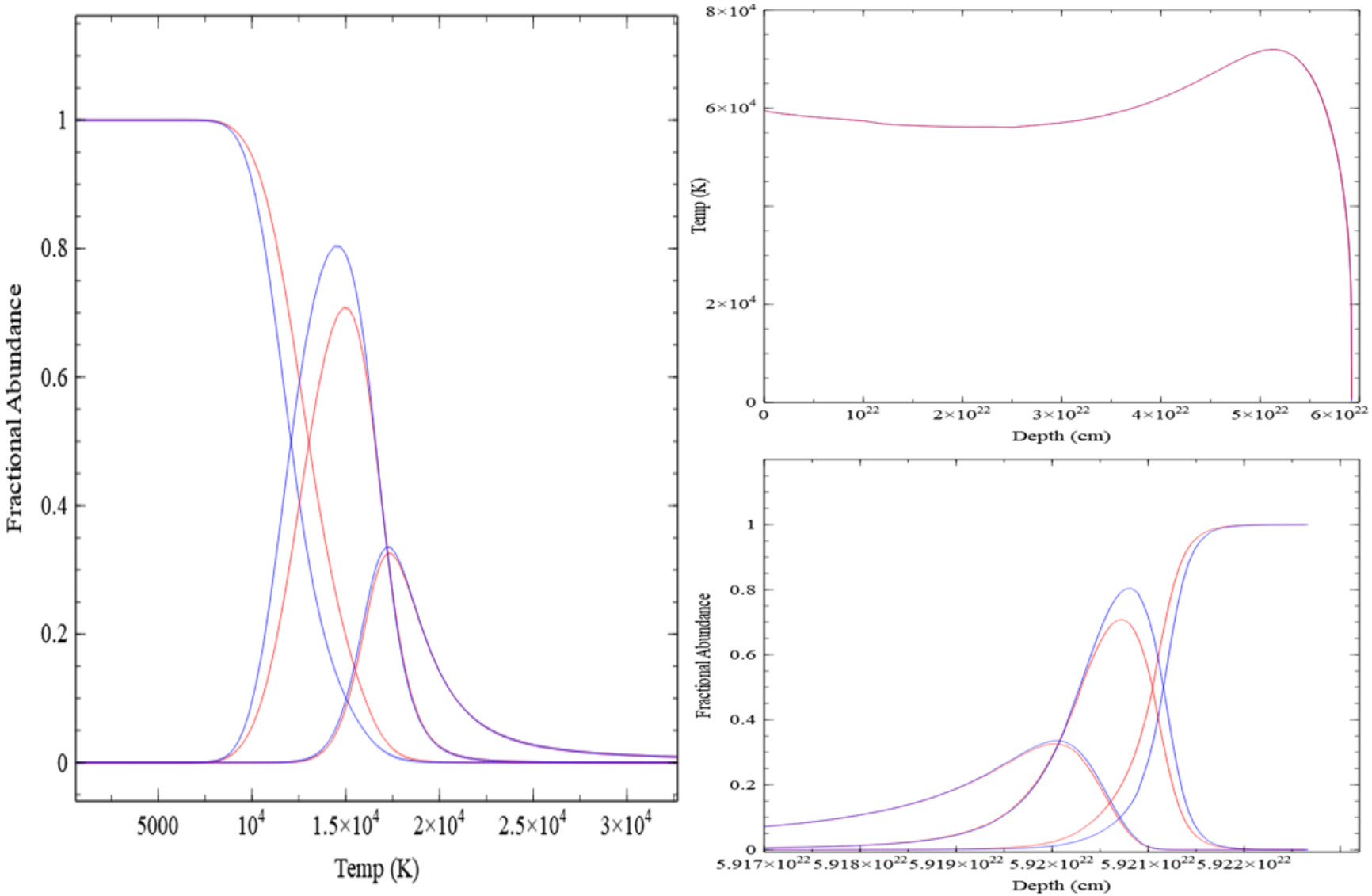

Figure 5.6: Density = 100 cm^{-3} , Ionization param = 2 log no O, BB_T = 100,000 K

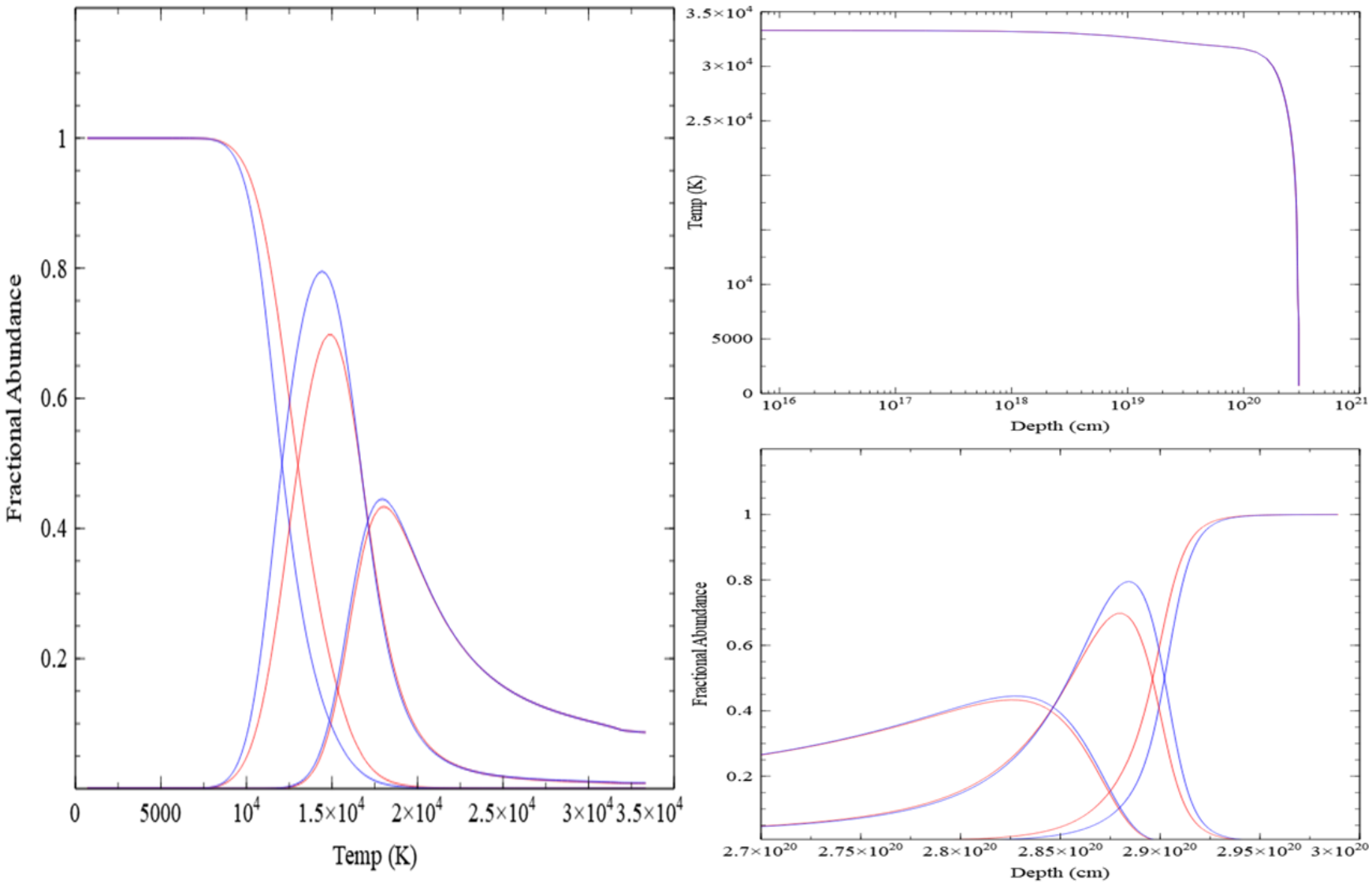

Figure 5.7: Density = 100 cm^{-3} , Ionization param = -1 log, BB_T = 100,000 K

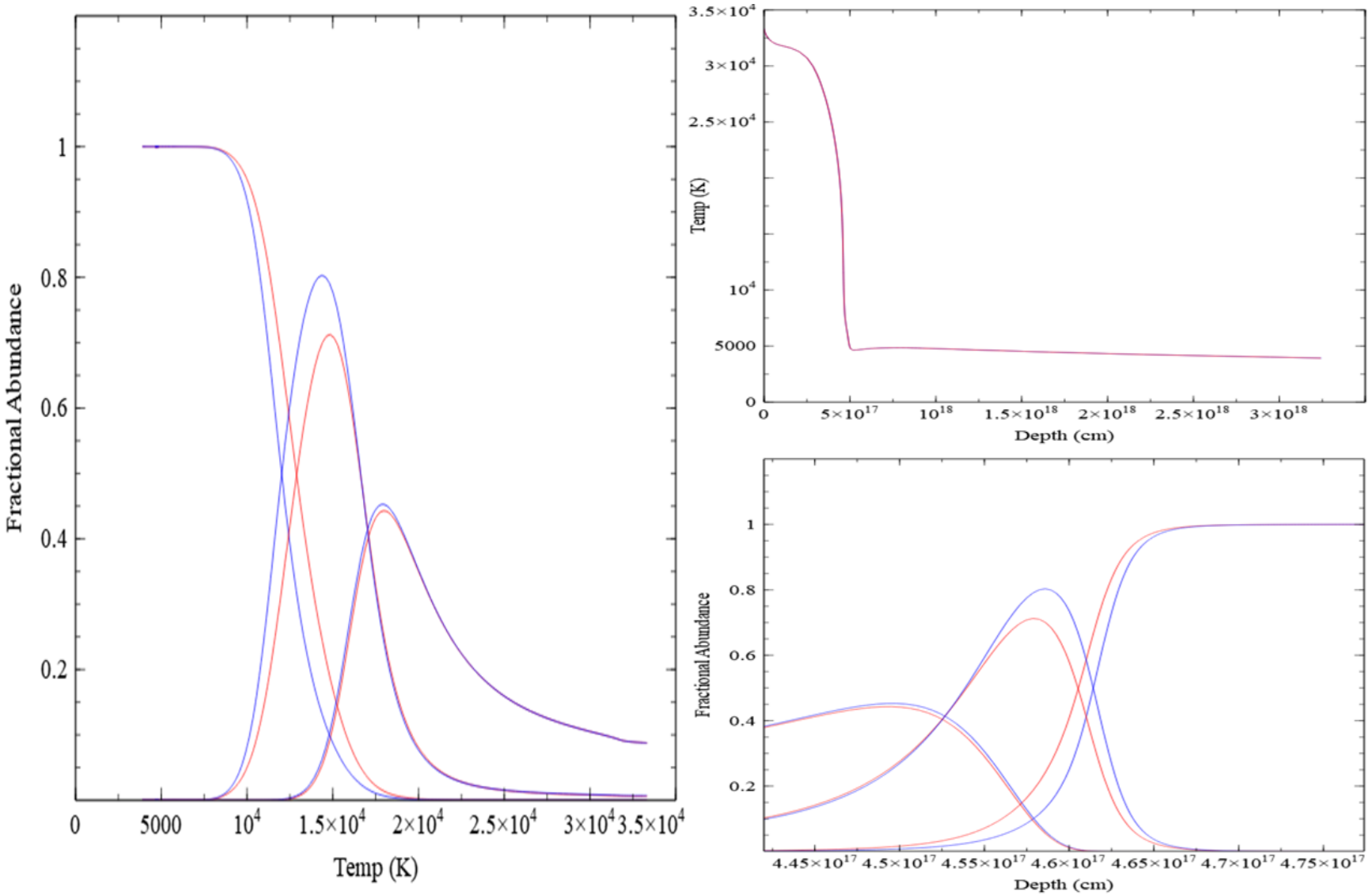

Figure 5.8: Density = 10,000 cm^{-3} , Ionization param = -1 log, BB_T = 100,000 K

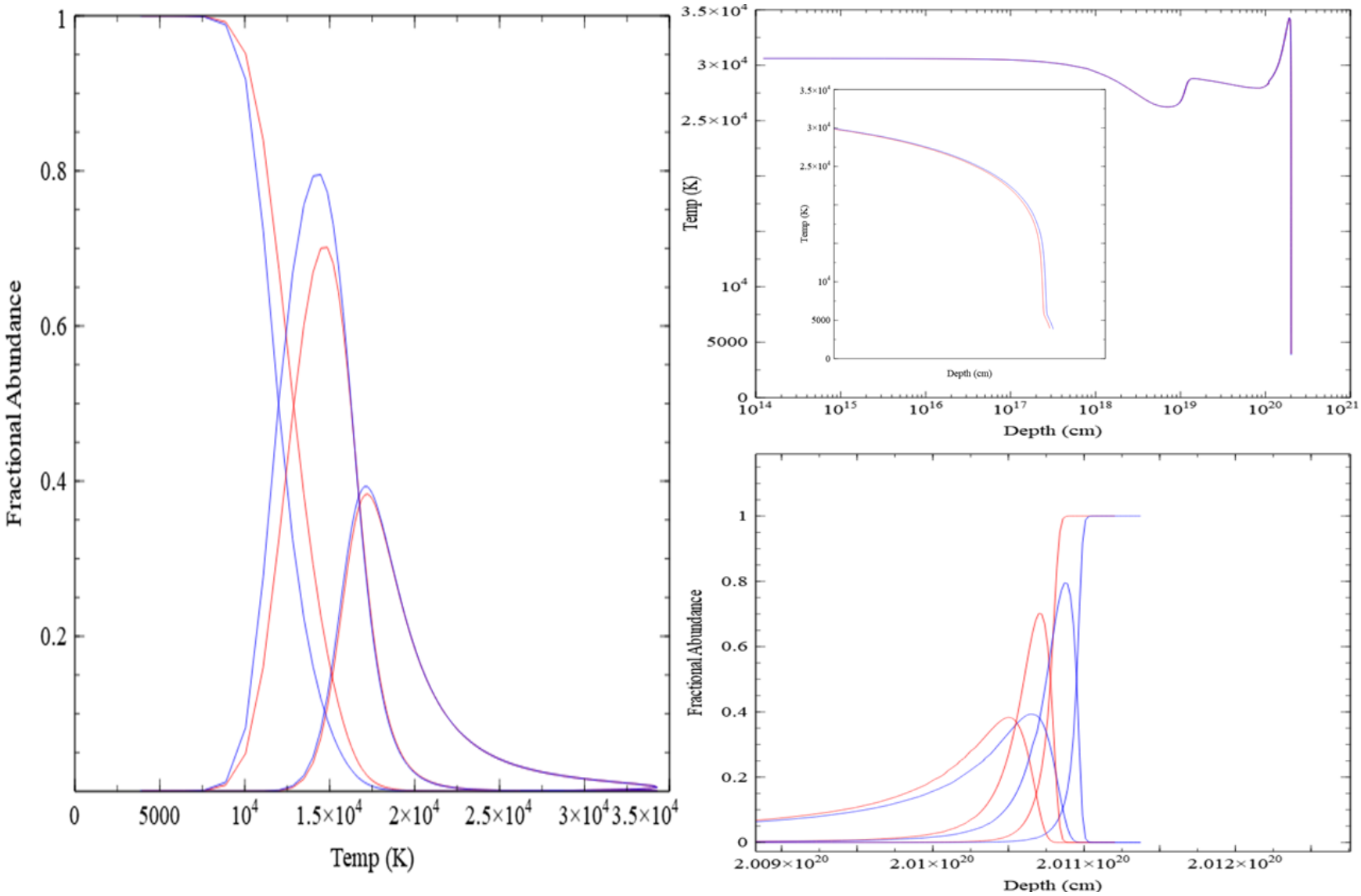

Figure 5.9: Density = 10000 cm^{-3} , Ionization param = 2 log , BB_T = 100,000 K

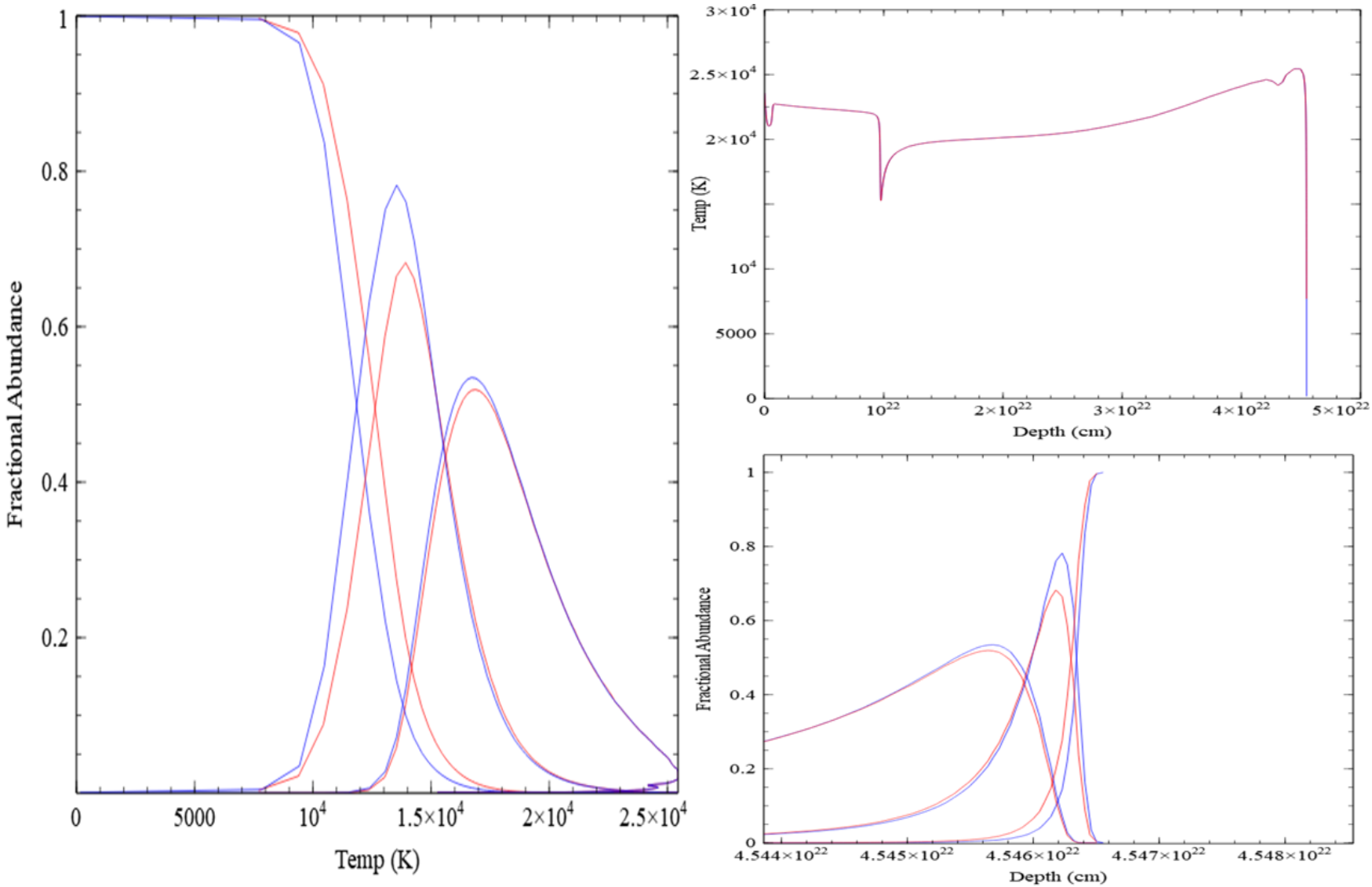

Figure 5.10: Density = 100 cm^{-3} , Ionization param = 2 log , BB_T = 100,000 K

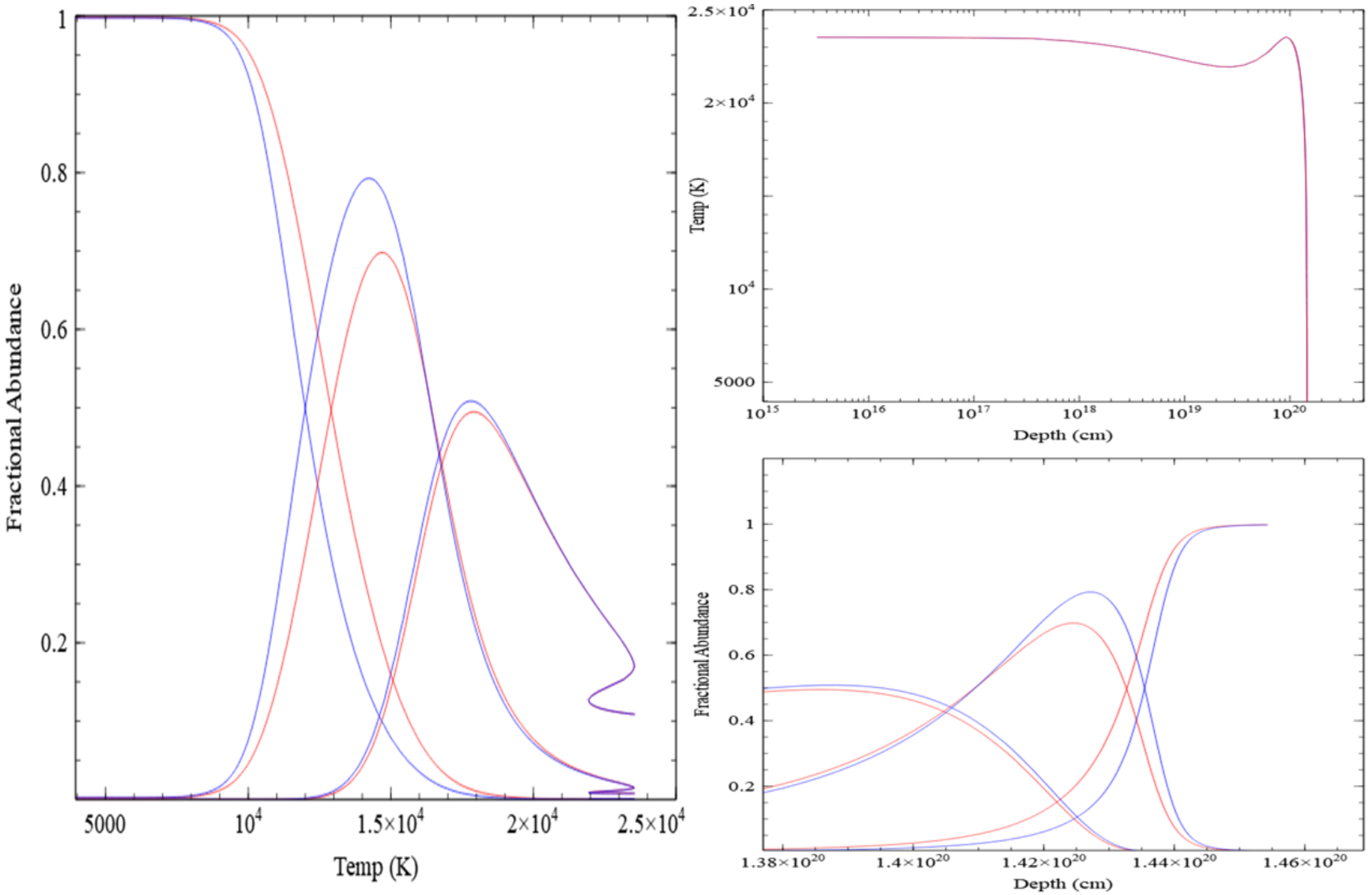

Figure 5.11: Density = 100 cm^{-3} , Ionization param = -1 log , BB_T = 100,000 K

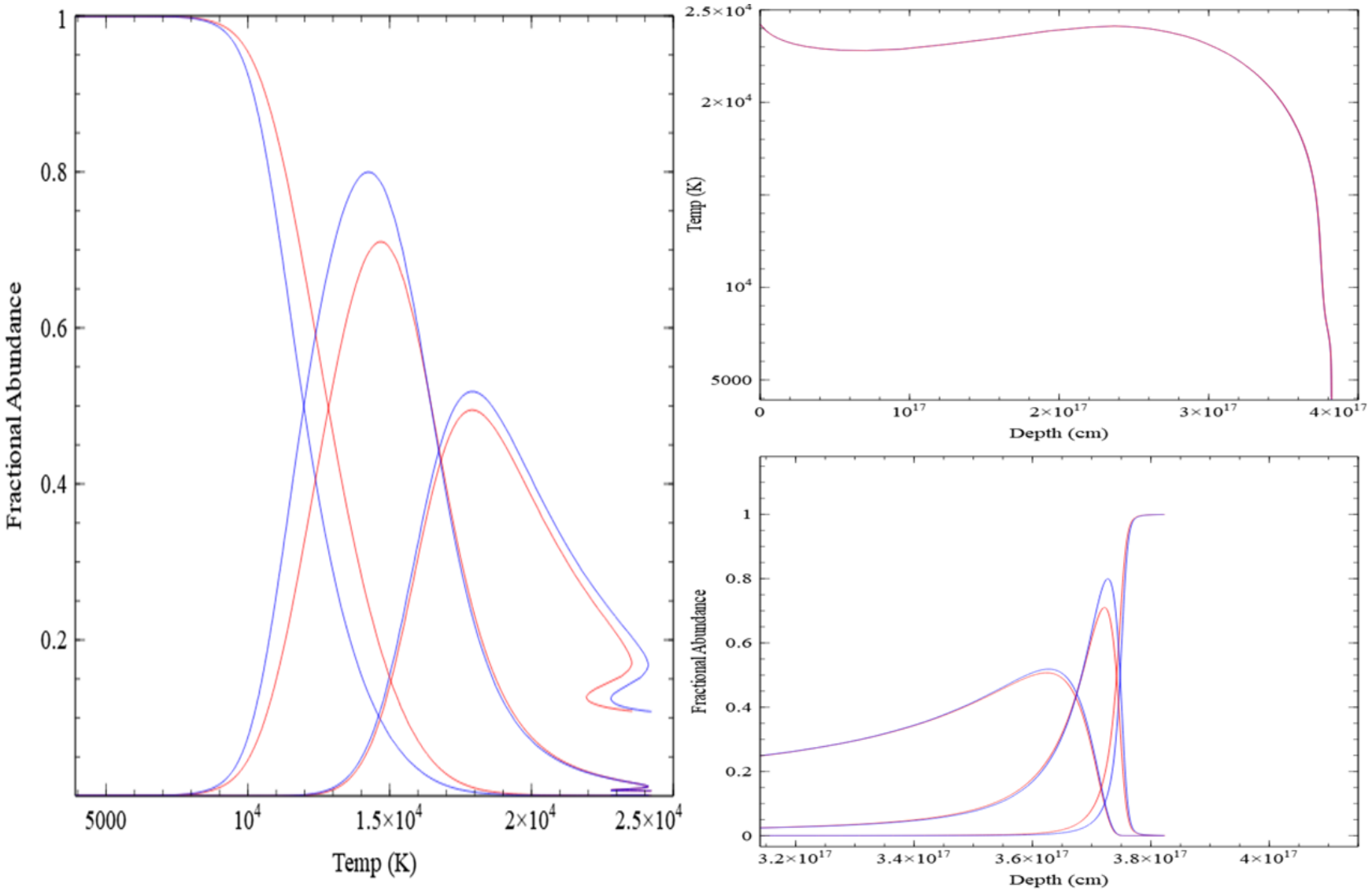

Figure 5.12: Density = 10000 cm^{-3} , Ionization param = -1 log , BB_T = 100,000 K

When we introduce the blackbody radiation source as (as in the second input file) see Figures 5.5 5.6 5.7 5.8, we reach to similar conclusion as above. The difference observed is that we have less C^{3+} and more C^{2+} earlier in the nebula because of the range of photon energies available. Then we introduce higher Carbon abundance and Oxygen to increase the amount of coolants in the gas see Figures 5.9 5.10 5.11 5.12. At that point we start to see more complicated temperature profiles (especially with high ionization parameters). This is likely the case because of the increasing number of (heating/cooling) processes in the plasma. Moreover, there is a clear cooling effect for this simulation in all the conditions. This is due to the increase in the cooling curves when adding Oxygen and the new rates which will cause the equilibrium equations to reach the required temperature closer to the star.

In summary, the new rates change the ionization balance in photoionized plasma environments. That in turn will change the spatial distribution of the different coolants in the plasma. That will cause the temperature profile to be different. The new rates take effect only at low temperatures where: a) the ion charge state is available, b) the required temperature for recombination is achieved. We do not see significant effect on cooling in these simulations because their temperatures are in the region where recombination is not too significantly enhanced. But since the enhancement in the rates increases drastically with the decrease in temperatures, we expect to see more significant effect on the cooling curves at very low temperatures. For example, if there was a location in the gas with severe conditions (low temperature, high density and abundance as in some of the proposed models to resolve the ADF discrepancy), then when the code encounters that cell it would experience increased cooling curves and very low temperatures maintained. When the code encounters the normal gas again, it would heat up again.

5.2 Tailored Cloudy models

The most complex model was considered next. In this case, a set of Cloudy inputs which had previously been used to study some of the PN was used. This model had been optimized to obtain agreement with collisionally excited lines in the PN, so was not expected to be as accurate for recombination lines. However, it provided a more complex model that could be used for line intensity studies. To characterize the C II RER lines detected, we compare the line ratio of the RER lines to a known C II ORL with observations. The most intense C II recombination line is the C II 4267 Å and is commonly detected in the observed spectra of PNe and H II regions. Figures 5.13 and 5.14 show the predicted line ratio of C II 7115 Å RER line and C II 4267 Å ORL with the inclusion of RER and without. These line ratios are calculated from the atomic data and does not consider depth dependant interactions with the gas. As can be seen from Figure 5.13 when RER is included in the recombination coefficient of C II 7115 Å RER line the ratio ranges between 1.5 - 5.5 depending on the temperature. While the ratio is orders of magnitude higher at low temperature if we did not include RER. At temperature around 7500 K the ratio drops significantly; at temperature 10,000 K the ratio is 25. The idea is that the observed ratio would tell us if RER is in play or is that conditions are not sufficient. The conditions that control occurrence of RER are the temperature, density, and the availability of the studied ions in those regions. The following table lists the observed ratio from the studied PNe.

PN	I(7115)/ I(H)	I(4267)/ I(H)	I(4267) / I(7115)
HB-12	4.48×10^{-3}	0.221	49
IC418	4.30×10^{-3}	0.5712	132.84
IC2501	9.80×10^{-3}	1	102
IC4191	3.10×10^{-3}	0.63	203
NGC2440	2.30×10^{-2}	0.48	20.9
NGC3918	6.80×10^{-3}	0.473	69
NGC7027	1.47×10^{-2}	0.575	38.3

Table 5.1: Observed intensities and line ratios

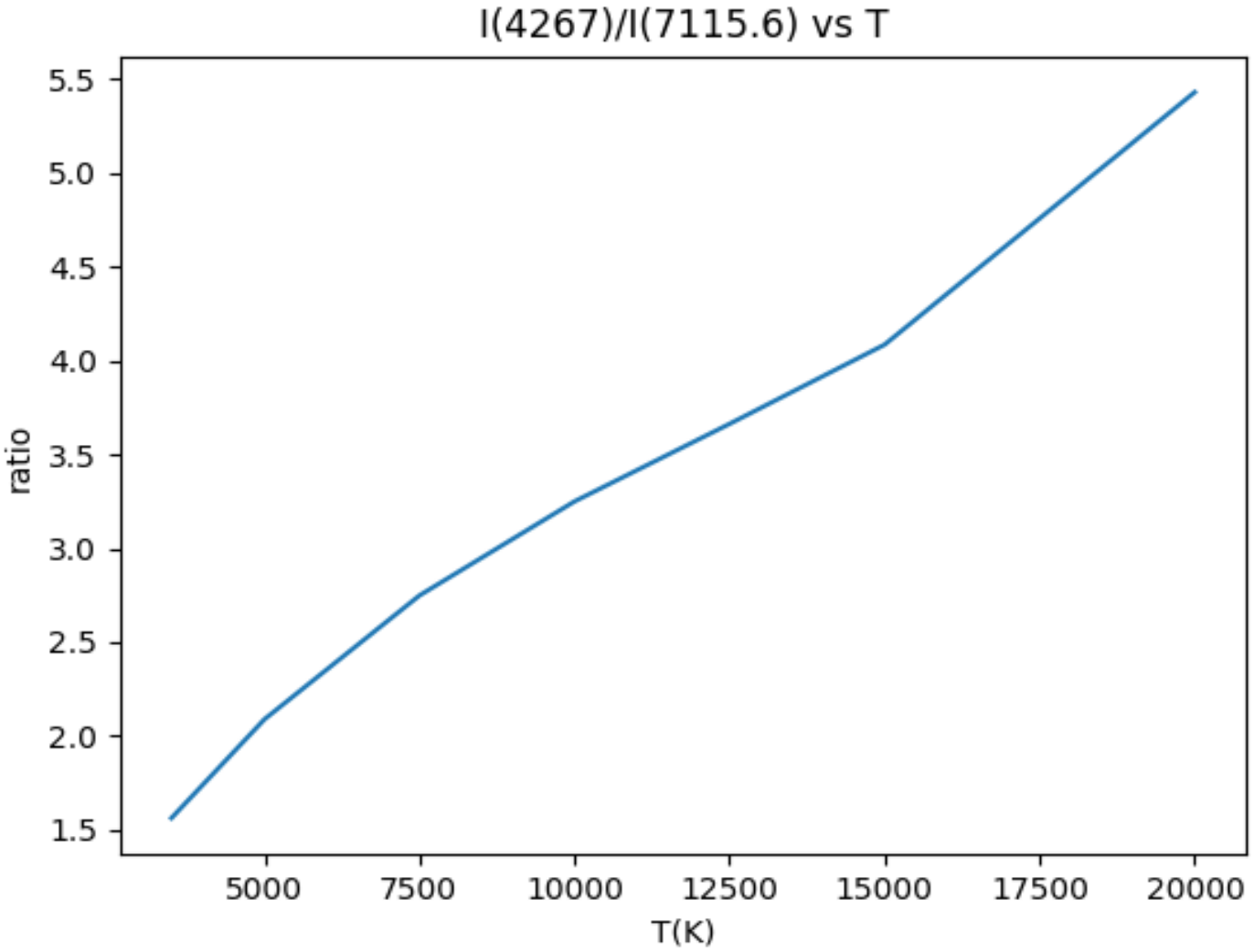

Figure 5.13: predicted ratio of C II 4267 Åand C II 7115 Åin regions where RER dominates

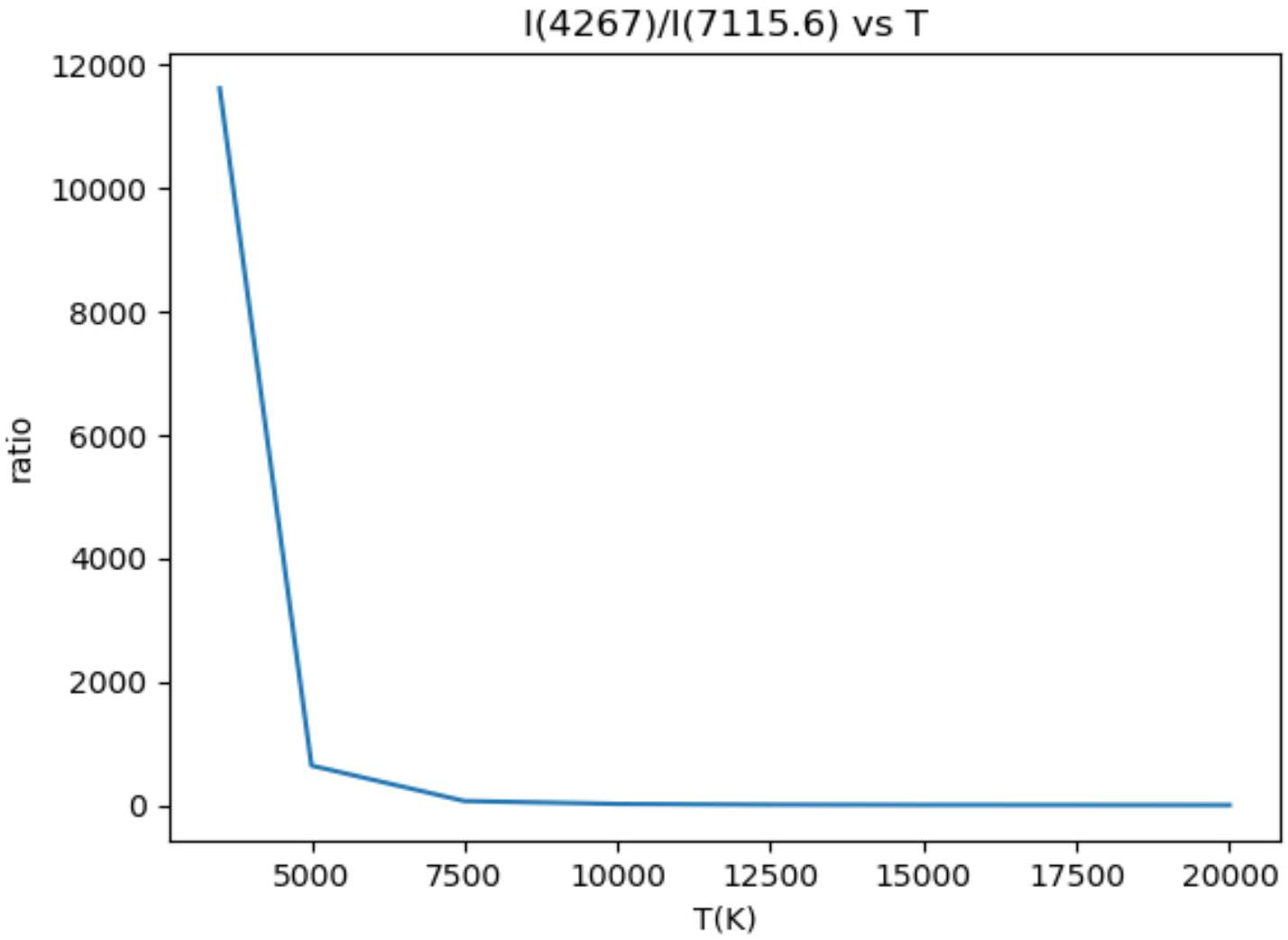

Figure 5.14: predicted ratio of C II 4267 Åand C II 7115 Åin regions where RER dominates

From the table of observed line ratios we can see that we have disparate results. Some of PNe have ratio above 100 and some have ratios as low as 20. As was discussed before, the nebulae are expected to have inhomogeneous physical conditions, and it is likely the that observed ratio comes from parts affected by RER and some that are not. We ran tailored models of some of these PNe using Cloudy (considering homogeneous conditions) using old and new rates. The simulated results using Cloudy can be split into to categories with the exception of an outlier. Low excitation PNe are a class of nebulae where the energy input reaching the ionized gas from the star is low, and as a result the gas is in a low excitation mode (low charge states only). On the contrary, high excitation PNe receive a higher energy deposit from the star. The energy deposited into the gas decreases with distance of the central star and increases the blackbody temperature of the star. For low excitation PNe the observed ratio was much closer to the one simulated without RER than with its inclusion as can be seen from Figs. 5.13 and 5.14. On the other hand, the observed line ratio for high excitation PNe was in between the simulated with and without the inclusion of RER. The exception is IC4191 where the observed line ratio was much higher than simulated with and without RER.

As can be seen from Fig. 5.15 , for low excitation PNe, the temperature is lower than 10,000 K which makes it ideal for RER occurrence. However, the observed line ratio suggests that RER is almost non-existent in them. This could be because the charge states producing the C II 7115 Å RER line are absent; C^{+} is abundant, but C^{2+} the recombining ion is missing. For high excitation PNe 5.16, the observed ratio suggests that RER occurs at least in some parts of the PNe. Contrary to low excitation PNe, the temperature is almost double than the low excitation one which makes it less ideal for RER. But the high excitation PNe have higher charge states, and the both ions required for RER are present. The RER lines are probably emitted from the region where both ions are present and the recombination is occurring. The lack of spatially resolved observations of these PNe makes difficult to make

any further conclusions on the occurrence of RER. This is an indication that RER is strongly correlated with the physical conditions of the plasma, and hence can be used as a probe for these conditions. IC4191 is the outlier in the sense that none of the above arguments apply Figure 5.17. The conditions assumed for this PN in our model are similar to the other high excitation PNe; higher temperature, higher charge states. But the observed ratio suggests that the simple modeled assumed for IC4191 does not work with it as well as the others, and we would be missing some important assumptions about that gas that would account for the observed ratio. It could be that there is a part of the plasma that has extreme low temperatures but without the sufficient conditions for RER, in that case the observed ratio would be dominated by emission from that region.

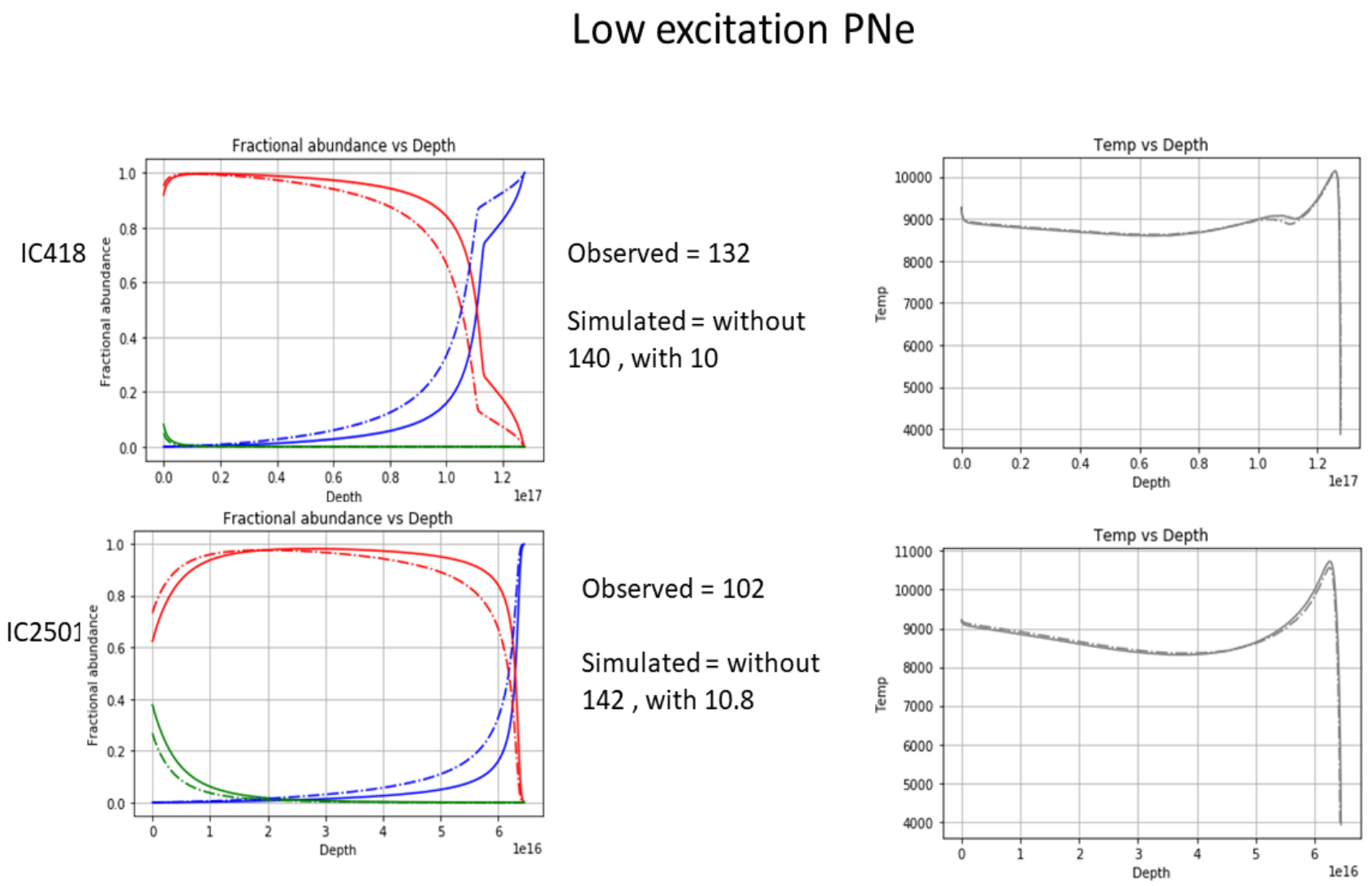

Figure 5.15: Cloudy simulations of low excitation PNe IC418 and IC2501

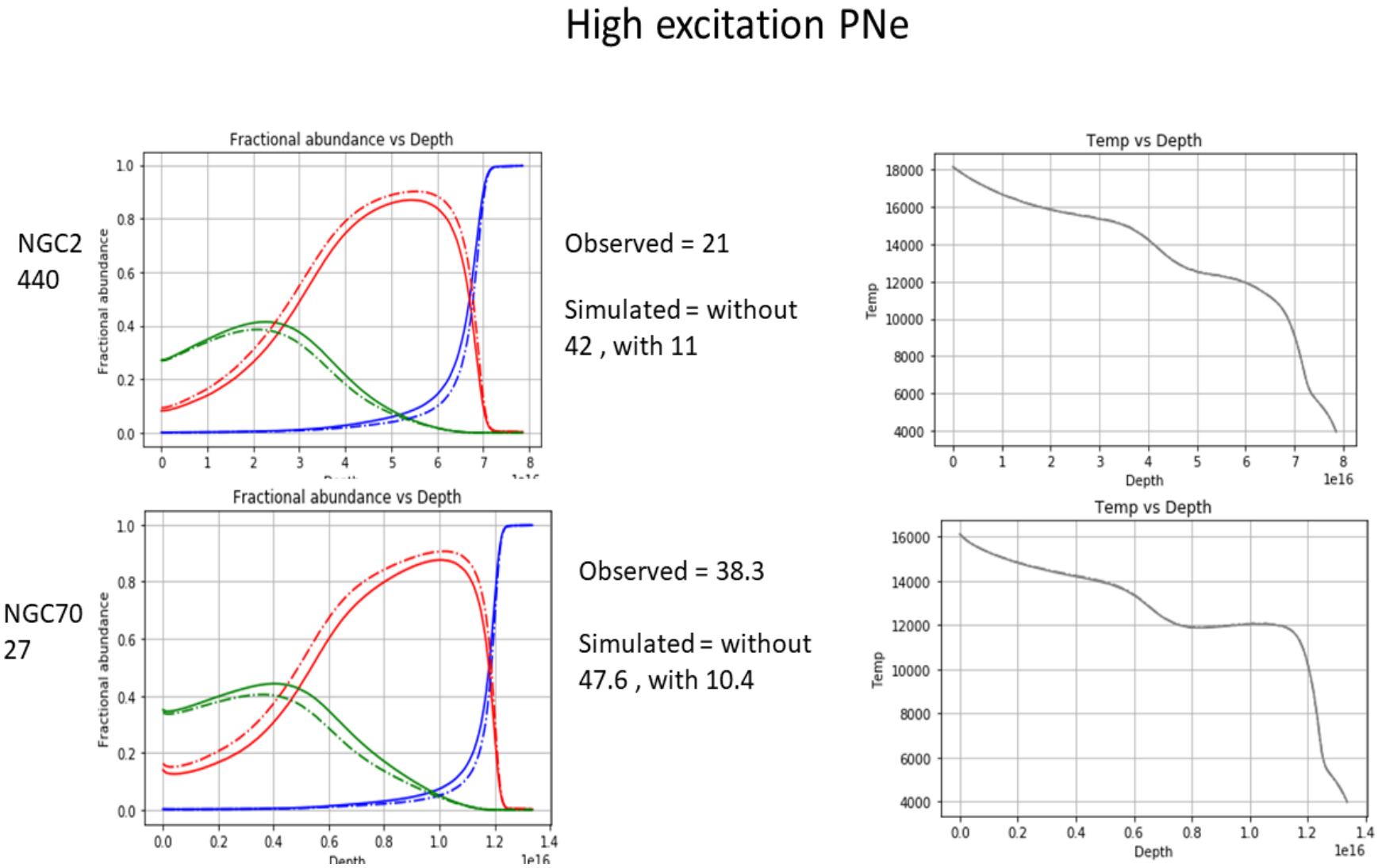

Figure 5.16: Cloudy simulations of high excitation PNe NGC2440 and NGC7027

High excitation PNe

IC4191

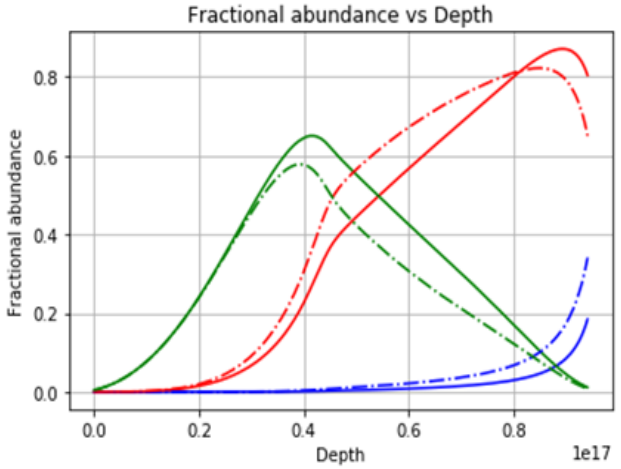

Observed = 203

Simulated = without 89
, with 10

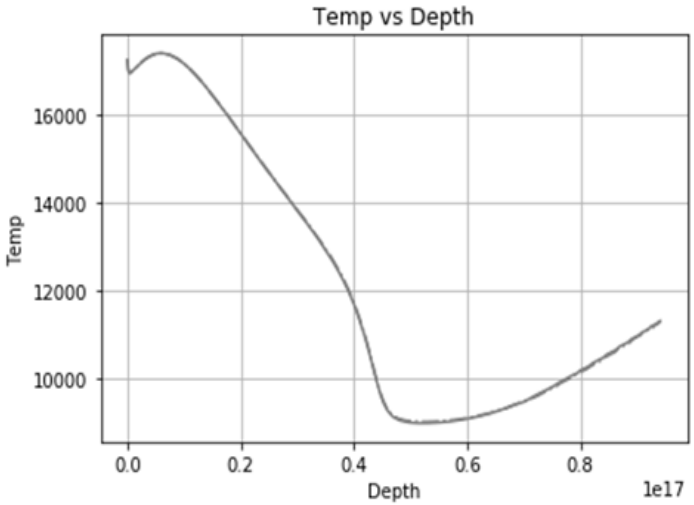

Figure 5.17: Cloudy simulations of high excitation PNe IC4191

Chapter 6

Hubble Space telescope proposals

Given that the first evidence of the RER mechanism has now been detected, the next step will be to investigate the process and characterize its occurrence. Moreover, we would like to see how the RER lines behave in environments with different physical conditions, and ultimately be able to determine if RER can resolve the AD problem. Since most of the RER emission lies in the UV, and we require high spectral resolution with high quality detection setup, we were constrained to use Hubble Space Telescope (HST). The time allocation for HST is very competitive and the proposal has to be very convincing to be accepted. Thus, we opted to apply for an Archival proposal this year to facilitate for an observational propsal next cycle. The Archival proposal would be dedicated to searching through existing spectra in the archives before we ask for an observational one. Below is found the archival proposal that was submitted. Many potential archived spectra were identified for this study.

6.1 HST Archival Proposal

Characterizing a New Recombination Process in Photoionized Plasmas through UV Spectroscopy, and Studying its Broader Implications for Elemental Abundance Determination

Scientific Category: Stellar Physics
Scientific Keywords: Chemical Abundances, Evolution, HII Regions, Planetary Nebulae, Radiative Transfer
Alternate Category: Stellar Populations
Budget Size: Regular

UV Initiative: Yes
Fundamental Physics: Yes

Abstract

Recent observations have revealed evidence of a new recombination process, Rydberg Enhanced Recombination (RER), that can potentially fundamentally alter our understanding of the thermal and ionization balance, and hence abundance determinations, of photoionized nebulae. It is critical to test model predictions for the dependence of RER on plasma conditions, which is not possible from the limited number of objects in which RER emission lines have thus far been detected. We propose to investigate archival HST spectra of a variety of ionized nebulae, with an emphasis on the astrophysically important elements C and O, whose RER emission is mostly in the UV. The aim of our proposal is to characterize RER as a function of temperature and density, using existing HST observations of planetary nebulae, H II regions, and symbiotic stars that span a large range of nebular temperatures and densities. The observed line intensities will be used to benchmark and improve synthetic spectral models in order to assess the effect of RER on abundance determinations, as well as to develop new temperature diagnostics from these transitions.

Characterizing a New Recombination Process in Photoionized Plasmas through UV Spectroscopy, and Studying its Broader Implications for Elemental Abundance Determination

Investigators:

Investigators and Team Expertise are included in this preview for your team to review. These will not appear in the version of the proposal given to the TAC, to allow for a double-blind review.

Investigator	Institution	Country
Dr. Andrea Dupree	Smithsonian Institution Astrophysical Observatory	USA/MA
Dr. Stuart Loch	Auburn University	USA/AL
Mr. Ahmad Nemer	Auburn University	USA/AL
Dr. John Charles Raymond	Smithsonian Institution Astrophysical Observatory	USA/MA
Dr. Nicholas C. Sterling	University of Western Georgia	USA/GA

Number of investigators: 5

Team Expertise:

PI Ahmad Nemer (AN) has expertise in spectral modelling and photoionization codes and will be responsible for the overall success of the work and will participate in all aspects of the investigation. Co-PI Nick Sterling (NS) is an expert in the analysis of astrophysical observations and will be responsible for analyzing the emission line spectra. In addition, NS will be supervising the training of two undergraduate students to work on data acquisition and reducing the sample set. Co-I Stuart Loch (SL) is an expert in making quality atomic data and will give support in generating the atomic data. Co-I John Raymond (JR) will contribute his expertise in plasma modelling and HST observation to in order to select the optimum targets and in the scientific discussion of the results. Co-I Andrea Dupree has expertise in analysis of ultraviolet stellar spectra and will provide instrument advice, important so that we can avoid systematics when comparing data across instruments and avoid uncertainties in data reduction pipelines.

- **Scientific Justification**

Background on Low-Temperature Photoionized Plasmas:

Photoionized astrophysical plasmas are some of the most prominent and diagnostically important objects in the universe. Different radiation sources can ionize gases directly such as: low-mass dying stars in the case of Planetary Nebulae; a hot compact object in symbiotic binaries: or young massive stars as found in H II regions. The chemical compositions of ionized nebulae play a critical role in our understanding of nucleosynthesis, stellar evolution, metallicities and the evolution of galaxies, and cosmology (*1–4*). However, abundance determinations in photoionized plasmas rely on the accurate conversion of ionic abundances to elemental abundances, requiring a detailed understanding of the atomic processes (specifically photoionization and recombination) that control the ionization equilibria of elements. Recently, we have found observational evidence for a new recombination process that fundamentally alters the ionization balance of nebulae, affecting the derived abundances of astrophysically important elements such as C and O. Lines formed by this process, known as Rydberg Enhanced Recombination (RER) were detected in 8 planetary nebulae and a symbiotic star system, in good agreement with theoretical predictions. Due to its importance in determining the charge state balance of elements in photoionized plasmas, particularly for C and O, it is now imperative to study a wider cross section of plasma conditions to thoroughly characterize the prevalence of RER and its emission behavior. **We propose an archival study of STIS, COS, and GHRS high-resolution spectroscopic observations of planetary nebulae, H II regions, and symbiotic stars to characterize RER in these objects as a function of density, temperature, and other features (see below) to reveal the importance of this potentially groundbreaking new atomic process in our understanding of these objects.**

The New Recombination Mechanism: The main processes responsible for recombination line production (Fig. 1) are the non-resonant Radiative Recombination (direct capture of a free electron; red arrows) and the resonant Dielectronic Recombination (a free electron is captured into an autoionizing state above the continuum threshold, accompanied by the excitation of a core electron; blue arrows). Dielectronic Recombination has been essential in explaining mysterious behavior of line emission (*5*, *6*) and is critical in understanding the temperature of the solar corona (*7*). Robicheaux et al. (*8*) pointed out that a process very similar to Dielectronic Recombination should be possible between high energy singly-excited states near the ionization threshold of an ion (also called Rydberg states) and below threshold doubly-excited states of the same ion that are coincident in energy (that is, free electrons are captured into states *below* the ionization threshold). We call this process Rydberg Enhanced Recombination (RER, green arrow in Fig. 1). RER substantially changes plasma conditions when added to modelling codes. **The inclusion of these states can increase the recombination rate coefficients at temperatures below 11000 K.** For example, RER increases the C^{2+} recombination rate at 9000 K by 100% (Fig. 2), with larger increases for lower temperatures. By incorporating RER into a Cloudy model for a planetary nebula with similar temperature (~ 10,000 K), the abundance of C^{3+} increased by a factor of two in

the region of emission. Consequently, we expect that RER will alter the fractional abundances of C and O ions and hence elemental abundance determinations. High-resolution spectroscopy is critically important for characterizing the RER lines, both to resolve these lines from nearby features of other species and to provide greater line-to-continuum contrast. Recently we found evidence for RER in eight planetary nebulae via the detection of optical C II lines (Fig. 3), and by a C III UV line in the symbiotic star AG Pegasi (which was not identified by Eriksson et al. (9); Fig. 4). Using the reported relative intensities of the C III RER line and C IV resonance lines, we estimate an electron temperature of ~11,000 K, which is consistent with the temperatures required for significant RER contribution to the C III emission. These observations of the RER lines are the first confirmation of the RER process.

Specific Objectives: Table 1 shows a list of important RER lines that we will search for in HST archival data. Some of the optical C II lines have been detected (and C III 1553 in AG Pegasi), but our models indicate that most of the RER emission lies in the UV. Therefore the UV transitions can be used to study RER in a much larger sample of objects than was previously possible, with a much wider range of physical conditions than in the 9 objects we have analyzed to date. Specifically, we have identified a large number of high-resolution observations within the MAST archive to study the RER process, with HST spectroscopic data on **1354 planetary nebulae, 326 symbiotic star systems and 530 H II regions.**

The variety of objects that will be covered in this study will allow the RER emission features to be characterized against a wide range of plasma conditions and ionizing radiation fields. Our models predict that the RER line intensity grows dramatically as the electron temperature decreases below about 11,000 K (Fig. 2), while other permitted lines show the opposite behavior. In addition, since the populations of the Rydberg states depend on electron density, the RER emission has a non-linear dependence upon density. It is critical to benchmark our model predictions of the dependence of RER on electron temperature and density against observations, in order to accurately assess the impact on derived elemental abundances. Moreover, the difference in the density and temperature dependence of RER lines compared to other recombination populated lines makes RER lines a potential diagnostic, but only if their density and temperature behaviors are well understood. The UV Carbon RER emission lines Table 1 lie in the proximity of forbidden lines from the same ions, which makes them ideal for this study.

The archived spectra represent a much wider temperature and density ranges than the limited studied set of nebulae in which RER has been studied to date, hence has only been characterized for a small range of plasma conditions. For example, symbiotic stars, which consist of photoionized gas surrounding a binary white dwarf and red giant system, have densities between 10^5 - 10^{10} cm^{-3}. The temperature of the hot component (White Dwarf) ranges between 3 x 10^4 – 2 x 10^5 K while the cold component (Red Giant) ranges between 1000 – 3500 K, and the surrounding nebula has lower temperatures. On the other hand, Planetary Nebulae show temperatures of as low as 1000 K for permitted lines (*9*) up to 18,000 K and densities between 10^3 – 10^6 cm^{-3} while the conditions of H II regions span 2000 – 10,000 K and 10^2 – 10^6 cm^{-3}. We will also study the prevalence of RER as a

function of metallicity (determined from the O abundance, which we will recompute with models incorporating RER). Low metallicity nebulae typically exhibit high electron temperatures, and are exposed to a harder radiation field, which alters the ionization balance of elements.

Abundance Discrepancy Problem: Abundance determinations in photoionized nebulae have long been plagued by an unresolved dichotomy between the abundances derived from forbidden and permitted lines (*10*). Specifically, ionic abundances derived from permitted lines are higher than those from forbidden lines, with discrepancies of up to a factor of 700 (*9*). Liu et al (*11*) proposed a bi-abundance model, with permitted lines preferentially emitted in cold, metal rich clumps, while Peimbert et al (*12*) proposed that temperature fluctuations are responsible for the dichotomy. Both of these theories posit that the gas has non-homogeneous temperature conditions, and that the observed spectrum is thus a superposition of the emission from both hot and cold regions. The lack of accurate diagnostics for the colder regions has been a key challenge for testing these models, in addition to the scarcity of spatial information from different locations in the gas. We note that the unique temperature and density dependence of RER lines makes them ideal probes for local plasma conditions in nebulae. Many authors have argued historically about the existence of a "hidden atomic process" that could complete the description of line production mechanisms necessary to resolve the Abundance Discrepancy problem (*13–15*). Ferland et al. (*16*) have shown that the lack of reliable Dielectronic Recombination rates is the dominant source of uncertainty in atomic parameters needed for ionization balance calculations of photoionized plasmas.

Nebulae seldom have uniform density, temperature and abundances, and these non-homogeneities have a direct effect on the observed discrepancies. Multiple studies (*16*, *17, and refereneces therein*) have mapped these non-homogeneities in the nebulae through forbidden and permitted lines that trace different structures. When spatially resolved HST data are available, we will map RER lines to compare to those of permitted and forbidden transitions. **The RER emission lines uniquely trace low temperature region because of its temperature dependence.**

In summary, we will characterize RER in a large number of astrophysical objects for the first time, and study correlations between RER and temperature, density, metallicity, and abundance discrepancy factors. This program will substantially improve our understanding of this process in a wide range of Galactic and extragalactic objects, with critical implications for abundance determinations of astrophysically important elements such as C and O, and for the long-standing abundance discrepancy problem.

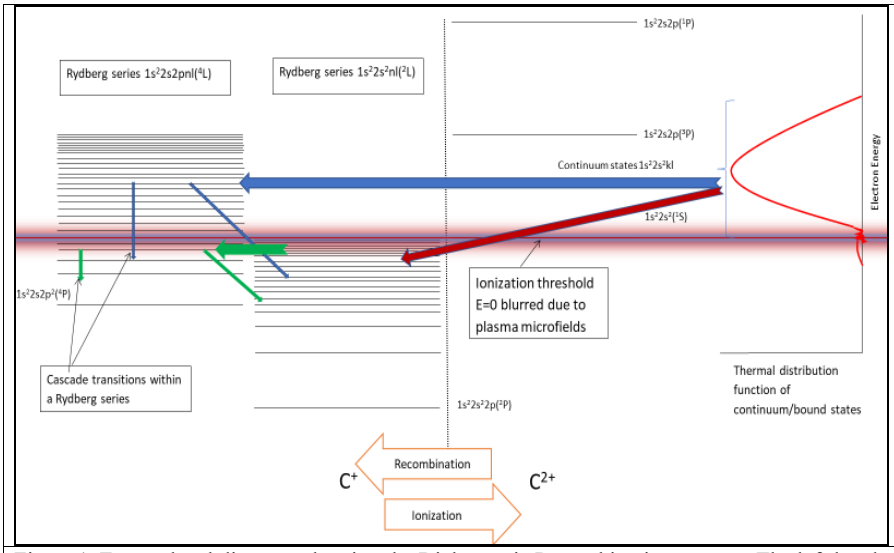

Figure 1: Energy level diagram, showing the Dielectronic Recombination process. The left-hand side of the figure shows the energy levels of C^+, with the blurred line representing the ionization threshold (and the ground state of C^{2+}). Two series of energy levels are shown, the singly excited $1s^22s^2nl$ series, and the doubly excited $1s^22s2pnl$ series. On the right-hand side the electron distribution function is shown, extending to energies above and below the ionization potential.

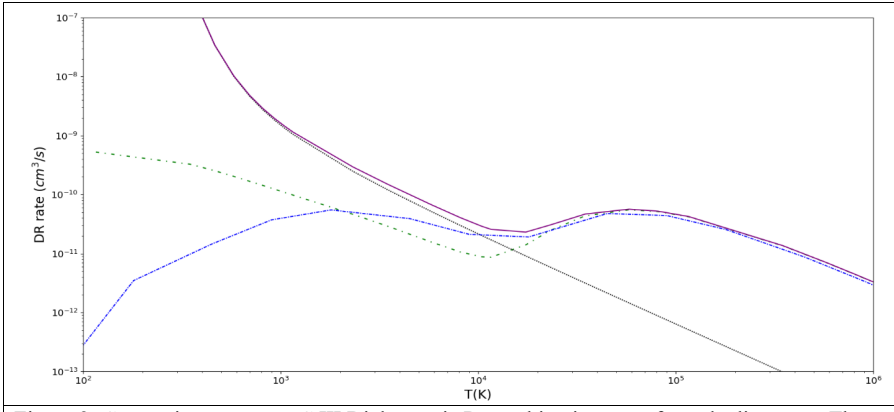

Figure 2: Comparison amongst C III Dielectronic Recombination rates from the literature. The green curve represents Badnell et al (*19*). calculated rates, the blue curve is our calculated rates for above threshold Dielectronic Recombination only, and the black curve is our calculated Rydberg Enhanced Recombination (RER) rate. The purple curve is the recommended total rates produced by combining the measured Dielectronic Recombination rates with the RER contribution

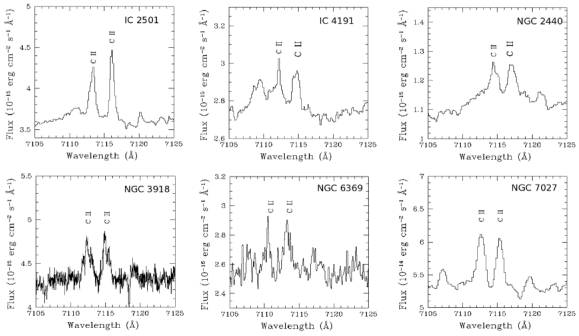

Figure 3. From left to right and from top to bottom: high-resolution spectra showing the C II RER emission lines at 7112 and 7115 Å for 6 Planetary Nebulae: IC 2501, IC 4191, NGC 2440 (*20*), NGC 3918 (*21*), NGC 6369 (*22*) and NGC 7027 (*20*). These spectra confirm RER.

Table 1 – Preditced RER line list

Element and ion stage	Term (multiplet) Term (multiplet)	Energy below ionization potential (eV)	Wavelength of strongest transitions (A)
C II	$1s^2 2s2p(^3P)3d(^4F)$	0.105355-0.112927	7115.53,7134.03, 7112.94,7119.73
C III	$1s^2 2p4p(^1D)$	0.07475-0.05254	1581.43, 1623.25, 1512.93
C III	$1s^2 2p4p(^3F)$	0.05148	1593.65,1594.27, 2799.19,1553.38
O III	$1s^2 2s^2 p^2(^4P)4p(^5P)$	0.45183-0.59911	2430.3,2427.66,2426.78

Table 1. C and O RER transitions and energies. UV wavelengths are in vacuum, optical wavelengths in air.

- **Analysis Plan**

We will search for RER emission lines in about 2210 high-quality archival HST spectra of photoionized astrophysical plasmas including 1354 Planetary Nebulae, 326 Symbiotics, and 530 H II regions. The detected C II, C III, and O III RER emission lines will be measured and characterized in terms of nebular electron temperature T_e and density n_e, and other properties such as the existing discrepancies in elemental abundance determinations.

Our investigation will be based on non-proprietary HST STIS, COS, and GHRS observations of Planetary Nebulae, Symbiotic binaries, and H II regions. The comparison

of RER line intensities and ratios for different physical conditions and radiation fields will provide critical new constraints to our models in a wider temperature and density parameter space than is viable through optical observations alone, owing to the relative strength of UV RER lines. Data sets with high spatial and spectroscopic resolution (*9*, *23–25*) are of particular interest for the use of RER lines as diagnostic probes of temperature and density inhomogeneities. A sample of a GHRS UV observation from the archives is shown in Fig. 4. Other key data sets are those with high exposure times to facilitate for the detection of weak lines. Our analysis of the UV spectra will be used to inform future high resolution ground-based observations, to search for additional RER lines of diagnostic value.

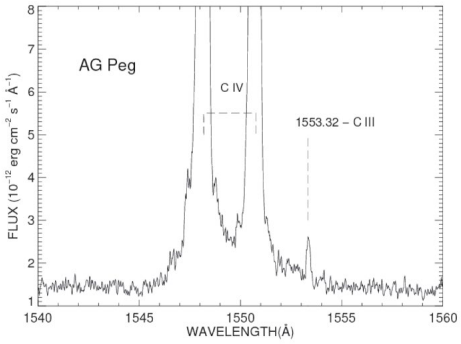

Figure 4) Sample UV spectrum for AG Pegasi showing the C III 1553 Å line (*26*) taken from HST archive.

Moreover, if the optical spectra needed are not available, we have access to telescopes in the Northern (MMT 6.5m Telescope and the 1.5-meter Tillinghast reflector telescopes both in Arizona) and the Southern hemisphere (6.5m Magellan telescopes in Chile) to acquire high-resolution optical spectra to complement the UV spectra. As an additional resource, we will be accessing the HST Spectroscopic Legacy Archive to look for additional spectra; we found a large number of Symbiotics star spectra there.

Data Processing: The first task will be to select targets for further analysis from the large number of observations available. To do so, we will create quick-look plotting procedures centered on the predicted wavelengths of RER lines. For targets exhibiting one or more RER lines (Table 1), we will measure the fluxes of these lines as well as other C and O transitions, and diagnostically important lines of other species. Extinction coefficients c(H_β) will be taken from the literature, as well as electron temperatures and densities from various diagnostic line ratios. In cases where relevant lines are available from STIS optical data, we will determine T_e, n_e, and abundances using the nebular analysis package PyNeb (*27*). The data on The Mikulski Archive for Space Telescopes (MAST) are fully reduced. So, the main tasks are to develop software to plot and measure emission line strengths. We will utilize existing codes to plot and measure emission line fluxes that have been developed by the Co-PI.

Spectral Modelling: The theoretical methods required for predicting spectral lines that result from RER involve the transition rate between Rydberg states and doubly excited states just below the ionization potential. The method of calculating such rates is analogous to the regular dielectronic capture methodology as described in (*8*). For this project two atomic structure codes were modified, the multi-configuration Breit-Pauli atomic structure code AUTOSTRUCTURE (*28*) and the multi-configuration Dirac-Fock code GRASP (*29*). We also used a collisional-radiative model to calculate level populations and line emissivities necessary for radiative rates; the code used for that purpose is ADAS (*30*). All those transition parameters will be used to generate a synthetic spectrum for the desired physical conditions to match with observations.

Management Plan: The timeline for this 1 year investigation is as follows:

Months 1 – 2 : download and preliminary inspection of all data from the search described above.

Months 3 – 6 : Measure emission line intensities and make conclusions about the relevant spectra for the goal of looking for inhomogeneities.

Months 4 – 7 : Modelling of the reduced sample set to match with observations and finding optimum conditions for RER.

Months 6 – 9: Consolidate conclusions about RER emission (Which of these observations can be used to address the Abundance Discrepancy problem) and make viable comparisons between select spectra.

Months 9 – 12: Prepare figures, write-up for publication, submit to journal. Prepare and deliver final report.

1. D. Zaritsky, R. C. . J. Kennicutt, J. P. Huchra, H II regions and the abundance properties of spiral galaxies. *Astrophys. J.* **420**, 87 (1994).
2. F. Hamann, G. Ferland, Elemental Abundances in Quasistellar Objects: Star Formation and Galactic Nuclear Evolution at High Redshifts. *Annu. Rev. Astron. Astrophys.* **37**, 487–531 (1999).
3. D. W. Savin, Ionization Balance, Chemical Abundances, and the Metagalactic Radiation Field at High Redshift. *Astrophys. J.* **533**, 106–112 (2000).
4. R. B. C. Henry, B. G. Stephenson, M. M. Miller Bertolami, K. B. Kwitter, B. Balick, On the production of He, C, and N by low- and intermediate-mass stars: a comparison of observed and model-predicted planetary nebula abundances. *Mon. Not. R. Astron. Soc.* **473**, 241–260 (2018).
5. A. K. Dupree, L. Goldberg, Radiofrequency Recombination Lines. *Annu. Rev. Astron. Astrophys.* **8**, 231–264 (1970).
6. J. H. Parkinson *et al.*, An investigation of the 1.9 A feature in solar-flare X-ray spectra. *Astrophys. J.* **231**, 551 (1979).
7. Burgess A Alan, Delectronic Recombination and the Temperature of the Solar Corona. *Astrophys. J.* **139**, 776 (1964).
8. F. Robicheaux, S. Loch, M. Pindzola, C. Ballance, Contribution of Near Threshold States to Recombination in Plasmas. *Phys. Rev. Lett.* **105**, 233201 (2010).
9. R. Wesson, X.-W. Liu, M. J. Barlow, Physical conditions in the planetary nebula Abell 30. *Mon. Not. R. Astron. Soc. Vol. 340, Issue 1, pp. 253-263.* **340**, 253–263 (2003).
10. A. ~B. Wyse, The Spectra of Ten Gaseous Nebulae. *Astrophys. J.* **95**, 356 (1942).
11. X. Liu, P. Storey, NGC 6153: a super-metal-rich planetary nebula? *Mon. Not. ….* **312**, 585–628 (2000).
12. M. Peimbert, TEMPERATURE DETERMINATIONS OF H n REGIONS. *Astrophys. J.* **150**, 825 (1967).
13. C. Rola, G. Stasi'nska, The carbon abundance problem in planetary nebulae. *A&A*. **282**, 199–212 (1994).
14. T. Barker, T., The ionization structure of planetary nebulae. III - NGC 7009. *Astrophys. J.* **267**, 630 (1983).
15. J. P. Harrington, W. A. Feibelman, The remarkable ultraviolet spectrum of the planetary nebula Abell 30. *Astrophys. J.* **277**, 716 (1984).
16. G. J. Ferland *et al.*, CLOUDY 90: Numerical Simulation of Plasmas and Their Spectra. *Publ. Astron. Soc. Pacific*. **110**, 761–778 (1998).
17. D. R. Garnett, H. L. Dinerstein, Spatially-Resolved O II Recombination Line Observations of the Ring Nebula, NGC 6720. *Astrophys. J.* **558**, 145–156 (2001).
18. J. García-Rojas *et al.*, Imaging the elusive H-poor gas in the high ADF planetary nebula NGC 6778. *Astrophys. J. Lett. Vol. 824, Issue 2, Artic. id. L27, 5 pp. (2016).* **824** (2016), doi:10.3847/2041-8205/824/2/L27.
19. J. Colgan, M. S. Pindzola, A. D. Whiteford, N. R. Badnell, Dielectronic recombination data for dynamic finite-density plasmas. *Astron. Astrophys.* **412**, 597–601 (2003).
20. B. Sharpee *et al.*, s-Process Abundances in Planetary Nebulae. *Astrophys. J.* **659 (2)**, 1265–1290 (2006).

21. J. García-Rojas *et al.*, s-process enrichment in the planetary nebula NGC 3918. Results from deep echelle spectrophotometry. *MNRAS*. **452**, 2606–2640 (2015).
22. J. García-Rojas, M. Peña, C. Morisset, A. Mesa-Delgado, M. T. Ruiz, Astrophysics Analysis of chemical abundances in planetary nebulae with [WC] central stars I. Line intensities and physical conditions. *A&A*. **538**, 54 (2012).
23. J. H. Bieging, P. A. Boley, W. B. Latter, A. G. G. M. Tielens, A Search for Temperature and Density Variations in NGC 7027 with the *Hubble Space Telescope*. *Astrophys. J.* **676**, 390–401 (2008).
24. T. R. Miller *et al.*, Co-spatial UV-optical HST/STIS Spectra of Six Planetary Nebulae: Nebular and Stellar Properties. *Mon. Not. R. Astron. Soc. Vol. 482, Issue 1, p.278-292*. **482**, 278–292 (2018).
25. R. J. Dufour *et al.*, Co-spatial Long-slit UV/Optical Spectra of Ten Galactic Planetary Nebulae with HST/STIS I. Description of the Observations, Global Emission-line Measurements, and CNO Abundances. *Astrophys. Journal, Vol. 803, Issue 1, Artic. id. 23, 24 pp. (2015).* **803** (2015), doi:10.1088/0004-637X/803/1/23.
26. M. Eriksson, S. Johansson, G. M. Wahlgren, The nature of ultraviolet spectra of AG Pegasi and other symbiotic stars : locations , origins , and excitation mechanisms of emission lines. **175**, 157–175 (2006).
27. V. Luridiana, C. Morisset, R. A. Shaw, PyNeb: a new tool for analyzing emission lines. I. Code description and validation of results. *Astron. Astrophys. Vol. 573, id.A42, 14 pp.* **573** (2014), doi:10.1051/0004-6361/201323152.
28. N. R. Badnell, A Breit–Pauli distorted wave implementation for autostructure. *Comput. Phys. Commun.* **182**, 1528–1535 (2011).
29. K. G. Dyall, I. P. Grant, C. T. Johnson, F. A. Parpia, E. P. Plummer, GRASP: A general-purpose relativistic atomic structure program. *Comput. Phys. Commun.* **55**, 425–456 (1989).
30. A. Giunta, H. Summers, P. Bryans, M. O'mullane, "ADAS-EU ADAS for fusion in Europe Grant: 224607 Generalised-collisional-modelling for light-and medium-weight elements" (2012).

6.2 HST Observational Proposal

In preparation for a future HST proposal, we outline below some of the considerations on hardware, observed fluxes, and the required observing time. To investigate the AD problem using HST observations, we want to have multiple long slit locations in within the nebula. The Space Telescope Imaging Spectrograph (STIS) uses two-dimensional detectors operating from the ultraviolet (UV) to the near-infrared (NIR). First-order gratings cover the full spectral range and are designed for spatially resolved spectroscopy using a long slit. The echelle gratings, available only in the UV are designed to maximize the spectral coverage in single observations of point sources. These two functionalities of STIS makes it perfect for use to achieve our goal.

The full UV/optical spectrum covering exactly the same spatial regions is needed to figure out why the Cloudy models cannot reproduce the observed line intensities. We will mostly need low resolution for the diagnostic lines, but we will need moderate resolution for the RER lines because of their weakness in detection. Spectral resolution R = $\lambda/\Delta\lambda$ where $\Delta\lambda$ is the resolution element, the difference in wavelength between two equally strong (intrinsically skinny) spectral lines that can be resolved, corresponding to the projected slit width in wavelength units; values of hundreds are considered low, thousands are moderate, while tens of thousands is considered high resolution spectrum. Table 1.2 shows useful diagnostic line ratios to be used for this purpose.

The resolution is also compromised with the slit width to be used. If you are limited by photon statistics, the 2" wide slit is best. If the faint lines are limited by background (dark current or nebular continuum), the signal is proportional to slit width, but the background goes as width^2, so the noise also goes as slit width. The wide slit costs resolution, which can be important for optical depth effects if you want to use resonance lines such as C IV, Si IV, N V. We would like STIS spectra with the 52" slit that cover knots like those in Abell 30

and the Helix, as well as the edge of the photoionized gas (if possible), to cover the interfaces and changes in ionization state.

Next to consider is the exposure time calculations.One has to be careful that exposure time estimates are not drastically underestimated, if we are using the magnitude of the PN. Taking NGC 6153, according to SIMBAD (http://simbad.u-strasbg.fr/simbad/) its B magnitude is 10.7. But this corresponds to the flux from the entire nebula, which has a diameter of 24 arcsec. So even if we use a 2" width slit, only a small fraction of the nebula's flux will be observed. And Abell 30 has an optical diameter of 127", though the knots are some of the higher surface brightness features of that PN. Instead, we find the Hβ flux for a given slit position in the literature, along with the extinction coefficient, and estimate the reddening-corrected intensity of the lines. Or, in the case of NGC 6153, the He II 4686 intensity would provide a more direct comparison to the UV spectral regime of STIS (specifically, He II 1640). The exposure time calculators for HST are not meant for extended emission line objects. Generally we have to bin the data to get reasonable S/N. We could use the flux estimates and multiply by the HST mirror area and throughput to get the number of counts in the lines as a sanity check. it would be beneficial to find some other STIS spectra of PNe that don't include the central star.

We also have an option to use the Cosmic Origins Spectrograph (COS). In most spectrographs the light from the telescope is focused onto a slit, which is then re-imaged onto the detector. In such a design the slit width and the way that the slit is illuminated determine the resolving power and LSF. COS is different. It is essentially a slitless spectrograph with an extremely small field of view. The Primary Science Aperture (PSA) is a circular field stop 2.5 arcsec (700 m) in diameter. It is located, not at the HST focal surface, but near the point of the circle of least confusion. The aperture transmits 95% of the light from a well-centered, aberrated point-source image delivered by the HST optics. The PSA is used

for almost all COS science observations. After passing through one of the COS apertures light next encounters the Optics Select Mechanism 1 (OSM1), a rotating mechanism that can bring one of four optical elements into the beam. One of these, NUV Collimating Mirror 1 (NCM1), is a flat mirror that directs the beam to the NUV channel. The other three elements are the G130M, G160M, and G140L gratings for the FUV channel. As a consequence of this design the FUV and NUV channels cannot be used simultaneously.

The primary design goal of COS is to improve the sensitivity of HST to point sources in the far-ultraviolet (FUV) (from about 1100 to 1800). In this wavelength range, the throughput of the COS FUV channel exceeds that of the STIS FUV-MAMA by factors of 10 to 30, and the combination of the spectroscopic resolving power (20,000) and wavelength coverage (300 to 370 per setting) of the medium-resolution COS FUV modes results in a discovery space (throughput times wavelength coverage) for observations of faint FUV point sources that is at least 10 times greater for most targets than that of STIS modes with comparable resolution, and is as much as 70 times greater for faint, background-limited point sources.

Chapter 7

Conclusions and Future work

This work has focused on the calculation of DR rates and synthesizing a spectrum for C^{+} and C^{2+} to find an evidence of and illustrate the effect of including RER in DR rates and modelling codes. The next step of the project is to produce RER rates for a wide range of elements relevant to astronomy. We plan to identify the important ions for cooling and calculate new rates for them. With the aid of photoionization codes, we will integrate these new rates and study their cooling effect. Moreover, the addition of RER will change the effective rates for known ORLs which would need to be studied with a radiative transfer model that calculate predicted intensities and then compared with observations.

Furthermore, the majority of emission for RER lies in the UV. We would need to study a larger sample of RER lines from different ions and different astrophysical environments to characterized RER. As mentioned in chapter 6, we applied for an archival proposal to study the archived data available in HST's archives to achieve that purpose. We would use the papers that these data has appeared in to understand the emitting environment; namely the physical conditions like electron temperature and metallicity. Based on these parameters we will make prediction models for the RER lines and study their behaviour with various physical conditions. Moreover, we will apply for observing time on HST. This proposal will be guided by our previous efforts to characterize RER and what is available (or not available) in the literature. This work will be focused on studying lines that would in most relevance to the AD problem. We would like to study one of the PNe with the highest ADF such as Abell 30.

As mentioned in chapter 4, the Rydberg states of ions affected by RER will be disturbed by the depopulating specific resonant states. This disturbance to the population will create non-LTE conditions that can be observed and studied with RRLs like maser emission. The emission of the radio lines is expected to be correlated with density effects in the plasma (i.e. continuum lowering and microfields). We would like to apply for an observing time using a radio telescope like Atacama Large Millimeter/submillimeter Array (ALMA) or the SubMillimeter Array (SMA) at Harvard. By observing the Rydberg states using radio recombination lines, it should be possible to explore effects such as continuum lowering, as well as using the Rydberg states to provide evidence of the positions of the below threshold doubly excited states.

Consequently, we expect other processes that interact with the Rydberg states to be affected by their population and interaction with the doubly excited states. For instance, there is a significant portion of ions suspected to be in the ground state that are now in a Rydberg state of the previous charge state. This could affect ionization and recombination processes the same. In addition radiative processes in ions are expected to be affected by the disturbance in the Rydberg states.

Last but not least, we would like to conduct a lab experiment that would lead to RER. Instead of having the Rydberg states populated due to plasma effects with their thermal distribution, we can excite the ions to specific states like the Rydberg states. This procedure could be done using Electron Beam Ion Traps (EBIT). The EBIT is a small-scale laboratory instrument which uses a tightly focused and energy-tunable electron beam to create, trap, and probe highly charged ions. Virtually any charge state of any element in the periodic table can be studied using an EBIT simply by injecting the desired element and adjusting the electron beam energy appropriately. In the case of Rydberg states, tuning the energy exactly will be difficult because of their narrow energy range. Instead we could promote

the ions to high doubly excited states ($1s^2 2s 2pnl$) with the desired nl for the Rydberg state which will decay to ($1s^2 2s^2 nl$) Rydberg state. Then we can direct this excited ion beam to a low temperature chamber where we can observe the recombination processes. This work is still in design and will be initiated once we find an ion proper for such an experiment.

Bibliography

[1] N.R. Badnell. A BreitPauli distorted wave implementation for autostructure. *Computer Physics Communications*, 182(7):1528–1535, jul 2011.

[2] F Robicheaux, SD Loch, MS Pindzola, and CP Ballance. Contribution of Near Threshold States to Recombination in Plasmas. *Physical Review Letters*, 105(December):233201, 2010.

[3] G J Ferland, M Chatzikos, F Guzmán, M L Lykins, P A M Van Hoof, R J R Williams, N P Abel, N R Badnell, F P Keenan, R L Porter, and P C Stancil. THE 2017 RELEASE OF Cloudy. *Revista Mexicana de Astronomía y Astrofísica*, 53(385-438), 2017.

[4] K. B. Kwitter, R. H. Méndez, M. Peña, L. Stanghellini, R. L.M. Corradi, O. De Marco, X. Fang, R. B.C. Henry, A. I. Karakas, X. W. Liu, J. A. López, A. Manchado, and Q. A. Parker. The present and future of planetary nebula research. A white paper by the IAU planetary nebula working group. *Revista Mexicana de Astronomia y Astrofisica*, 50(2):203–223, 2014.

[5] A.˜B. Wyse. The Spectra of Ten Gaseous Nebulae. *Apj*, 95(4):356–+, 1942.

[6] Manuel Peimbert, Antonio Peimbert, and Gloria Delgado-Inglada. Nebular spectroscopy: A guide on HII regions and planetary nebulae. *Publications of the Astronomical Society of the Pacific*, 129(978), 2017.

[7] Robin Ciardullo, John J. Feldmeier, George H. Jacoby, Rachel Kuzio de Naray, Mary Beth Laychak, and Patrick R. Durrell. Planetary Nebulae as Standard Candles. XII. Connecting the Population I and Population II Distance Scales. *The Astrophysical Journal*, 577(1):31–50, sep 2002.

[8] Amanda I. Karakas and John C. Lattanzio. The Dawes Review 2: Nucleosynthesis and Stellar Yields of Low- and Intermediate-Mass Single Stars. *Publications of the Astronomical Society of Australia*, 31, jul 2014.

[9] B. E. J. (Bernard Ephraim Julius) Pagel. *Nucleosynthesis and chemical evolution of galaxies*. Cambridge University Press, 2nd ed. edition, 2009.

[10] Hagai B. Perets and Scott J. Kenyon. Wind-accretion disks in wide binaries, second generation protoplanetary disks and accretion onto white dwarfs. *The Astrophysical Journal, Volume 764, Issue 2, article id. 169, 9 pp. (2013).*, 764, mar 2012.

[11] J. Mikołajewska and J. Symbiotic stars: Observations confront theory. *Baltic Astronomy, Vol. 21, p. 5-12*, 21:5–12, oct 2011.

[12] P. F. Roche, D. A. Allen, and D. K. Aitken. Symbiotic stars: spectrophotometry at 3-4 and 8-13 m. *Monthly Notices of the Royal Astronomical Society*, 204(4):1009–1015, oct 1983.

[13] Krzysztof Belczynski, Vassiliki Kalogera, and Tomasz Bulik. A Comprehensive Study of Binary Compact Objects as Gravitational Wave Sources: Evolutionary Channels, Rates, and Physical Properties. *The Astrophysical Journal, Volume 572, Issue 1, pp. 407-431.*, 572:407–431, nov 2001.

[14] Burgess A Alan. Delectronic Recombination and the Temperature of the Solar Corona. *The Astrophysical Journal*, 139:776, 1964.

[15] Donald D. Clayton. *Principles of stellar evolution and nucleosynthesis : with a new preface*. University of Chicago Press, 1983.

[16] Edward B. Jenkins and Edward B. A Unified Representation of Gas-Phase Element Depletions in the Interstellar Medium. *The Astrophysical Journal, Volume 700, Issue 2, pp. 1299-1348 (2009).*, 700:1299–1348, may 2009.

[17] Leticia Carigi, Manuel Peimbert, Cesar Esteban, and Jorge GarciaRojas. Carbon, Nitrogen, and Oxygen Galactic Gradients: A Solution to the Carbon Enrichment Problem. *The Astrophysical Journal*, 623(1):213–224, apr 2005.

[18] Donald E. Osterbrock and Gary J. Ferland. Astrophysics of gaseous nebulae and active galactic nuclei. *Astrophysics of gaseous nebulae and active galactic nuclei, 2nd. ed. by D.E. Osterbrock and G.J. Ferland. Sausalito, CA: University Science Books, 2006*, 2006.

[19] G.J. Ferland, K.T. Korista, D.A. Verner, J.W. Ferguson, J.B. Kingdon, and E.M. Verner. CLOUDY 90: Numerical Simulation of Plasmas and Their Spectra. *Publications of the Astronomical Society of the Pacific*, 110(749):761–778, jul 1998.

[20] Y. Liu, X. W. Liu, S. G. Luo, and M. J. Barlow. Chemical abundances of planetary nebulae from optical recombination lines - I. Observations and plasma diagnostics. *Monthly Notices of the Royal Astronomical Society*, 353(4):1231–1250, 2004.

[21] Y. G. Tsamis, M. J. Barlow, X. W. Liu, P. J. Storey, and I. J. Danziger. A deep survey of heavy element lines in planetary nebulae - II. Recombination-line abundances and evidence for cold plasma. *Monthly Notices of the Royal Astronomical Society*, 353(3):953–979, 2004.

[22] MS Pindzola, SD Loch, and F Robicheaux. Dielectronic recombination in C 3 + above and below the ionization threshold. *Physical Review A*, 83:042705, 2011.

[23] K.G. Dyall, I.P. Grant, C.T. Johnson, F.A. Parpia, and E.P. Plummer. GRASP: A general-purpose relativistic atomic structure program. *Computer Physics Communications*, 55(3):425–456, oct 1989.

[24] Alessandra Giunta, Hugh Summers, Paul Bryans, and Martin O'mullane. ADAS-EU ADAS for fusion in Europe Grant: 224607 Generalised-collisional-modelling for light- and medium-weight elements. Technical report, 2012.

[25] M. F. Gu. Indirect XRay LineFormation Processes in Iron LShell Ions. *The Astrophysical Journal*, 582(2):1241–1250, jan 2003.

[26] M Fogle, NR Badnell, P Glans, SD Loch, S Madzunkov, S.A. Abdel-Naby, MS Pindzola, and R Schuch. Electron-ion recombination of Be-like C, N, and O. *A\&A*, 442:757–766, 2005.

[27] Taha Sochi and Peter J. Storey. Dielectronic recombination lines of C+. *Atomic Data and Nuclear Data Tables*, 99(6):633–650, 2013.

[28] A.˜R. Davey, P.˜J. Storey, and R Kisielius. Recombination coefficients for C Ii lines. *\Aaps*, 142:85–94, 2000.

[29] Thomas Peters, Steven N Longmore, and Cornelis P Dullemond. Understanding hydrogen recombination line observations with ALMA and EVLA. *Mon. Not. R. Astron. Soc*, 425:2352–2368, 2012.

[30] A. N. Starostin and I. I. Yakunin. The influence of plasma microfields on spectral properties of lithium-like ions in non-ideal plasma. In *The 14th international conference on spectral line shapes*, volume 467, pages 132–133. ASCE, apr 1999.

[31] MS Pindzola, SD Loch, and F Robicheaux. Dielectronic recombination in C 3 + above and below the ionization threshold. *Physical Review A*, 83:042705, 2011.

[32] S. Mannervik, D. DeWitt, L. Engström, J. Lidberg, E. Lindroth, R. Schuch, and W. Zong. Strong relativistic effects and natural linewidths observed in dielectronic recombination of lithiumlike carbon. *Physical Review Letters*, 81(2):313–316, 1998.

[33] Brian Sharpee, Yong Zhang, Robert Williams, Eric Pellegrini, Kenneth Cavagnolo, Jack A Baldwin, Mark Phillips, and Xiao-Wei Liu. s-Process Abundances in Planetary Nebulae. *The Astrophysical Journal*, 659 (2):1265–1290, 2006.

[34] J García-Rojas, S Madonna, V Luridiana, N C Sterling, C Morisset, G Delgado-Inglada, L Toribio, and San Cipriano. s-process enrichment in the planetary nebula NGC 3918. Results from deep echelle spectrophotometry. *MNRAS*, 452:2606–2640, 2015.

[35] C. G. Sherrard, Nicholas C. Sterling, H.L. Dinerstein, S. Madonna, and A. Mashburn. Abundance Analysis of 17 Planetary Nebulae from High-Resolution Optical Spectroscopy. In *230th AAS meeting*, page 318.11, Austin, 2017. AAS.

[36] Peter J. Storey and Taha Sochi. Electron temperatures and free-electron energy distributions of nebulae from C II dielectronic recombination lines. *Monthly Notices of the Royal Astronomical Society*, 430(1):599–610, 2013.

[37] M Eriksson, S Johansson, and G M Wahlgren. The nature of ultraviolet spectra of AG Pegasi and other symbiotic stars : locations , origins , and excitation mechanisms of emission lines. 175:157–175, 2006.

[38] Daniel Wolf Savin. Ionization Balance, Chemical Abundances, and the Metagalactic Radiation Field at High Redshift. *The Astrophysical Journal*, 533(1):106–112, 2000.

[39] J. García-Rojas, M. Peña, C. Morisset, G. Delgado-Inglada, A. Mesa-Delgado, and M.T. Ruiz. Analysis of chemical abundances in planetary nebulae with [wc] central stars: Ii. chemical abundances and the abundance discrepancy factor. *Astronomy and Astrophysics*, 558:1–25, 2013.

[40] Jorge Garcia Rojas and Cesar Esteban. On the Abundance Discrepancy Problem in H II Regions. *The Astrophysical Journal*, 670(1):457–470, 2007.

[41] R. Wesson, D. Jones, J. García-Rojas, H. M.J. Boffin, and R. L.M. Corradi. Confirmation of the link between central star binarity and extreme abundance discrepancy factors in planetary nebulae. *Monthly Notices of the Royal Astronomical Society*, 480(4):4589–4613, 2018.

[42] C Rola and G Stasi\'nska. The carbon abundance problem in planetary nebulae. *Aap*, 282:199–212, 1994.

[43] M Fogle, NR Badnell, P Glans, SD Loch, S Madzunkov, S.A. Abdel-Naby, MS Pindzola, and R Schuch. Electron-ion recombination of Be-like C, N, and O. *A&A*, 442:757–766, 2005.

[44] X. Fang, P. J. Storey, and X.-W. Liu. New effective recombination coefficients for nebular Niilines. *Astronomy & Astrophysics*, 530:A18, 2011.

[45] Manuel Peimbert. TEMPERATURE DETERMINATIONS OF H n REGIONS. *The Astrophysical Journal*, 150:825, 1967.

[46] S. M. Viegas and R. E. S. Clegg. Density condensations in planetary nebulae and the electron temperature. *Monthly Notices of the Royal Astronomical Society*, 271(4):993–998, dec 1994.

[47] XW Liu and PJ Storey. NGC 6153: a supermetalrich planetary nebula? *Monthly Notices of ...*, 312(3):585–628, 2000.

[48] David C. Nicholls, Michael A. Dopita, and Ralph S. Sutherland. RESOLVING THE ELECTRON TEMPERATURE DISCREPANCIES IN H II REGIONS AND PLANETARY NEBULAE: κ-DISTRIBUTED ELECTRONS. *The Astrophysical Journal*, 752(2):148, jun 2012.

[49] B. Ercolano, M. J. Barlow, P. J. Storey, X. W. Liu, T. Rauch, and K. Werner. Three-dimensional photoionization modelling of the hydrogen-deficient knots in the planetary nebula Abell 30. *Monthly Notices of the Royal Astronomical Society*, 344(4):1145–1154, 2003.

[50] B. T. Draine and C. D. Kreisch. Electron Energy Distributions in H ii Regions and Planetary Nebulae: κ -distributions Do Not Apply. *The Astrophysical Journal*, 862(1):30, jul 2018.

[51] D. R. Garnett and H. L. Dinerstein. Spatially-Resolved O II Recombination Line Observations of the Ring Nebula, NGC 6720. *The Astrophysical Journal*, 558:145–156, may 2001.

[52] Jorge García-Rojas, Romano L. M. Corradi, Hektor Monteiro, David Jones, Pablo Rodríguez-Gil, and Antonio Cabrera-Lavers. Imaging the elusive H-poor gas in the high ADF planetary nebula NGC 6778. *The Astrophysical Journal Letters, Volume 824, Issue 2, article id. L27, 5 pp. (2016).*, 824, jun 2016.

[53] A. Peimbert, M. Peimbert, G. Delgado-Inglada, J. García-Rojas, and M. Peña. Physical conditions derived from O II recombination lines in planetary nebulae and their implications. *Revista Mexicana de Astronomia y Astrofisica*, 50(2):329–340, 2014.

[54] T. Barker and T. The ionization structure of planetary nebulae. III - NGC 7009. *The Astrophysical Journal*, 267:630, apr 1983.

[55] J. P. Harrington and W. A. Feibelman. The remarkable ultraviolet spectrum of the planetary nebula Abell 30. *The Astrophysical Journal*, 277:716, feb 1984.

[56] A. PEDLAR. Anomalous Recombination Line 166α. *Nature*, 226(5248):830–831, may 1970.

[57] Leo Goldberg. Stimulated Emission of Radio-Frequency Lines of Hydrogen. *The Astrophysical Journal*, 144:1225, jun 1966.

[58] A.K. (Harvard College Observatory) Dupree and L. (Harvard College Observatory) Goldberg. Radiofrequency recombination lines. *Annual Review of Astronomy and Astrophsyics*, 8:231, 1970.

[59] M. A. (Mark A.) Gordon and R. L. Sorochenko. *Radio recombination lines : their physics and astronomical applications*. Springer, 2009.

[60] P. A. Shaver, E. Churchwell, and A. H. Rots. Stimulated Recombination Line Emission from M 82. *Astronomy and Astrophysics*, 55:435, mar 1977.

[61] K. R. Anantharamaiah, Jun-Hui Zhao, W. M. Goss, and F. Viallefond. Detection of H92 alpha Recombination Line from the Galaxies NGC 3628, IC 694, and NGC 1365. *The Astrophysical Journal*, 419:585, dec 1993.

[62] P.A. Shaver. Why is observable Radio Recombination Line emission from galactic H II regions always close to LTE? *Astronomy and Astrophysics*, 90:34–43, 1980.